

**IN-SITU RADIATION GRAFTING OF POLYMER FILMS
AND DEGRADATION STUDIES OF MONOMERS FOR
APPLICATIONS IN FUEL CELL MEMBRANES**

Von der Fakultät Chemie der Universität Stuttgart zur
Erlangung der Würde eines Doktors der Naturwissenschaften
(Dr. rer. nat.) genehmigte Abhandlung

vorgelegt von

M. Sc. Svetlin Mitov
aus Burgas, Bulgarien

Hauptberichter: Prof. Dr. Emil Roduner
Mitberichter: Prof. Dr. Andreas Friedrich

Tag der mündlichen Prüfung: 01.02.2007

INSTITUT FÜR PHYSIKALISCHE CHEMIE
DER UNIVERSITÄT STUTTGART

February 2007

Eidesstattliche Erklärung

Ich versichere, dass ich diese Dissertation selbstständig verfasst und nur die angegebenen Quellen und Hilfsmittel verwendet habe.

Stuttgart, 04.12.2006

Svetlin Mitov

Prüfungsvorsitzender: Prof. Dr. Friedhelm Zabel

Hauptberichter: Prof. Dr. Emil Roduner

Mitberichter: Prof. Dr. Andreas Friedrich

Tag der mündlichen Prüfung: 01.02.2007

CONTENTS

CONTENTS.....	3
ABBREVIATIONS.....	6
LIST OF FIGURES.....	8
LIST OF TABLES.....	12
1 INTRODUCTION AND MOTIVATION.....	14
2 BACKGROUND INFORMATION.....	18
2.1 Membranes.....	18
2.2 Direct photolysis.....	23
2.3 HO [•] radical initiated degradation.....	25
2.4 Radiation grafting.....	32
2.5 Non-fluorinated and perfluorinated alkyl and alkyl-peroxy radicals.....	35
3 EXPERIMENTAL AND THEORETICAL METHODS.....	37
3.1 Electron Spin Resonance.....	37
3.1.1 The <i>g</i> -value.....	38
3.1.2 Hyperfine structure.....	39
3.1.3 Hyperfine coupling constants.....	40
3.1.3.1 Electron and spin density, spin population and spin polarization.....	40
3.1.3.2 McConnell relations for α and β -nuclei.....	41
3.1.3.3 γ and δ -nuclei.....	42
3.1.4 Spin trapping technique.....	42
3.2 UV-VIS spectroscopy and Beer-Lambert law.....	43
3.3 Density Functional Theory and Gaussian calculations.....	44
3.4 Non-fluorinated monomeric building blocks.....	47
3.4.1 Preparation of solutions.....	47
3.4.2 Apparatus and analysis of ESR spectra.....	49
3.5 E-beam irradiated fluoropolymer films.....	49
3.5.1 Preparation of irradiated fluoropolymer samples.....	49
3.5.2 In-situ ESR measurements during grafting reactions.....	50
3.5.3 Analysis of decay curves and grafting levels.....	51
3.6 DFT calculations for non-fluorinated and perfluorinated fragments.....	52

4	OXIDATIVE AND PHOTOCHEMICAL STABILITY OF NON-FLUORINATED IONOMERS.....	55
4.1	ESR results and specific discussion.....	55
4.1.1	4,4'-Sulfonyldiphenol (SDP).....	55
4.1.2	Bisphenol A (BPA).....	57
4.1.3	4,4'-Diphenol (DP).....	62
4.1.4	Sulfonated 4,4'-Dichlorodiphenylsulfone (sDCPS).....	65
4.1.5	4,4'-Dihydroxybenzophenone (HBP).....	66
4.1.6	Sulfonated Polyetherketones (sPEK, sPEEK and sPEKEK).....	66
4.2	Discussion.....	67
4.2.1	Aspects of direct photolysis.....	67
4.2.2	Formation of phenoxy and semi-quinone radicals and the origin of its pH dependence.....	68
4.3	Relevance for fuel cell membranes.....	70
5	IN-SITU STUDY OF STYRENE GRAFTING OF ELECTRON IRRADIATED FLUOROPOLYMER FILMS.....	73
5.1	Results.....	73
5.1.1	Spin concentrations for FEP, ETFE and PVDF.....	73
5.1.2	Interpretation of ESR spectra obtained with FEP and ETFE.....	75
5.1.2.1	ESR spectra of irradiated FEP.....	75
5.1.2.2	ESR spectra of irradiated ETFE.....	79
5.1.2.3	ESR spectra of irradiated PVDF.....	83
5.1.3	Grafting of ETFE.....	85
5.1.4	Grafting of FEP.....	89
5.1.5	Grafting of PVDF.....	91
5.2	Discussion.....	92
5.2.1	Styrene attachment products.....	92
5.2.2	The influence of crystallinity.....	92
5.2.3	Grafting rates and influence of solvents.....	93
5.2.4	Grafting levels.....	94
6	COMPARATIVE DFT STUDY OF NON-FLUORINATED AND PERFLUORINATED FRAGMENTS.....	97
6.1	Bond dissociation energies and reaction enthalpies.....	97
6.2	Optimized geometries and charge distributions.....	101

6.3	Energy barriers to internal rotation.....	106
6.4	<i>g</i> -Tensors.....	107
6.5	Hyperfine couplings.....	108
6.6	Further discussions.....	114
7	SUMMARY.....	120
	ZUSAMMENFASSUNG.....	127
	ACKNOWLEDGEMENT.....	134
	BIBLIOGRAPHY.....	136

ABBREVIATIONS

AO	Atomic Orbital
BPA	Bisphenol A
BDEs	Bond Dissociation Energies
BPSH	Biphenol-based poly(arylene ether sulfone)
DBNBS	3,5-Dibromo-4-nitrosobenzene-sulfonic acid
DBS	Dangling Bond Site
DFT	Density Functional Theory
DMFC	Direct Methanol Fuel Cell
DMPO	5,5-Dimethyl-1-pyrroline- <i>N</i> -oxide
DP	4,4'-Diphenol
ESR	Electron Spin Resonance
ETFE	Poly(ethylene-alt-tetrafluoroethylene)
FC	Fluorocarbon
FEP	Poly(tetrafluoroethylene-co-hexafluoropropylene)
FEP-g-PSA	Poly(tetrafluoroethylene-co-hexafluoropropylene) grafted with Polystyrene Sulfonic Acid
HBP	4,4'-Dihydroxybenzophenone
HC	Hydrocarbon
HF	Hartree Fock
HFCs	Hyperfine Coupling Constants
KS	Kohn and Sham
LDA	Local Density Approximation
LYP	Lee, Yang and Parr
MEA	Membrane Electrode Assembly
MMA	Methyl Methacrylate
MO	Molecular Orbital
NMR	Nuclear Magnetic Resonance
PBI	Polybenzimidazole
PE	Polyethylene
PEK	Polyetherketone
PEEK	Poly(ether ether ketone)
PEKEK	Poly(ether ketone ether ketone)

ABBREVIATIONS

PEMFC	Polymer Electrolyte Membrane Fuel Cell
PES	Polyethersulfone
PFA	Perfluoro(alkylvinyl ether)
PFSA	Perfluorosulfonic acid
POBN	α -(4-pyridyl-1-oxide)- <i>N</i> - <i>tert</i> -butylnitrone
PPBP	Poly(phenoxy benzoyl phenylene)
PSU	Polysulfone
PTFE	Poly(tetrafluoroethylene)
PVDF	Poly(vinylidene fluoride)
sDCPS	4,4'-Dichlorodiphenylsulfone
SDP	4,4'-Sulfonyldiphenol

LIST OF FIGURES

Fig. 1: Primary photodissociative processes in aromatic hydrocarbons [42].....	24
Fig. 2: Formation of benzyl radicals by acid catalysis from hydroxycyclohexadienyl radicals [47,57].....	26
Fig. 3: Mechanisms for consecutive reactions of hydroxycyclohexadienyl radicals with oxygen leading to different phenolic compounds and to bond breaking [47,57].....	27
Fig. 4: Possible sites for HO• radical attack on various polymers used in proton-conducting membranes [57].....	28
Fig. 5: ESR hyperfine splittings and <i>g</i> -values for radical intermediates of the reaction of HO• radicals with aromatic hydrocarbons [68].....	30
Fig. 6: Membrane preparation by pre-irradiation grafting [74].....	32
Fig. 7: Simplified qualitative view of grafting front mechanism [87].....	34
Fig. 8: Reaction mechanism with DBNBS spin trap agent.....	42
Fig. 9: Model compounds for the investigation of HO• initiated degradation reactions.....	48
Fig. 10: Quartz cell for <i>in-situ</i> ESR experiments during grafting of irradiated polymer films [122].....	51
Fig. 11: Experimental ESR spectrum of the <i>p</i> -benzosemiquinone radical anion 1 obtained with SDP at pH 12.2 and 135 ml h ⁻¹ flow rate.....	55
Fig. 12: Relative intensities of the ESR signals of radical 1 observed with SDP at 135 ml h ⁻¹ flow rate in dependence on the pH-value.....	56
Fig. 13: ESR spectrum of an SDP/DBNBS/water/methanol/H ₂ O ₂ mixture at pH 0.4 and at a) flow rate of 8 ml h ⁻¹ ; b) flow rate of 90 ml h ⁻¹	57
Fig. 14: a) Experimental ESR spectrum obtained with BPA at pH=12 and 135 ml h ⁻¹ flow rate; b) simulation for the sum of radicals 1-4 ; c) simulation of radical 1 (33%); d) simulation of radical 2 (5%); e) simulation of radical 3 (14%); f) simulation of radical 4 (48%).....	58
Fig. 15: ESR spectra obtained with BPA at pH 12 and different flow rates: a) 90 ml h ⁻¹ ; b) 20 ml h ⁻¹ ; c) 8 ml h ⁻¹	61
Fig. 16: Relative intensities of the ESR signals of the radicals 1 (♦), 2 (●), 3 (▲) and 4 (▼) observed with BPA at 90 ml h ⁻¹ flow rate in dependence on the pH-value.....	62

Fig. 17: ESR spectra obtained with DP acquired at 135 ml h ⁻¹ flow rate and: a) pH=12.2, no H ₂ O ₂ ; b) pH 10.3; c) pH 11.3; d) pH 12.2; e) pH 13.0. Spectra (b-e) are measured in the presence of H ₂ O ₂	63
Fig. 18: a) Experimental spectrum obtained with DP at pH=10.3 and 135 ml h ⁻¹ flow rate; b) simulation for the sum of radicals 6-10 ; c) simulation radical 6 ; d) simulation radical 7 ; e) simulation radical 8 ; f) simulation radical 9 ; g) simulation radical 10	64
Fig. 19: Experimental ESR spectrum obtained with sDCPS at pH 12.2 and a) flow rate 13 ml h ⁻¹ ; b) flow rate 20 ml h ⁻¹ ; c) simulation of radical 11 . The asterisk denotes the SO ₃ ^{•-} radical.....	65
Fig. 20: Experimental ESR spectra obtained with sPEKs at pH=12.1 and 90 ml h ⁻¹ flow rate.....	67
Fig. 21: Suggested formation mechanism of radical 2 (R = C(CH ₃) ₂ C ₆ H ₄ OH) [130].....	69
Fig. 22: Possible formation mechanism of radical 6 and further dioxysubstituted species (R= C ₆ H ₄ OH) [66,131,132].....	70
Fig. 23: <i>Teflon</i> -PVDF: a) peroxy radical at -120 °C, superimposed partly by alkyl radicals; b) alkyl radical at -120 °C.....	75
Fig. 24: Potential radical species formed in irradiated FEP.....	76
Fig. 25: a) Experimental spectrum obtained with FEP after electron irradiation under Ar; b) sum of all simulated radicals; c) simulation radical E; d) simulation radical F; e) simulation radical A.....	78
Fig. 26: Temperature dependence of ESR spectra obtained with FEP after electron irradiation under air.....	79
Fig. 27: Temperature dependence of the <i>g</i> -tensor of the peroxoradical obtained with FEP after electron irradiation under air.....	79
Fig. 28: Potential radical species formed in irradiated ETFE.....	80
Fig. 29: a) Experimental ESR spectrum obtained with ETFE after electron irradiation under Ar; b) sum of all simulated radicals; c) simulation radical F; d) simulation radical E; (* irradiated quartz).....	81
Fig. 30: Temperature dependence of ESR spectra obtained with ETFE after electron irradiation under Ar (* irradiated quartz).....	81
Fig. 31: Temperature dependence of ESR spectra obtained with ETFE after electron irradiation under air: a) -120 °C; b) 0 °C; c) +80 °C (* irradiated quartz).....	82
Fig. 32: Temperature dependence of the <i>g</i> -tensor of the peroxoradical obtained with ETFE after electron irradiation under air.....	83
Fig. 33: Potential radical species formed in irradiated PVDF.....	84

- Fig. 34:** ESR spectra during the grafting process of styrene on *Teflon*-ETFE (40 kGy) at +60 °C: a) after 2 min; b) after 150 min (* irradiated quartz).....85
- Fig. 35:** ESR spectra during the grafting process of styrene onto peroxy radicals in *Teflon*-ETFE (40 kGy) at +60 °C: a) after 2 min; b) after 160 min (* irradiated quartz, arrows: alkyl radicals).....86
- Fig. 36:** ESR spectra during the grafting process of 25% styrene in benzene onto peroxy radicals in *Teflon*-ETFE (40 kGy) at +60 °C: a) after 2 min; b) after 180 min (* irradiated quartz).....87
- Fig. 37:** Normalized intensities of the ESR spectra of ETFE radicals during the grafting process at +60 °C relative to their initial concentration: alkyl radicals, 25% styrene in benzene (■); peroxy radicals, 25% styrene in ethanol (+); alkyl radicals, styrene (●); peroxy radicals, styrene (▲); peroxy radicals, 25% styrene in benzene (*)......87
- Fig. 38:** ESR spectra during the grafting process of styrene on *Teflon*-FEP (40 kGy) at +60 °C: a) after 2 min; b) after 40 min (* irradiated quartz).....89
- Fig. 39:** ESR spectra during the grafting process of styrene onto peroxy radicals in *Teflon*-FEP (40 kGy) at +60 °C: a) after 2 min; b) after 60 min (* irradiated quartz, dotted arrows: alkyl radicals).....90
- Fig. 40:** Normalized intensities of the ESR spectra of FEP radicals during the grafting process at +60 °C relative to their initial concentration: alkyl radicals, styrene (■); peroxy radicals, 25% styrene in ethanol (+); alkyl radicals, 25% styrene in benzene (●); peroxy radicals, styrene (*); peroxy radicals, 25% styrene in benzene (▼).....91
- Fig. 41:** Optimized geometries of non-fluorinated and perfluorinated primary alkyl and alkyl-peroxy radicals (selected bond lengths in Å (bold), total atomic charges in a.u. (italics)).....103
- Fig. 42:** Optimized geometries of non-fluorinated and perfluorinated secondary alkyl and alkyl-peroxy radicals (selected bond lengths in Å (bold), total atomic charges in a.u. (italics)).....104
- Fig. 43:** Optimized geometries of non-fluorinated and perfluorinated tertiary alkyl and alkyl-peroxy radicals (selected bond lengths in Å (bold), total atomic charges in a.u. (italics)).....105
- Fig. 44:** Possible conformations of the fluorinated ethyl radical.....106
- Fig. 45:** Relative energies as a function of the dihedral angle θ for optimized (left) and planar (right) $\text{CF}_3\bullet\text{CF}_2$ structures.....107
- Fig. 46:** g -Tensor components and isotropic g -value (▲) as a function of the dihedral angle θ for optimized $\text{CF}_3\bullet\text{CF}_2$108
- Fig. 47:** F^α hfc as a function of the dihedral angle θ for optimized (left) and planar (right) $\text{CF}_3\bullet\text{CF}_2$ structures.....110

Fig. 48: Anisotropic spin-dipole couplings and directions of the dipolar contribution to the ^{19}F hyperfine tensor for optimized $\text{CF}_3\cdot\text{CF}_2$ structure in eclipsed (left) and anti-periplanar (right) conformations.....	111
Fig. 49: F^β hfc as a function of the dihedral angle θ for optimized (left) and planar (right) $\text{CF}_3\cdot\text{CF}_2$ structures.....	112
Fig. 50: Spin density distribution for the fluorinated ethyl radical.....	117

LIST OF TABLES

Table 1: Commercial PFSA Membranes by Producer [5].....	19
Table 2: Rate constants for reactions of HO• radicals [67].....	29
Table 3: Rate constants for reactions of HO• and O•- radicals with different substrates [67].....	31
Table 4: ESR parameters of intermediates in the reaction of HO• radicals with sulfonated aromatics.....	59
Table 5: Spin concentrations at 40 kGy electron radiation dose for FEP, ETFE and PVDF polymer films.....	74
Table 6: Solvent effect on the grafting reactions of <i>Teflon</i> -ETFE and <i>Teflon</i> -FEP at +60 °C.....	88
Table 7: Grafting levels (eqn. 3-30) for grafting at +60 °C and average number of monomer units per chain at 40 kGy radiation dose in dependence on solvent.....	95
Table 8: Bond dissociation energies for primary, secondary, and tertiary peroxy radicals (kJ mol ⁻¹).....	98
Table 9: Bond dissociation energies for primary, secondary, and tertiary peroxide molecules (kJ mol ⁻¹).....	98
Table 10: Reaction enthalpies $\Delta_R H$ of reactions (6-1) and (6-2) (kJ mol ⁻¹).....	99
Table 11: Bond dissociation energies for primary, secondary, and tertiary alcohol OH and OF bonds (kJ mol ⁻¹).....	100
Table 12: Reaction enthalpies $\Delta_R H$ of reaction (6-3) (kJ mol ⁻¹).....	100
Table 13: Isotropic hfc of ¹³ C ^α and ¹³ C ^β nuclei represented by the coefficients of eqn. (6-4) for the non-fluorinated and fluorinated ethyl radicals.....	109
Table 14: Isotropic hfc of H ^α and F ^α nuclei represented by the coefficients of eqn. (6-4) for the non-fluorinated and fluorinated ethyl radicals.....	110
Table 15: Isotropic hfc of H ^β and F ^β nuclei represented by the coefficients of eqn. (3-31) for the non-fluorinated and fluorinated ethyl and 1-propyl radicals (rotation is about the C ^α -C ^β bond).....	113
Table 16: Isotropic hfc of ¹³ C ^γ nucleus represented by the coefficients of eqn. (3-31) for the non-fluorinated and fluorinated 1-propyl radicals (rotation is about the C ^α -C ^β bond).....	113

Table 17: Isotropic hfc of F^γ (H^γ) nuclei represented by the coefficients of eqn. (3-31) for the non-fluorinated and fluorinated 1-propyl radicals114

Chapter 1

1 INTRODUCTION AND MOTIVATION

The World is entirely dependent on oil. The transportation sector in particular, so vital in our society for carrying people, goods, food and materials, relies on more than 95% of its gasoline, diesel and kerosene derived from petroleum, and consumes about 60% of the oil produced [1]. We also depend on oil for the large variety of petrochemicals and derived products such as plastics, detergents and synthetic fabrics. Oil is so important because it is the most versatile among the three primary fossil fuels. It has a high energy content, is easy to transport, and is relatively compact. Coal is heavier, more bulky and more polluting. Natural gas on the other hand is cleaner burning but bulky in volume and requires pipelines or expensive liquefaction for transportation, which raises safety concerns.

There are two key problems with continued use of fossil fuels which meet about 80% of the world energy demand today. The first problem is that they are limited in amount and sooner or later will be depleted. According to the estimates by petroleum companies, the production of the most convenient utilizable fossil fuels, petroleum and natural gas, will peak sometime between the years 2015 and 2020 and then begin to decrease. This means that there will be a gap between demand and production of fluid fuels, beginning around 2015 [2]. The second problem is that fossil fuels are causing serious environmental problems, such as global warming, climate changes, melting of ice caps, acid rains, pollution, ozone layer depletion, forest and agricultural land damage, etc [2]. Today new approaches are needed for the solution of these two interconnected global problems, thus mitigating any human-caused global climate change and liberating mankind from its dependence on diminishing fossil fuel reserves.

Fuel cells are devices that convert the chemical energy of a fuel directly into electrical energy by electrochemical reactions. In contrast to heat engines (gasoline and diesel engines) the fuel cell does not involve conversion of heat to mechanical energy and the overall thermodynamic efficiencies can be very high. They are considered to be one of the main solutions for the efficient utilization of fossil fuel-derived fuels. The possible applications of fuel cells are numerous, from micro fuel cells producing only a few watts needed in cell phones and laptops, to on-board fuel cells for the automobile sector, and large units able to produce several MW to provide buildings with electricity. Major drawbacks to the widespread

commercialization of fuel cells are mainly technological (reliability issues, material durability, catalyst utilization, mass transport, etc.) and cost-related.

Hydrogen-based fuel cells produce electricity, heat and water by catalytically combining hydrogen and oxygen. Hydrogen, the simplest element consisting of one proton and one electron, makes up 90% of the composition of the universe and is the third most abundant element on the earth's surface. Hydrogen is not a primary energy source, but it is an excellent energy carrier with many unique properties. It is the lightest, most efficient and cleanest fuel. Such a wealth of fuel would provide an almost unlimited source of energy at relatively low cost. But there is a price to pay: the fuel cell stack that converts oxygen and hydrogen to electricity is expensive to build and maintain.

Producing hydrogen is only the first step in the envisioned hydrogen economy, the next is the storage of the generated hydrogen in a form that should be economical, practical, safe and user-friendly. Current technology involves the physical or chemical storage of hydrogen. Physical storage is effected in insulated or high-pressure containers in which hydrogen is stored as a liquefied or compressed gas. Chemical storage includes metals and other materials which absorb hydrogen. If propane, natural gas or diesel is used, a reformer is needed to generate hydrogen. Reformers for Polymer Electrolyte Membrane Fuel Cells (PEMFCs) are bulky and expensive. They start up slowly, and further purification of the hydrogen is required. As a result some fuel efficiency is lost and certain emissions are generated, including CO₂. In general, these emissions are much lower than those of comparable conventional energy conversion technologies.

For transportation, the PEMFCs are at present the most promising option to replace the current internal combustion engine. They operate like a refuelable battery, generating electricity for as long as they are supplied with hydrogen fuel and oxygen (from air). Today, numerous PEM fuel cell-powered prototype vehicles are being tested worldwide by the major automobile companies, including Daimler-Chrysler, Volkswagen, Toyota, Renault, Ford and General Motors. To make fuel cell-powered vehicles affordable, however, major technological breakthroughs are needed in order to make a significant lowering of production costs and also to mitigate safety issues. Most crucial is the lifetime of a fuel cell, for which more than 40,000 hours of continuous and stable performance are required. Poisoning of the platinum-based anode catalysts by trace amounts of CO inevitably contained in reformed fuels results in a severe deterioration of performance [3]. Water management in the membrane is critical as well for an efficient operation.

In this work we try to acquire new insights in problems of a long term stability for low temperature fuel cells. We concentrate on the studies of membrane stability because the membrane is a key component of a fuel cell often limiting the performance of a whole fuel cell system. Oxidative degradation of polymers is usually a free radical process which involves attack of the hydroxyl and hydroperoxyl radicals, HO^\bullet and HOO^\bullet . Both radicals are intermediates of the oxygen reduction in a fuel cell process, and since hydrogen peroxide has been detected as a trace by-product of the fuel cell reaction it is plausibly assumed that attack of these two radicals is an important degradation pathway of the proton conducting polymer membrane. Electron Spin Resonance (ESR) methods are particularly sensitive and suitable for their investigation. ESR is, as well, a suitable spectroscopic technique to identify the nature of radiation generated radicals in organic polymers, and to monitor their concentration in-situ during grafting reactions. The focus of the first part of the present work are the reaction mechanisms which are accessible *via* the structures of free radical intermediates, and the identification of fuel cell operating conditions which may lead to enhanced free radical production. These points are addressed by exposing novel membrane building blocks in solutions to the above intentionally produced oxidative radicals. Non-fluorinated aromatic monomers are chosen, since much effort has focused on the development of alternative PEMFCs in particular with the aim of increasing the temperature of operation of the fuel cell, namely above 80 °C.

Since radiation-induced grafting of commercially available polymer films followed by sulfonation is one of the promising synthesis strategies in the development of new materials for PEMFCs, in the second part of the present work we investigate different electron beam irradiated fluoropolymers, as well as their grafting reactions with styrene in different diluents, by means of ESR. Thus, we compare the decay of radicals in different fluoropolymers by carrying out *in-situ* ESR measurements in a similar systematic manner during the radiation grafting process, aiming at an understanding of the influence of the irradiation atmosphere and of the diluent. In the development of new membranes, the introduction of a functional property into a preformed commodity polymer film by grafting of a second component onto activated centers in the base polymer through radical polymerization is a versatile technique [4]. In particular for fuel cell application, low-cost raw materials for the base polymer and graft monomer can be selected, yielding a cost-competitive material for proton exchange membranes.

Furthermore, in the radiation grafting of polymer films with styrene for fuel cell applications it is important to control whether the polystyrene chain is grafted onto a peroxy

or a carbon centered radical. Therefore thermodynamic properties of small alkyl and alkylperoxy radicals are studied to model primary, secondary and tertiary radicals in non-fluorinated and perfluorinated polymers. Bond strengths, bond lengths, and total atomic charges are compared for the above mentioned radicals. The effects of non-planarity of the $\text{RCF}_2\cdot\text{CF}_2$ and $\text{RCH}_2\cdot\text{CH}_2$ radical centers on the barrier to internal rotation and on the β -hyperfine coupling constants and g -tensor components as a function of dihedral angle, are studied as well. An understanding of the hyperfine couplings is essential for the correct assignment of radical structures and conformations in solid environments.

Chapter 2

2 BACKGROUND INFORMATION

In this chapter the focus is put on the proton-conducting membrane as a key component of low and medium temperature fuel cells.

2.1 Membranes

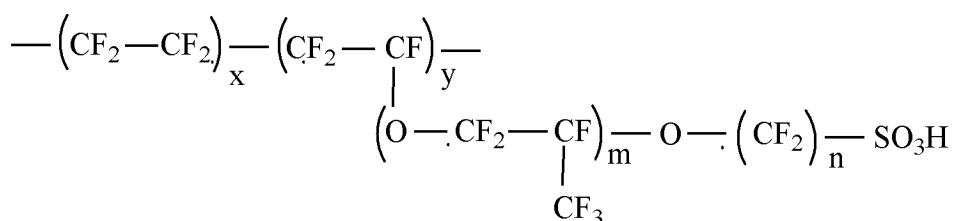
PEMFCs use a proton exchange membrane as an electrolyte. They are low temperature fuel cells, generally operating between 85 and 105 °C. The membrane consists of a fluorocarbon or F-free aromatic polymer backbone, to which sulfonic acid groups are attached. On both sides of the membrane there is a porous electrode. The electrodes must be porous because the reactant gases are fed from the back and must reach the interface between the electrodes and the membrane, where the electrochemical reaction takes place in the so-called catalyst layers. The multilayer assembly of the membrane sandwiched between the two electrodes is commonly called the Membrane Electrode Assembly (MEA). The MEA is then sandwiched between the collector/separator plates: collector because they collect and conduct electrical current, and separator because in multicell configuration they separate the gases in the adjacent cells. They provide the pathways for flow of reactant gases, and they also provide the cell structural rigidity [2]. Thus the function of the membrane is twofold: proton conduction from the anode to the cathode, and effective separation of the anode and cathode gases.

Enormous efforts are devoted to the development of new materials for proton conducting fuel cell membranes. The general focus is on obtaining lower cost per unit of generated power over the cell lifetime. More specifically, this means that thin membranes are sought based on low cost starting materials and simple synthetic procedures. They are required to be gas tight, have high proton exchange capacity and are of sufficient thermal, mechanical, and chemical stability [5]. Fluoropolymers are characterized by their excellence in resisting chemical attack, their very good thermal stability, chemical inertness, outstanding electrical properties and excellent weathering. These properties differentiate fluoropolymers from their hydrocarbon analogues, and make them preferable materials for high energy radiation environments in the chemical, microelectronic, and nuclear industries, as well as in medicine and aerospace [6].

Furthermore preformed fluoropolymer films can be transformed into proton exchange membranes. The films are irradiated and grafted with styrene and the polystyrene grafts are subsequently sulfonated (see subchapter 2.4 for further details). The aim is to produce membranes that combine the mechanical strength and chemical resistance of the original film with the proton-conducting properties provided by the sulfonic acid groups. Such membranes find applications as polymer electrolytes for fuel cells and the results are promising.

The currently well-developed PEMFC technology is based on perfluorosulfonic acid (PFSA) polymer membranes as electrolyte [7,8]. PFSA membranes are composed of carbon-fluorine backbone chains with perfluoro side chains containing sulfonic acid groups. Some typical commercial PFSA membranes and their structures are listed in Table 1:

Table 1: Commercial PFSA Membranes by Producer [5].



Structure parameter	Trade name and type	Equivalent weight	Thickness, μm
DuPont			
m=1; x=5-13.5; n=2; y=1	Nafion 120	1200	260
	Nafion 117	1100	175
	Nafion 115	1100	125
	Nafion 112	1100	80
Asashi Glass			
m=0, 1; n=1-5	Flemion-T	1000	120
	Flemion-S	1000	80
	Flemion-R	1000	50
Asashi Chemicals			
m=0; n=2-5; x=1.5-14	Aciplex-S	1000-1200	25-100
Dow Chemical			
m=0; n=2; x=3.6-10	Dow	800	125

The DuPont product Nafion[®] is the standard membrane material for low temperature fuel cells [9]. Because of its poly(tetrafluoroethylene) (PTFE) backbone, it is chemically inert in both oxidizing and reducing atmospheres. Although the Teflon-like backbone is highly hydrophobic, the sulfonic acid at the end of the side chain is highly hydrophilic. The hydrophilic regions are created around the clusters of sulfonated side chains. This is why this kind of material absorbs relatively large amounts of water (in some cases up to 50% by weight). H⁺ ions movement within well-hydrated regions makes these materials proton conductive. Nafion[®] membranes are highly acidic, have excellent proton conductivity ($9 \times 10^{-3} - 12 \times 10^{-2} \text{ S cm}^{-1}$ at 80 °C in the range 34-100% relative humidity) [10], and unsurpassed longevity (> 60 000 h) in a fuel cell environment [5]. The main shortcomings of these materials is their high price of US\$ 500-800 m⁻² where the thickness of the membrane is an important cost factor and the production process which includes strongly toxic and environment-unfriendly intermediates [11,12]. However expiring patents may reduce this cost in a not too far future [12]. At T > 100 °C the membranes show a significant amount of drying-out, leading to a conductivity drop of several orders of magnitude [13]. A shortcoming of the perfluorinated ionomers especially related to their application in Direct Methanol Fuel Cells (DMFCs) is their high methanol permeability leading to poisoning of the cathode catalyst and therefore to large reduction in power density [14,15]. These features are common to the other perfluorinated membranes, such as those produced by Dow, Asahi Glass and Asahi Chemical (Table 1).

However, even the extremely stable Nafion[®] can suffer from degradation [16]. At an operating temperature of 50 °C, evidence for the deterioration of Nafion[®] membranes was detected by X-ray power diffraction and X-ray photoelectron spectroscopy; moreover, it was reported that the type of structural damage is different at the anode and cathode sides [17]. Product water analysis showed the presence of fluoride ions, low molecular weight perfluorocarbon sulfonic acid and CO₂ [18]. Fluoride ion release *via* detection in the product water after long-term operation indicates that the polymer may undergo certain chemical decomposition [19,20]. A life prediction of 10000 h for a fluoride release rate of $5.38 \times 10^{-5} \text{ mg (F) cm}^{-2} \text{ h}^{-1}$ for a Nafion[®] membrane with thickness of 200-250 μm working at 0.5 A cm⁻² was reported [19]. The susceptibility towards oxidative degradation of Nafion[®] has been attributed to traces of -CHF₂- groups that are hard to avoid during synthesis, or to -CF=CF₂ groups formed in the termination step of polymerization. Furthermore, the tertiary fluorine atom, which is further activated by the inductive effect of the ether link of the -OCF₂CF₂SO₃H side chain, is a potential site of F-abstraction by HO[•] radicals. A radical

defect on the chain can, in a domino-type process, lead to continuous disintegration by bond cleavage and/or oxidation [21].

Partially fluorinated ionomers are also under active research and examples include an ionomer membrane type prepared by styrene/divinylbenzene grafting of γ -irradiated (poly(tetrafluoroethylene-co-hexafluoropropylene)) (FEP) and consequent sulfonation by immersion of the foils in chlorosulfonic acid/dichloroethane mixtures [22,23]. Partially fluorinated membranes based on α,β,β -trifluorostyrene (TFS) and substituted TFS copolymer composition were also investigated and the MEAs incorporating these composite membranes were tested for 200-1400 h at 70 °C [24]. Ballard Power Systems (Canada) used substituted TFS monomers in their BAM grafted polymer electrolyte membrane, such as *para*-methyl-, -methoxy-, or -phenoxy-TFS, and these were activated toward grafting [25,26]. The main advantage of using TFS is that it does not contain benzylic hydrogen atoms, which makes it chemically much more stable [27]. At the same time the production process for the TFS-monomer is complicated, and the sulfonation of poly-TFS-homo-and-copolymers is found to be difficult [28].

In the past years there is a tremendous acceleration in research devoted to non-fluorinated polymer membranes, both as competitive alternatives to commercial perfluorosulfonic acid membranes operating in the same temperature range and with the objective of extending the range of operation of polymer fuel cells toward those more generally occupied by phosphoric acid fuel cells [29]. Consequently, much effort has focused on the development of alternative proton exchange membranes for PEFCs and DMFCs, in particular with the aim of increasing the temperature of operation of the fuel cell. Important advantages in terms of water management, increased proton conductivity and CO tolerance in fuel cells can be gained by operating at higher temperature, typically ≈ 120 °C; this operating temperature imposes additional stringent requirements in terms of membrane stability in a highly oxidative environment. There are few non-fluorinated membrane materials appropriate for fuel cell applications at temperatures above 80 °C, and they are made up of polyaromatic or polyheterocyclic repeat units. Examples include polysulfones (PSU), polyethersulfone (PES), polyetherketone (PEK), poly(ether ether ketone (PEEK), poly(ether ketone ether ketone) (PEKEK), poly(phenoxy benzoyl phenylene) (PPBP), polybenzimidazole (PBI), polyphenylquinoxaline, polyetherimides, etc. Membranes based on sulfonated PEEK (sPEEK) are promising for fuel cell applications as they possess good thermal stability and mechanical properties, and the proton conductivity can be controlled by the degree of sulfonation [30,31]. The sPEEK membranes with a degree of sulfonation of around 50%

exhibit performances comparable to or exceeding that of Nafion[®] due to lower methanol crossover, but the operating temperature must be limited to $< 65\text{ }^{\circ}\text{C}$ [30]. Usually high sulfonation levels (therefore greater water uptake) are needed with these polyaromatic membranes to obtain comparable proton conductivities as to Nafion[®], because the acidity of the pendant perfluorosulfonic acid in the polymer electrolyte is much stronger than those typically encountered in hydrocarbon membranes, such as the aryl sulfonic acid [32]. An interesting comparison study between sPEEK and sPPBP has been performed, as both polymers are isomers. The water uptake at low relative humidity as well as the conductivity at high temperatures is higher for sPPBP [33]. Membranes with high degrees of sulfonation experience huge swelling at higher temperatures ($80\text{ }^{\circ}\text{C}$) and undergo failure. Such problems related to excessive swelling can be solved by enhancing the membrane strength through crosslinking or making composites with certain inorganic reinforcement [34]. Both reinforcement and inorganic doping of covalently cross-linked blend membranes based onto sulfonated poly(arylene ether ketone)s and sulfonated PESs reduced the water uptake, particularly at temperatures $> 60\text{ }^{\circ}\text{C}$, and improved the thermal stability of the membranes, in particular increased the onset of $-\text{SO}_3\text{H}$ group splitting-off temperature [35]. Sulfonated biphenol-based poly(arylene ether sulfone) copolymers (sBPSH) showed lower water transport compared to Nafion[®] 117 [36] and this could favorably prevent cathode flooding which often decreases cell performance in long term DMFC operation. The sBPSH membranes displayed drastically lower electro-osmotic drag coefficients than Nafion[®] and other PFSA ionomers [36]. The phenomenon of electro-osmotic drag is coupled with proton transport in aqueous media. It was shown that MEAs based on H_2SO_4 -doped PBI and non-humidified exhibited higher fuel cell characteristics than MEAs based on Nafion[®] 117 [37]. The fuel cell characteristics of MEAs based on H_3PO_4 -doped PBI exhibited high performances at $185\text{ }^{\circ}\text{C}$ even fuelled with hydrogen containing 3% CO [37].

Furthermore polymer blending is a potentially versatile way of tuning the properties to those desirable for fuel cell application. For instance, sulfonated PEK and PSU have been used in blends with PBI, as well as with more weakly basic components such as polyetherimine, polyethylenimine and poly(4-vinylpyridine) [5,38]. The performance of the sPEEK membranes could be improved also by incorporating hydrated inorganic oxides such as SiO_2 [34], which can suppress the swelling behavior and increase the operating temperature [30]. PSUs are chemically stable, main-chain arylene polymers with broad applications as basis materials for both porous and dense polymeric membranes [39]. Sulfonation with chlorosulfonic acid or the $\text{SO}_3/\text{triethylphosphate}$ complex leads to sulfonated PSU (sPSU),

which can be used as a cation-exchange membrane [40]. Membranes based on pure PSU are known to be very brittle. However, covalently cross-linked blend membranes from sPSU with sPEEK showed a markedly reduced dry-brittleness [29]. Also a composite membrane on the basis of sPSU polymers and the PTFE reinforcement technique showed a remarkable single cell performance, which is very promising for PEMFC application [35]. The DMFC performance of differently cross-linked membranes (ionically, covalently or covalent-ionically), based on sPEK and sPSU, was similar and comparable with that of Nafion[®] 105, although the methanol permeability of the polyary-blend membranes was a factor 2 to 2.4 lower than that of Nafion[®] 105 [41].

A general problem of the most approaches for development of novel, non-fluorinated fuel cell membranes is that these polymers and membranes are developed *via* the trial-and-error principle. Therefore there is a strong need for the preparation of novel fuel cell membranes following a fundamental approach, including subsequent investigation of the chemical and thermal stability of the monomers, polymers, membranes and MEAs.

2.2 Direct photolysis

A convenient method for producing oxygen radicals in the laboratory is UV photolysis of aqueous solutions of H₂O₂. Since aromatic monomers absorb UV radiation as well care has to be taken to distinguish HO[•] radical reactions from direct photochemical cleavage. The possible primary photochemical processes which may occur on excitation of molecules are: dissociation into radicals; intramolecular decomposition into molecules; intramolecular rearrangement; photoisomerization; hydrogen-atom abstraction; photodimerization; photosensitised reaction and finally “external” or “internal” electron transfer [42].

The major primary photodissociative processes in the aldehydes, ketones and alcohols photolysis have been well described previously including also the so called “Norrish type II split” in aldehydes and ketones with a γ -hydrogen atom [42]. The “Type II” split in ketones occurs with a good efficiency when one of the alkyl groups is replaced by an aromatic ring, as in butyrophenone, or by a cycloalkyl group as in menthone. Furthermore the quantum yield of this process in butyrophenone was strongly affected by certain *ortho* and *para* substituents. Membranes based on aromatic hydrocarbons have found application in fuel cells, as mentioned in the previous subchapter, therefore we concentrate on the photochemistry of aromatic hydrocarbons.

Photodecomposition modes of the aromatic molecules occur only with low quantum efficiencies in the first absorption bands, $\phi \approx 0.01$ - 0.0001 or less. In those compounds having alkyl groups attached to an aromatic ring system, exposure to light in the first absorption region may lead to rupture of C–H or C–C bonds to form benzyl-type radicals (Fig. 1a) [43]. In compounds having an ethyl side chain, molecular elimination of H₂ may occur (Fig. 1c). In benzene, and presumably in its alkyl-substituted derivatives, the net effect of ring rupture occurs on irradiation at 2537 Å in rigid glass at 77 K. In ethanol-containing matrices a substituted triene appears to be the product, as shown in Fig. 1d. The 2537 Å irradiation of alkyl-substituted benzenes in the gas phase or in solution induces at low efficiency an interesting 1,2 shift of an alkyl group. Isotopic labelling experiments show that the rearrangement is intramolecular; the aromatic ring carbon to which the alkyl group is attached migrates with the alkyl group, presumably through the intermediate formation and reaction of folded Dewar-type ring or tricyclohexene structures, shown as X in Fig. 1e:

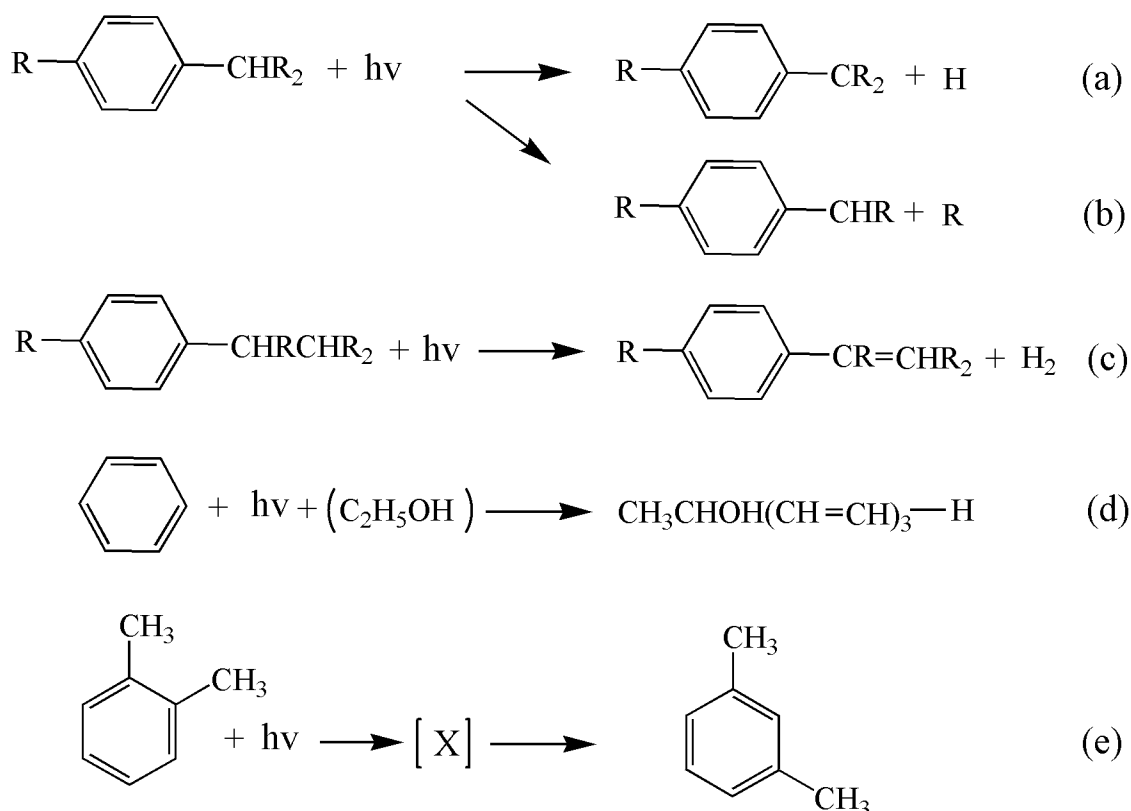


Fig. 1: Primary photodissociative processes in aromatic hydrocarbons [42].

The simple aromatic hydrocarbons such as benzene and toluene undergo a dramatic change in the character of their primary processes when they are irradiated in their second or

third (1849 Å) absorption bands, compared to their spectroscopic and photochemical behaviour in their first band at 2537 Å. A highly efficient photochemical reaction occurs in the vapor phase [42]. The ultimate products at 1849 Å are apparently a high-energy isomer of benzene, which decomposes to carbon and /or polymer and traces of volatile products such as H₂, CH₄, C₂H₆, toluene and C₂- or C₃-substituted benzene. Toluene behaves photochemically and spectroscopically in a similar way. Primary processes were also suggested for ethylbenzene, isopropylbenzene, tert-butylbenzene, cyclopropylbenzene and other derivatives. [42].

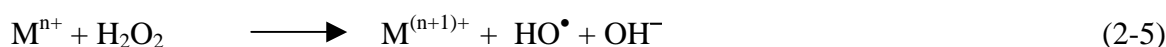
2.3 HO• radical initiated degradation

To ensure long term durability of the new materials, additional investigations are necessary about possible degradation mechanisms. HO• and HOO• radicals originating from oxygen diffusion through the membrane and incomplete reduction at the fuel cell cathode are held responsible for these degradation reactions [44,45]. Hydroxyl and superoxide radicals are regular intermediates of the cathode reaction and this is unproblematic as long as they remain attached to the catalyst surface. The intermediate product of oxygen reduction, hydrogen peroxide, can be formed in sufficient amounts on the catalyst surface at the cathode side of the cell [46]. In the presence of noble metals and at elevated temperatures H₂O₂ decays into hydroxyl radicals which attack the membrane [47]. Because of partial oxygen crossover through the membrane degradation can take place also at the anode. In a prior long-term fuel cell performance study on radiation-grafted FEP-g-polystyrene (FEP-g-PSA) type membranes, it was shown that the rate of radical-initiated degradation increases with increasing gas crossover [45]. This indicates that the stability of the highly cross-linked membranes is not only caused by cross-linking of the polystyrene chains, which slows down the loss of –SO₃H from the membranes, but also by reduced gas crossover and, therefore, reduced HOO• formation. High degrees of cross-linking (more than 12%) could improve the stability, however, the simultaneous increase of membrane resistance might not be tolerable [22]. The optimum membrane thickness, as a compromise between gas crossover and resistance, must be found.

Recent publications have suggested that the location to radical attack in a MEA is at the cathode (oxygen) side [48,49,50,51,52,53]. This mechanism is based on the premise that the oxygen reduction reaction at the cathode of the PEMFC proceeds *via* a parallel pathway where a two-electron reduction of oxygen occurs simultaneously with formation of H₂O₂ intermediates along with the four-electron reduction to H₂O [54]:



Other experiments, however, gave evidence that the main degradation is associated with loss of sulfonic acid groups and occurs at the anode [18,55]. The mechanism involves diffusion of molecular oxygen through the membrane (“crossover”) which reacts with atomic hydrogen chemisorbed on the surface of the anode platinum catalyst, thus producing radicals. The possible reactions involved in this mechanism are as follows:



This proposed mechanism has been suggested on the basis of tests in regular fuel cell setups under open-circuit potential conditions in previous publications [44,56]. Me^{n+} is a transition metal ion that can be oxidized further, for instance Fe (II), Cu (I) or Ti (III), and can activate oxidative cleavage of hydrogen peroxide, as in the Fenton mechanism. It was suggested that the hydroperoxyl radical, HOO^\bullet , is the species that attacks the membrane [18]. Some of the transition metal ions can react directly with the sulfonic acid groups of the membrane, thus providing an additional degradation pathway [21].

The dominating reaction in degradation processes of unsaturated polymers is the addition of HO^\bullet to the aromatic rings, preferentially in the *ortho* position to alkyl- and RO-substituents (since in sulfonated PS, PSU, PEK and FEP-g-PSA the *para* position is substituted and thus blocked) (Fig. 2) [47]. It demonstrates the combined *ortho* activation by these substituents and the *meta* directing effect of the $-\text{SO}_3\text{H}$ group in electrophilic addition reactions.

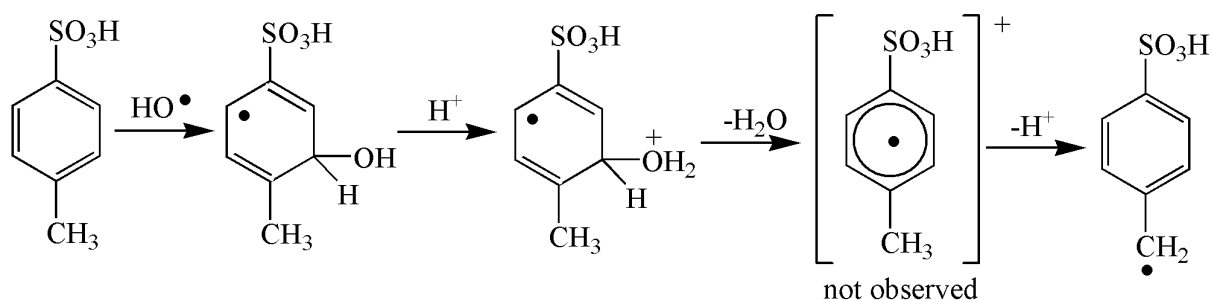


Fig. 2: Formation of benzyl radicals by acid catalysis from hydroxycyclohexadienyl radicals [47,57].

A crucial point is the acid catalysed water elimination from hydroxycyclohexadienyl adducts (Fig. 2). This process requires the presence of labile benzylic α -H atoms, thus it is not relevant for PSU or PEK type membranes but important in the case of FEP-g-PSA. In an endothermic process this can lead to chain scission (“reverse polymerization”) and thus to loss of $-\text{SO}_3\text{H}$ groups. When water is eliminated from cyclohexadienyl radicals in polystyrenesulfonate, radical intermediates are identified by UV-VIS and EPR under acidic conditions [58]. They can act as centers of degradation reactions in all of the newly developed polymers. The lack of α -H atoms certainly contributes to a much better long term behavior [44].

Oxygen has a strong tendency to add directly to cyclohexadienyl-like adducts, forming peroxy radical intermediates, which can lead to higher hydroxylated products and finally to bond breaking reactions as shown in Fig. 3. A degradation mechanism of sPEEK and sPSU, which leads to the loss of sulfonic acid groups was proposed based on ab-initio calculations [59]. Various OH-aromatic-OO type radicals could be formed and they can act as direct precursors for the loss of sulfonic acid groups. Alternatively, they can transform into bicyclic and/or epoxy-type radicals, which are labile towards the detachment of the sulfonic acid group [59].

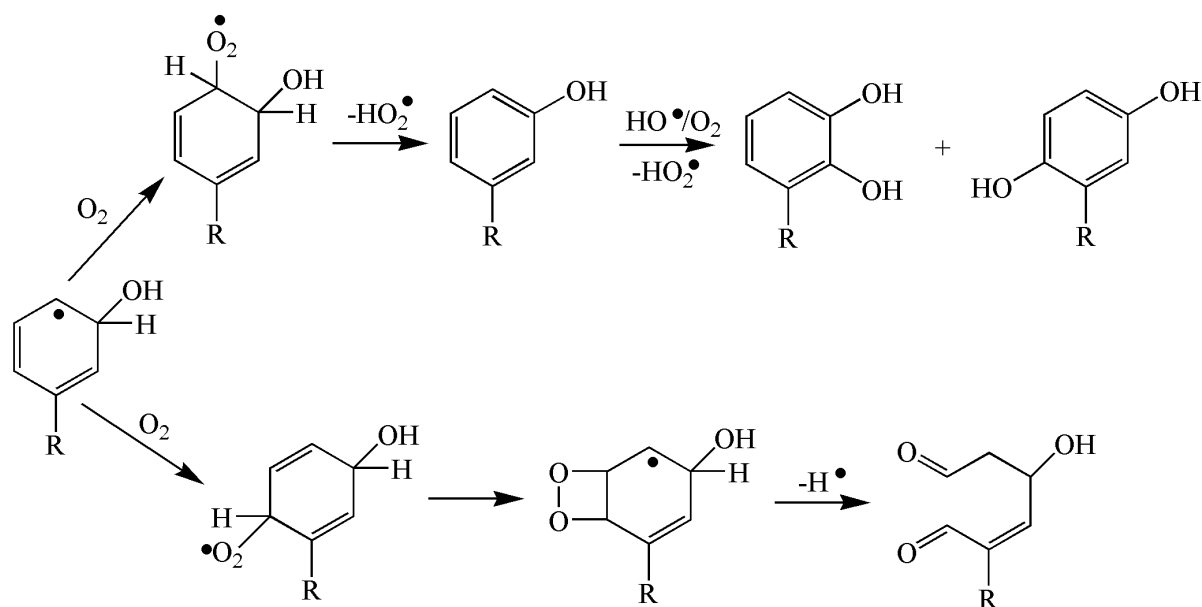


Fig. 3: Mechanisms for consecutive reactions of hydroxycyclohexadienyl radicals with oxygen leading to different phenolic compounds and to bond breaking [47,57].

Another crucial point is the C–O–C bond breaking, initiated by attack of HO[•]. This degradation mechanism is of relevance for the polymers with phenoxybenzene ether bridges like PSU or PEK. However, phenoxyl radicals are not observed at pH < 5, suggesting that the degradation may be avoided as long as the local pH is sufficiently low [47]. An alternative possibility could be the ultimate scission of the ether link, after the addition of HO[•], by *ipso*-attack of HO[•] to the –OR group due to the activating effect of hydroxyl substituent in the *ortho* position to –OR [53]. Fig. 4 summarizes possible sites from which degradation can start for several polymers [57].

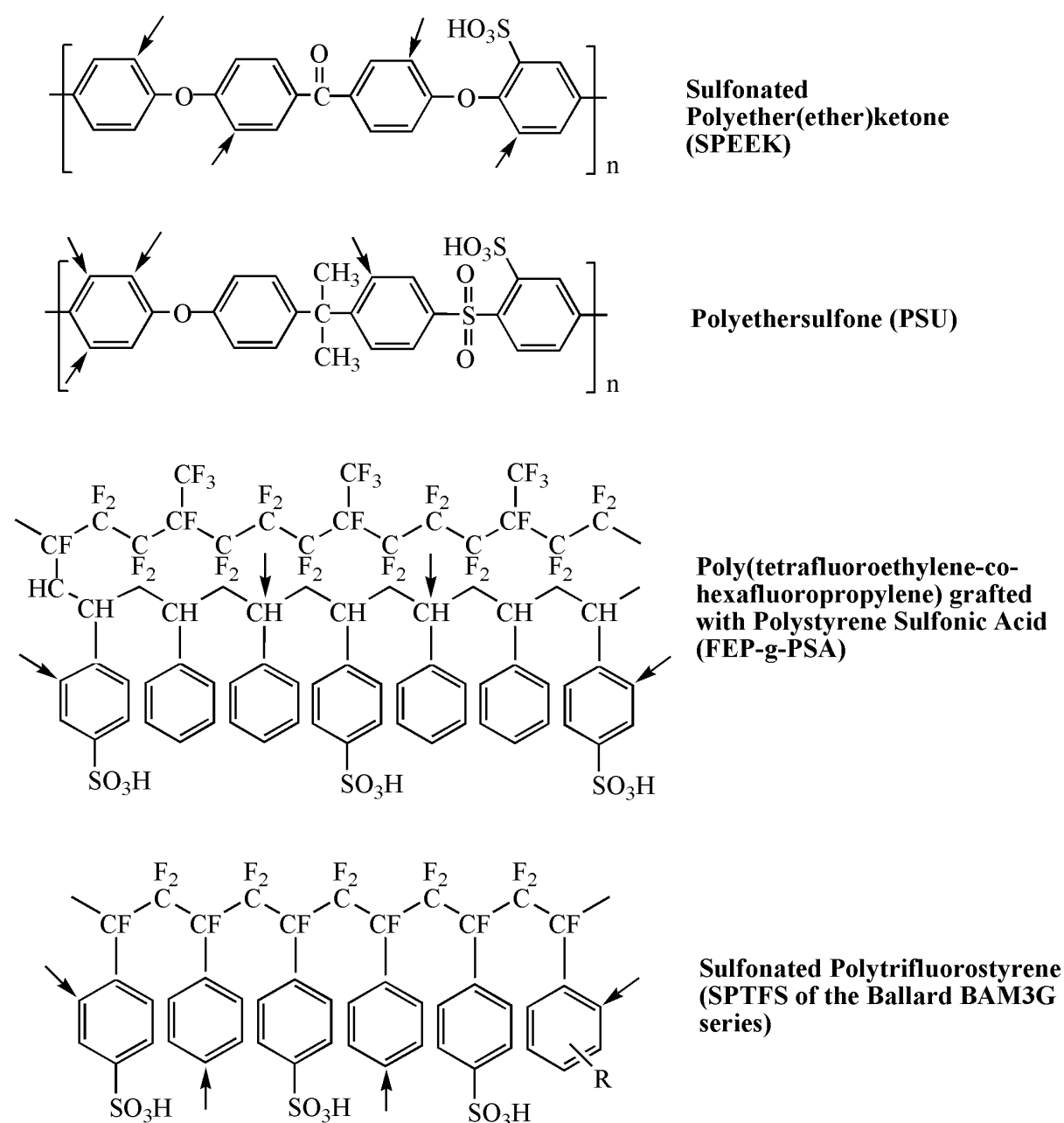


Fig. 4: Possible sites for HO[•] radical attack on various polymers used in proton-conducting membranes [57].

On an experimental scale, the generation of HO[•] and HOO[•] radicals can be achieved by a variety of different methods, for instance by direct photochemical [60,61] or photocatalytic [62] degradation of H₂O₂, also by e⁻ irradiation [63,64] or sonolysis [65] of aqueous solutions, etc. A convenient method for producing oxygen radicals in the laboratory is UV photolysis of aqueous solutions of H₂O₂ [66], and the main expected reactions are:



which react further via



and other reactions as detailed in Table 2. Since aromatic monomers absorb UV radiation as well care has to be taken to distinguish HO[•] radical reactions from direct photochemical cleavage.

Table 2: Rate constants for reactions of HO[•] radicals [67].

Reaction	Rate constant, $k/10^9 \text{ M}^{-1} \text{ s}^{-1}$
a: pH>11.7: $\text{HO}^\bullet + \text{HO}_2^- \rightarrow \text{H}_2\text{O} + \text{O}_2^{\bullet-}$	7.5
b: pH<11.7: $\text{HO}^\bullet + \text{H}_2\text{O}_2 \rightarrow \text{H}_2\text{O} + \text{HO}_2^\bullet$	0.027
c: $\text{HO}^\bullet + \text{O}_2^{\bullet-} \rightarrow \text{HO}^- + {}^1\text{O}_2$	8
d: pH=11.0: $\text{HO}^\bullet + \text{OH}^- \rightarrow \text{O}^{\bullet-} + \text{H}_2\text{O}$	12
e: $\text{HO}^\bullet + \text{HO}^\bullet \rightarrow \text{H}_2\text{O}_2$	5.5
f: $\text{O}^{\bullet-} + \text{HO}_2^- \rightarrow \text{HO}^- + \text{O}_2^{\bullet-}$	0.4
g: $\text{O}_2^{\bullet-} + \text{O}^{\bullet-} + \text{H}_2\text{O} \rightarrow 2 \text{HO}^- + {}^1\text{O}_2$	0.6

The formation of radical species from the attacked substrate, for instance RH, can occur by H-abstraction, and the polymer-derived R[•] radicals can initiate a degradation cascade:



The radical intermediates of the HO^\bullet initiated degradation of aromatic group containing membranes are of the cyclohexadienyl, benzyl, phenoxy or *ortho*-semiquinone type. These radicals are observable by ESR and distinguishable by means of their hyperfine splittings and g -values (see Fig. 5).

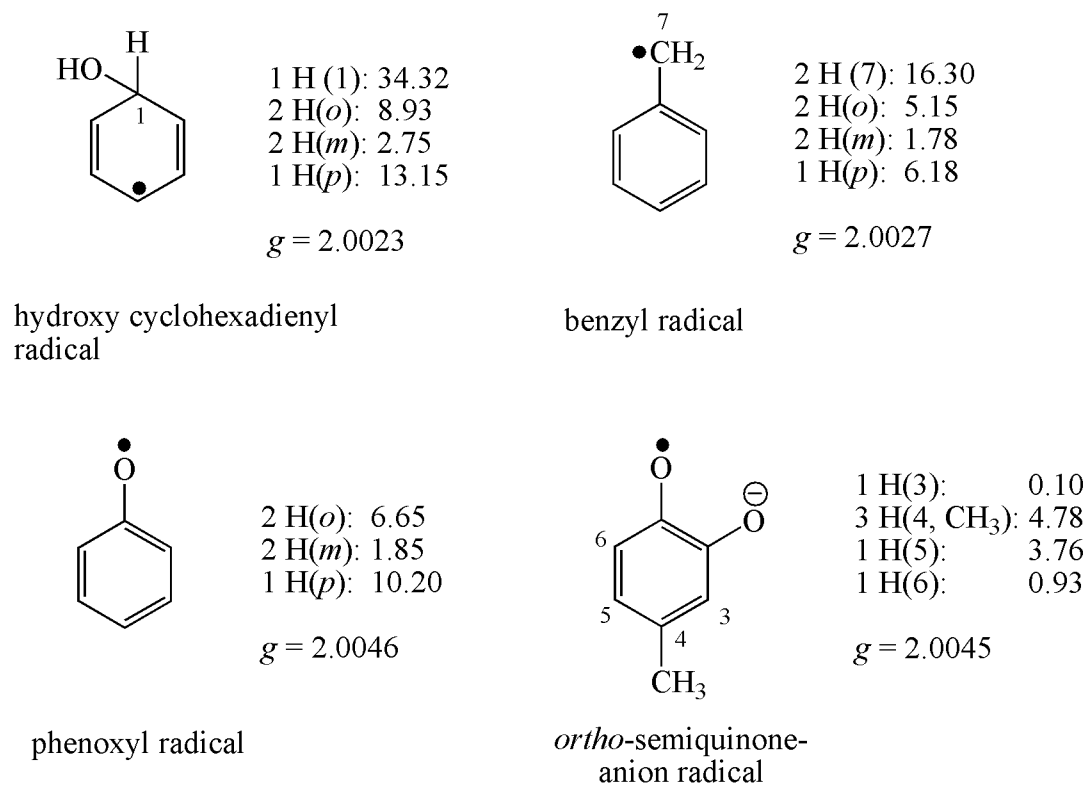


Fig. 5: ESR hyperfine splittings and g -values for radical intermediates of the reaction of HO^\bullet radicals with aromatic hydrocarbons [68].

Due to fast relaxation HO^\bullet itself is not observable by ESR in solution. Based on the $\text{p}K_{\text{S}}$ values of H_2O_2 (11.7), HO^\bullet (11.9) and HOO^\bullet (4.8) the main reactive species below pH 10 is HO^\bullet , above pH 13 it is $\text{O}^{\bullet-}$ and $\text{O}_2^{\bullet-}$, while at $10 \leq \text{pH} \leq 13$ we have a strongly pH-dependent mixture [47]. Relatively little quantitative information is available for HOO^\bullet , but it is known to be significantly less reactive than HO^\bullet which reacts by hydrogen abstraction or by addition to unsaturated bonds. The anionic species are less efficient in abstraction reactions but add readily to double bonds or aromatic rings. Since both H_2O_2 and HO^\bullet deprotonate near pH 11.7, the new reactive species is $\text{O}^{\bullet-}$ which can abstract H-atoms but shows little tendency for addition, but in particular, $\text{O}_2^{\bullet-}$ or $^1\text{O}_2$ are formed which are held mainly responsible for the formation of phenoxy and semiquinone-type aromatic polyoxy radicals [47,69]. Investigations at low pH are particularly relevant for understanding degradation in PEFCs, but one should keep in mind that the chemistry depends strongly on pH, a fact that is highly

significant in view of possible pH inhomogeneities in fuel cells under conditions of fuel starvation at high currents or when parts of the anode are flooded by water [21].

Typical rate constants for reactions with model compounds of relevance in the present context are collated in Table 3. They show that HO[•] addition occurs with rate constants close to the diffusion controlled limit, H-abstractions are slower by less than an order of magnitude, while O^{•-} can abstract H with a similar efficiency but does not undergo addition.

Table 3: Rate constants for reactions of HO[•] and O^{•-} radicals with different substrates [67].

Substrate	Reaction of HO [•]		Reaction of O ^{•-}	
	Product	k/10 ⁸ M ⁻¹ s ⁻¹	Product	k/10 ⁸ M ⁻¹ s ⁻¹
CH ₃ OH	•CH ₂ OH	9.7	•CH ₂ O ⁻	7.5
C ₆ H ₅ OH/C ₆ H ₅ O ⁻	C ₆ H ₅ (OH) ₂	66	C ₆ H ₅ O [•]	6.5
C ₆ H ₅ CH ₃	C ₆ H ₅ (OH)CH ₃ +C ₆ H ₅ •CH ₂	30	C ₆ H ₅ •CH ₂	21
Benzophenone	adduct	88		
Benzenesulfonic acid	adduct	16		
Benzenesulfonate ion	adduct	30		

ESR spectroscopy is the major method of study, because of its sensitivity and specificity for the detection of radical species. In the centre of interest are the reaction mechanisms which are accessible *via* the structures of free radical intermediates, and the identification of fuel cell operating conditions which may lead to enhanced free radical production.

2.4 Radiation grafting

Radiation grafting is a well-established technique for the preparation of polymer electrolyte membranes for fuel cells and other electrochemical applications. The preparation of membranes by radiation grafting has the advantage of permitting the use of a wide variety of base films and monomers, which may be tailored for the desired end-use, with the flexibility of introducing a controlled quantity of functional groups [4,70,71]. As the method has been based on low-cost starting materials and established process technologies, it offers the prospect of cost-competitive membranes for the PEFC [72].

Among many available grafting methods, radiation-induced grafting of commercially available polymer films followed by sulfonation is one of the promising synthesis strategies [44,45,73]. Essentially, this is a three step process, consisting of irradiation, grafting and sulfonation, to convert a non-conducting commodity polymer film into a proton conducting membrane (Fig.6).

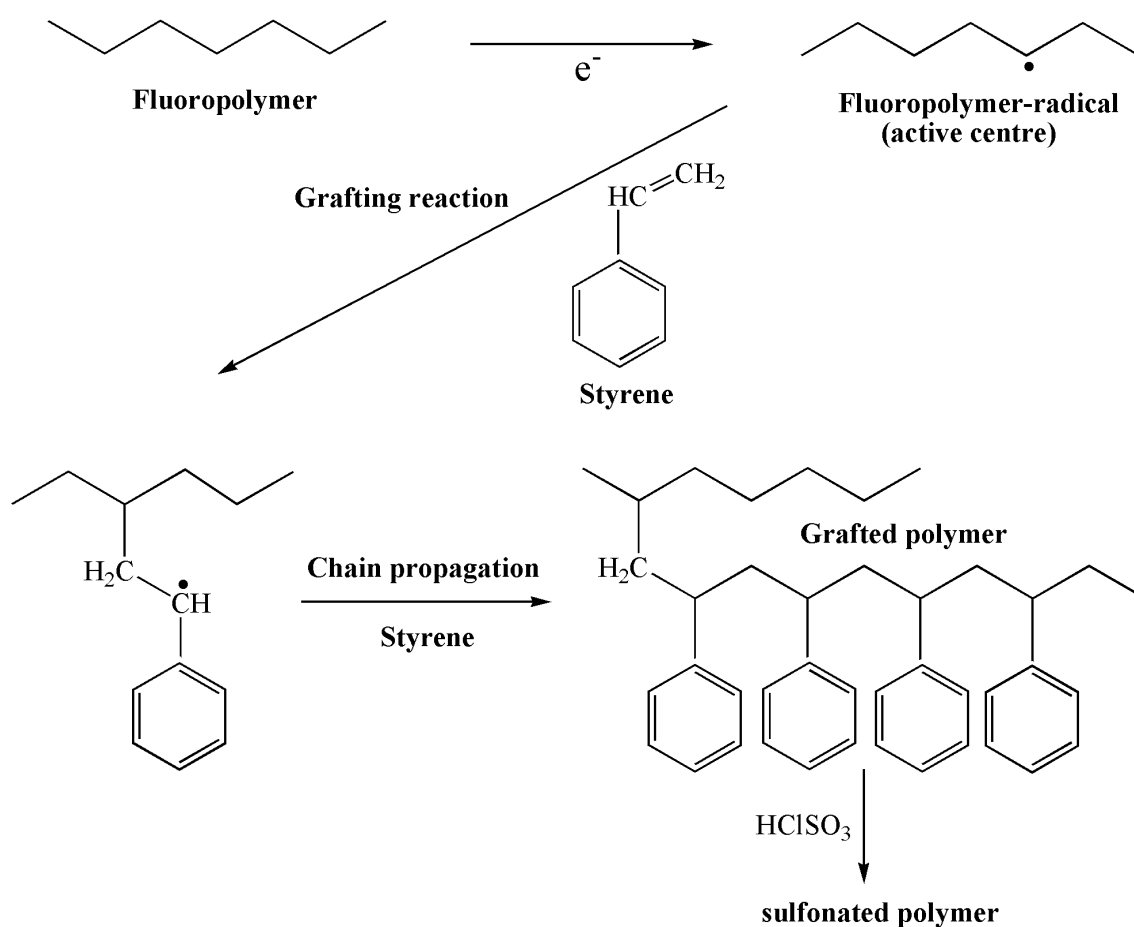


Fig. 6: Membrane preparation by pre-irradiation grafting [74].

The preparation of membranes based on FEP, (poly(ethylene-alt-tetrafluoroethylene)) (ETFE), (poly(vinylidene fluoride)) (PVDF), PTFE and (polytetrafluoroethylene-co-perfluoro(alkyl vinyl ether)) (PFA) has been reported at many occasions using simultaneous and pre-irradiation techniques [74,75,76,77,78,79,80]. The performance, in terms of current-voltage properties of PEFCs containing FEP-based radiation grafted membranes, was comparable to commercially available Nafion[®] 112 membranes of similar thickness and durability of several thousand hours could be demonstrated [4,81]. In addition, FEP-based membranes were optimized for use in DMFCs, and similar performance with Nafion[®] 117 was obtained with methanol crossover reduced by a factor of two [82]. ETFE-based radiation grafted membranes have demonstrated lifetimes on the order of 1000 h before significant membrane degradation occurs and the polarization properties of PEFCs using the latter membranes compare very favorably with those obtained using commercial and experimental Nafion[®] membranes of approximately similar thickness [83,84]. PVDF and ETFE (both 50 μm) based membranes with graft levels of 33 and 34%, respectively, showed MEA performance identical to Nafion[®] 115 at a cell temperature of 80 $^{\circ}\text{C}$ [85,86].

Due to their inertness, it is difficult to modify or functionalize most fluoropolymers. Nonetheless, high energy radiation like electron beam or gamma rays can be used to generate radical centers in fluoropolymers. These reactive sites can then be used to modify the fluoropolymer structure and properties by introducing specific functional groups. In the pre-irradiation method, the film is activated in a pre-irradiation step and then grafted with monomer in a subsequent step. The film may be pre-irradiated in the absence of oxygen or, alternatively, in the peroxide method, the base polymers can be irradiated in air [70]. Some of the advantages of radiation graft copolymerization include [87]: (1) the ready variation of the initiation step, for example by (a) creating either primarily carbon-based radical active sites or peroxy- or hydroperoxy based active sites, (b) varying the total irradiation dose or (c) varying the dose rate; (2) initiation under conditions where conventional methods fail (low temperature, solid-phase polymerization); (3) homogeneous distribution of introduced radiation defects; (4) lack of need for chemical initiators or catalysts and (5) the materials can be modified in an already prefabricated form.

In the pre-irradiation grafting of styrene to fluoropolymers, the films are not swollen in styrene. The reaction then proceeds by a grafting front mechanism [70]. In this mechanism grafting initially occurs only at the surface which is in intimate contact with the monomer solution, as shown in Fig. 7a. The grafted surface region swells in monomer and thus the monomer diffuses further into the film interior and reacts with more radicals (7b). The two

grafting fronts continue to move further into the film interior until they meet and the membrane is grafted through (7d). For applications in which ions should be conducted from one side of the membrane to the other, as, for example in electrochemical cells, grafting should proceed to a point at which a homogeneous grafting level is achieved throughout the film thickness (7f) [87].

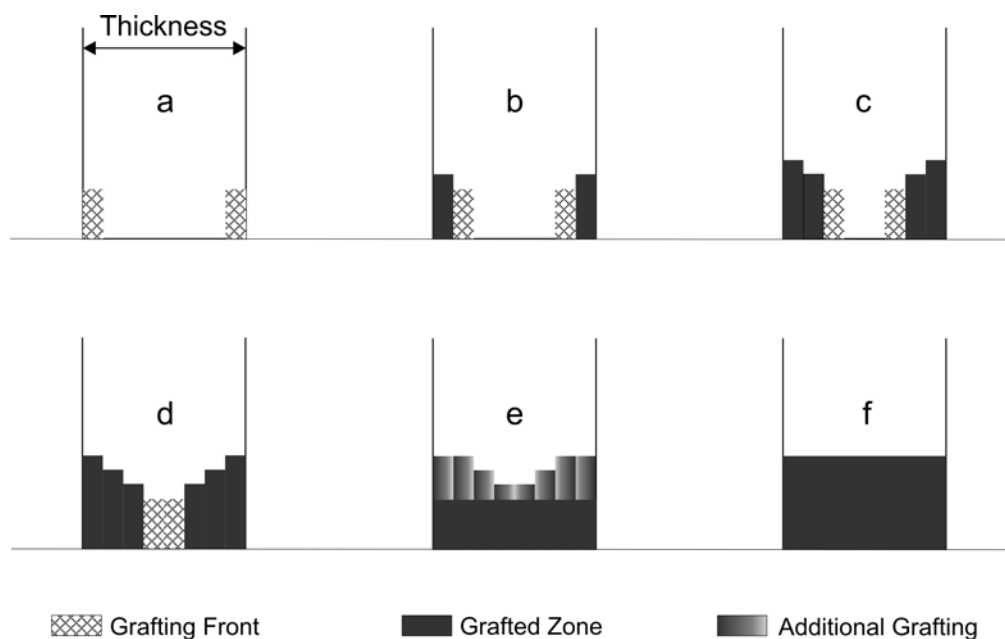


Fig. 7: Simplified qualitative view of grafting front mechanism [87].

If radiation grafting is monomer transport limited, as in the cases described by the grafting front mechanism [70,73], the base polymer film properties would be expected to have a significant effect on monomer transport into the film and thus the grafting process. Molar mass, crystallinity and orientation are all known to have important influences on diffusion in polymer films. It is therefore important to understand how base polymer film and radiation processing properties affect the extent and rate of grafting so that grafted film and membrane preparation can be carried out rapidly and reproducibly.

Analytical tools are needed to characterize and monitor the material during synthesis with the aim to understand the influence of the many experimental parameters on the membrane properties. ESR is a suitable spectroscopic technique to identify the nature of radiation generated radicals in organic polymers, and to monitor their concentration *in-situ* during the grafting process. Some *in-situ* ESR measurements have been carried out during the radiation grafting of fluoropolymers with styrene [76,77,88]. These investigations have focused on identifying the grafting sites and their associated radical species, observing and quantifying

the propagating radical species, and quantifying the rates of radical decay during grafting. Unfortunately, the propagating styryl radical species do not appear to have been observed successfully in these investigations. It has been proposed that they are not identified because they are present only at very low concentrations due to their rapid reaction [76,88]. This result contrasts however with the ready observation of propagating radical species when other monomers like methyl methacrylate (MMA) are used to graft fluoropolymers [88]. Curiously, at least in solution, the reported polymerization rates of MMA are typically anywhere from 2 to 10 times higher than for styrene [89]. Propagating styryl radicals are also readily observed during the solution polymerization of styrene [90]. With regards to the decay in radical content during grafting it has been reported that decay is faster in the presence of styrene under inert atmosphere than under inert atmosphere alone in both ETFE and PVDF films [76,77]. E-beam radiation was used in the ETFE study, and gamma radiation was used in the PVDF study. For ETFE a period of rapid radical decay was followed by a second period of much slower radical decay. No underlying cause for this behavior has been proposed to-date, but it was observed that the onset of this second slower phase corresponded to the first point in time at which the film is grafted through its thickness and the two grafting fronts meet in the film center [88].

In spite of the earlier work using ESR to study the radiation grafting of styrene onto fluoropolymers, several aspects remain to be investigated and clarified. For example, a clear overall understanding is not possible because a variety of different irradiation sources and doses were used in these cited earlier investigations. Therefore, the relative rates of radical decay are not known for the same polymer type but irradiated under air versus inert atmosphere, nor has the radiation grafting of different polymers irradiated in the same manner and with the same dose been compared.

2.5 Non-fluorinated and perfluorinated alkyl and alkyl-peroxy radicals

In radiation grafting of polymer films with styrene for fuel cell applications it is important to control whether the polystyrene chain is grafted onto a peroxy or a carbon centered radical, because of the different bond strengths which prevent the grafted chain to cleave off. Among the fluoropolymers, FEP is advantageous in terms of high radiation resistance, which provides the possibility for applying a wide range of irradiation doses [91].

Since gamma irradiation is a common method for sterilization of medical implants, examination of free radical reactions in ultra-high molecular weight polyethylene (PE) has become an important part of research in orthopedic industry. It is thought that the common cause of implantation failure is oxidative degradation of PE [92]. PE itself has been used as a benchmark in the development of theoretical techniques, and much experimental data, including X-ray and neutron diffraction studies of the crystalline material, are available [93-95]. Furthermore, a proton conducting membrane is a key component in a polymer electrolyte membrane fuel cell. It was proposed that HO^\bullet and HO_2^\bullet radicals originating during oxygen reduction at the cathode side are responsible for membrane degradation [96]. An investigation of possible free radical formation is therefore important for both FEP and PE applications. Thus thermodynamic properties of small alkyl and alkyl-peroxy radicals are studied to model primary, secondary and tertiary radicals in non-fluorinated and perfluorinated polymers. Bond dissociation energies are calculated for the above mentioned radicals and since alkoxy radicals may also occur in these systems, they are also considered. Due to the facts that F is highly electronegative, and that the steric repulsion between the neighboring fluorine atoms is stronger than that between the hydrogen atoms, optimized geometries and charge distributions are also compared (see subchapters 6.1 and 6.2).

Polymer degradation involves most frequently transient radicals. For an identification of these radicals one needs to distinguish features from *g*- and hyperfine anisotropy to obtain the corresponding tensors and analyse the local structure. It is therefore important to understand the relation between geometry and hyperfine coupling parameters. Pronounced spin polarization effects lead to unexpected behaviour of the hyperfine anisotropy. This is demonstrated by comparison of the parameters of $\text{CF}_3^\bullet\text{CF}_2$, both in a fully optimized and in a forced planar conformation, with those of the analogous non-fluorinated $\text{CH}_3^\bullet\text{CH}_2$ radical (see subchapters 6.3 and 6.4). The study is extended briefly to the fluorinated and the non-fluorinated 1-propyl radicals and is based again on density functional calculations.

The famous McConnell relations [97] were derived and routinely used for α and β -proton coupling constants, but occasionally the treatment was extended to other nuclei like ^{13}C or ^{14}N . One may be tempted to tacitly assume that it holds also for ^{19}F since F is a single valence atom and therefore a formal substitute for H. While alkyl substitution affects the planarity at the radical centre only slightly it has long been known that fluorine substitution at the radical centre leads to severe non-planarity that reaches close to tetrahedral geometry for the $^\bullet\text{CF}_3$ radical [98]. Furthermore, it was shown that F can induce strong and sometimes counter-intuitive charge polarization in molecules [99].

Chapter 3

3 EXPERIMENTAL AND THEORETICAL METHODS

This chapter consists of three subchapters. The first two characterize the ESR and UV-VIS techniques which are employed in our studies. In the third one a brief introduction into the *ab-initio* DFT approach used for our calculations is supplied.

3.1 Electron Spin Resonance

Electron Spin Resonance (ESR) or Electron Paramagnetic Resonance (EPR) is the study of molecules and ions containing unpaired electrons by observing the magnetic fields at which they come into resonance with monochromatic radiation. In general, the ESR deals with the interaction of electromagnetic radiation with magnetic moments which arise from the electrons. Electromagnetic radiation may be regarded classically as coupled electric (E) and magnetic (B) fields perpendicular to the direction of propagation. Both oscillate at some frequency ν , within the theoretical range 0 (DC) to infinity. In EPR the commonly used frequency range is 10^9 - 10^{11} s⁻¹ (1 - 100 GHz) [100]. Magnetic fields of about 3000 G (the value used in most commercial ESR spectrometers) correspond to resonance with an electromagnetic field of frequency 10 GHz and wavelength 3 cm. Because 3 cm radiation falls in the X-band of the microwave region of the electromagnetic spectrum, ESR is a microwave technique [101].

Each electron possesses an intrinsic magnetic-dipole moment that arises from its spin. In most systems electrons occur in pairs such that the net moment is zero. Hence only species that contain one or more unpaired electrons possess the net spin moment necessary for suitable interaction with an electromagnetic field.

A magnetic-dipole moment in an atom or molecule (neutral or charged) may arise from unpaired electrons, as well as from magnetic nuclei. The magnetic-dipole moments of these particles in turn arise, respectively, from electronic or nuclear angular momenta. Hence one of the fundamental phenomena to be understood in EPR spectroscopy is the quantization of angular momenta.

The unique feature of ESR spectroscopy is that it is a technique applicable to systems in a paramagnetic state (or which can be placed in such a state), that is, a state having net electron angular momentum (usually spin angular momentum). Either the species exists in a paramagnetic ground state or it temporarily may be excited into a paramagnetic state, for instance by irradiation. Thus, in principle, all atoms and molecules are amenable to study by ESR. Typical systems that have been studied include:

- free radicals in the solid, liquid, or gaseous phases;
- transition metal ions including actinide ions;
- various point defects (localized imperfections) in solids;
- systems with more than one unpaired electron (triplet-state systems, biradicals);
- systems with conducting electrons (semiconductors and metals).

3.1.1 The g -value

The spin magnetic moment interacts with the local magnetic field, and the resonance condition is normally written:

$$h\nu = g\mu_{\beta}B \quad (3-1)$$

where g is the **g -value** of the radical or complex [101]. This expression with a single numerical value of parameter g is applicable only to systems that behave isotropically. With anisotropic systems, variability of \tilde{g} with orientation relative to B is required:

$$B_{eff} = (1 - \sigma)B = \left(\frac{\tilde{g}}{g_e} \right) B \quad (3-2)$$

where $B_{eff} = B + B_{loc}$ is the total field effective at the electron being considered; σ is the analog of the “chemical shift parameter” used in Nuclear Magnetic Resonance (NMR) and \tilde{g} is the effective Zeeman tensor used by ESR spectroscopists [100]. Furthermore, the resonant field value is a function of the field orientation relative to the crystal (or molecular) axes. For some purposes it is convenient to append subscripts on g to specify the field orientation defining it. If the principal axes of the paramagnetic entity are labeled X, Y and Z, g_x is to be interpreted for a simple case as $h\nu/\mu_{\beta}B_x$, that is, the g -factor for B along the X axis of the magnetic entity. A truly isotropic system is one for which $g_x = g_y = g_z$. On the other hand, for paramagnetic species in a liquid system of low viscosity, the measured (apparently isotropic) g factor is to be regarded as an effective value averaged over all orientations.

It is important to distinguish between a space averaged and a time averaged quantity. In the case of paramagnetic species in solution, each entity exhibits a time averaged response, and hence the resultant spectral line is narrow. However, if a crystal were ground into a powder, each center exhibits its own resonance position, depending on its orientation, and the resultant spectrum is broad since the resonance is an envelope representing a weighted distribution of all possible resonance fields.

Many carbon centered organic radicals have g -values close to 2.0027; inorganic radicals have g -values typically in the range 1.9 to 2.1; d -metal complexes have g -values in a wider range (for instance, 0 to 4). The deviation of g from $g_e=2.0023$ depends on the ability of the applied field to induce local electron currents in the radical, and therefore its value gives some information about electronic structure. However, because g -values differ very little from g_e in many radicals (for example, 2.003 for H, 1.999 for NO₂, 2.010 for ClO₂) its main use in chemical applications is to aid the identification of the species present in a sample [101].

3.1.2 Hyperfine structure

The most important feature of ESR spectra is their hyperfine structure, the splitting of individual resonance lines into components. The source of the hyperfine structure in ESR is the magnetic interaction between the electron spin and the magnetic dipole moments of the nuclei present in the radical. There are two contributions to the interaction: dipole-dipole interaction and Fermi contact interaction. In general, a spin- I nucleus splits the spectrum into $2I+1$ hyperfine lines of equal intensity. When there are several magnetic nuclei present in the radical, each one contributes to the hyperfine structure. In the case of equivalent protons (for example, the two CH₂ protons in the radical CH₃•CH₂) some of the hyperfine lines are coincident. It is not hard to show that, if the radical contains N equivalent protons, then there are $N+1$ hyperfine lines with a binomial intensity distribution (that is, the intensity distribution given by Pascal's triangle) [101]. Therefore the hyperfine structure of an ESR spectrum is a kind of fingerprint that helps to identify the radical present in a sample. Moreover, because the magnitude of the splitting depends on the distribution of the unpaired electron near the magnetic nuclei present, the spectrum can be used to map the molecular orbital occupied by the unpaired electron.

3.1.3 Hyperfine coupling constants

Magnetic nuclei are sensitive probes of molecular electronic structure. Magnetic resonance methods have therefore become the standard methods for structure determination of organic molecules and even of proteins. In NMR the parameters of interest are the chemical shift tensors and the isotropic and dipolar spin-spin coupling constants. In a completely analogous way, ESR derived g -tensors and isotropic (Fermi contact) and dipolar nuclear hyperfine coupling constants are being used for local structural and conformational analysis around the unpaired electron of organic radicals. The hyperfine coupling constant of a nucleus is proportional to the electron spin density at the nucleus. The nuclei probe the spin density distribution of a free radical.

3.1.3.1 Electron and spin density, spin population and spin polarization

The total electron (charge) density is the sum of all one-electron densities over all orbitals:

$$\rho^e(r) = \rho^\alpha(r) + \rho^\beta(r) \quad (3-3)$$

The total spin density is the difference of spin *alpha* minus spin *beta* one-electron densities summed over all orbitals:

$$\rho^s(r) = \rho^\alpha(r) - \rho^\beta(r) \quad (3-4)$$

Molecular orbitals (MOs) Ψ_j are normally represented by a linear combination of Atomic Orbitals (AO):

$$\Psi_j = \sum_i c_{ij} \phi_{ij} \quad (3-5)$$

The one-electron population of an MO at the atom i is the one electron density integrated over the entire AO:

$$\rho_{ij}^e = \int \rho_{ij}^e(r) d\tau = \int \Psi_j^* \Psi_j d\tau = c_{ij}^* c_{ij} = |c_{ij}|^2 \quad (3-6)$$

The total electron population of an MO at the atom i is the sum of all one-electron densities at the atom (summation over all Mos j):

$$\rho_i^e = \sum_j \left(|c_{ij}^\alpha|^2 + |c_{ij}^\beta|^2 \right) = \rho_i^\alpha + \rho_i^\beta \quad (3-7)$$

The spin population of an MO at the atom i is the difference of all spin *alpha* minus spin *beta* densities at the atom:

$$\rho_i^s = \sum_j \left(|c_{ij}^\alpha|^2 - |c_{ij}^\beta|^2 \right) = \rho_i^\alpha - \rho_i^\beta \quad (3-8)$$

Spin polarization: the spin in the single-occupied MO of a free radical polarizes the doubly occupied MOs. This has the effect that at certain atoms there is more electron spin *alpha*, at others there is more electron spin *beta* in doubly occupied MOs. Spin polarization can occur without changing the atomic charge when some spin *alpha* is replaced by spin *beta*.

3.1.3.2 McConnell relations for α and β -nuclei

Decades ago, McConnell established two important relations [97], the first one describing the proportionality of the isotropic hyperfine coupling constant a^α of nuclei which are directly bound to a planar radical centre carrying an electron spin population ρ_π

$$a^\alpha = Q^\alpha \rho_\pi \quad (3-9)$$

where Q^α is an empirical proportionality parameter.

Hyperconjugation leads to delocalization of a fraction of spin density onto methyl groups in a similar way as by delocalization through a conventional conjugated system. Some of the electron spin density is delocalized onto substituents. The value of ρ_π remaining on the central carbon of a species $X_1 \bullet CX_2X_3$ obeys an empirical cumulative relation:

$$\rho_\pi = \prod_i \left[1 - \Delta_i (X_i) \right] \quad (3-10)$$

The second McConnell relation defines β -nuclei which are separated by two bonds from a radical centre,

$$\langle a^\beta \rangle = \rho_\pi \left[A + B \langle \cos^2(\theta - \theta_0) \rangle \right] \quad (3-11)$$

Here, A was described as a spin polarization term which for protons is usually small and often negligible compared to a hyperconjugative contribution B that transmits spin density to the β -nucleus with an angular dependence relating to the dihedral angle θ between the C–X bond of the β -nucleus X (measured relative to its equilibrium value θ_0) of interest and the direction of the p_z orbital that carries most of the electron spin density. For rotating β -methyl groups, due to their local C_3 symmetry, $\langle \cos^2(\theta - \theta_0) \rangle = 1/2$, the angular dependence gets lost and eqn. (3-11) can be written in a more compact form as:

$$a^{CH_3} = Q^{CH_3} \rho_\pi \quad (3-12)$$

Q^α and Q^{CH_3} are proportionality constants which adopt typical values for given classes of radicals [102]. A value of unity is assigned to ρ_π for the $\bullet CH_3$ radical, but by spin polarization

or hyperconjugation some of the spin population at the central carbon transfers onto each substituent other than H and diminishes ρ_{π} . $\langle \cos^2(\theta - \theta_0) \rangle$ stands for the expectation value that represents a Boltzmann average over ground and excited states of the internal rotational degree of freedom about the $C^{\alpha}-C^{\beta}$ bond. When there is an extensive averaging it is not appropriate to solve $\langle \cos^2(\theta - \theta_0) \rangle$ for θ , but for rigid conditions at low temperatures it is reasonable to use θ for conformational analysis.

3.1.3.3 γ and δ -nuclei

Hyperfine splittings of these nuclei are generally of the order of 1.0 Gauss or less and are often resolved only in solution spectra. Only for fixed and quite special geometrical conditions as they are encountered, e.g. in bicyclic radicals the coupling may be considerably larger.

3.1.4 Spin trapping technique

ESR is considered to be the only method that we can use for directly observing the radicals formed during fuel cell operation. However, the direct detection of the radicals formed is not always possible with ESR. The radicals formed are usually very reactive and have short lifetimes. These properties result in a very low steady state radical concentration, below the limit of ESR detection.

Spin trapping, a technique developed in the 1970's [103], is considered to be a powerful tool to visualize short-lived radicals indirectly. In this technique, a diamagnetic compound, called a spin trap, reacts with a primary radical to form a more stable radical that can accumulate to a high enough concentration for an ESR study. In our experiments 3,5-dibromo-4-nitrosobenzene-sulfonic acid (DBNBS) was used as a spin trap, and the reaction that takes place is the following:

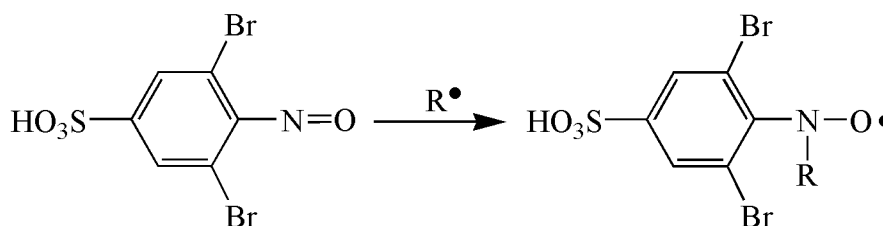


Fig. 8: Reaction mechanism with DBNBS spin trap agent.

The advantage of this kind of spin adduct is that it can yield structural information about the primary radical. Spin trap compounds, such as (5,5-dimethyl-1-pyrroline-*N*-oxide) (DMPO) and (α -(4-pyridyl-1-oxide)-*N*-*tert*-butylnitron) (POBN), have already proven to provide information from the hyperfine splitting parameters [96,104].

3.2 UV-VIS spectroscopy and Beer-Lambert law

UV-VIS spectroscopy is one of the oldest methods in molecular spectroscopy. The definitive formulation of the Bouguer-Lambert-Beer law in 1852 created the basis for the quantitative evaluation of absorption measurements at an early state. Optical spectroscopy is based on the Bohr-Einstein frequency relationship:

$$\Delta E = E_2 - E_1 = h\nu \quad (3-13)$$

This relationship links the discrete atomic or molecular energy states E_i with frequency ν of the electromagnetic radiation. In spectroscopy, it is appropriate to use wavenumber $\tilde{\nu}$ instead of frequency ν leading to equation 3-14:

$$\Delta E = E_2 - E_1 = hc\tilde{\nu}, \text{ where } \nu = \frac{c}{\lambda} = c\tilde{\nu} \quad (3-14)$$

Absorbed or emitted radiation of frequency ν or wavenumber $\tilde{\nu}$ can thus be assigned to specific energy differences or, applying the definition of the “term value” (energy level), to specific energy-level differences:

$$\tilde{\nu} = \frac{\Delta E}{hc} = \frac{E_2}{hc} - \frac{E_1}{hc} = T_2 - T_1 \quad (3-15)$$

Within the overall range of electromagnetic radiation which is of interest to chemists, UV- and VIS-absorption spectroscopy occupies only a very narrow frequency or wavenumber region. Nevertheless, this range is of extreme importance, since the energy differences correspond to those of the electronic states of atoms and molecules [105]. Most UV-VIS spectrometers nowadays cover the range 190 to 900 nm [106].

The ratio of the transmitted intensity, I , to the incident intensity, I_0 , at a given frequency is called the transmittance, T , of the sample at that frequency [107]:

$$T = \frac{I}{I_0} \quad (3-16)$$

It is found empirically that the transmitted intensity varies with the length, l , of the sample and the molar concentration, $[J]$, of the absorbing species J in accord with the Beer-Lambert law [107]:

$$I = I_0 * 10^{-\varepsilon [J] l} \quad (3-17)$$

The quantity ε is called the molar absorption coefficient (or “the extinction coefficient”). The molar absorption coefficient depends on the frequency of the incident radiation and is greatest where the absorption is more intense. For simplification of equation 3-17 the absorbance, A , of the sample at a given wavenumber is introduced [107]:

$$A = \log \frac{I_0}{I} \quad \text{or} \quad A = -\log T \quad (3-18)$$

Then the Beer-Lambert law becomes:

$$A = \varepsilon [J] l \quad (3-19)$$

The product $\varepsilon [J] l$ is known as the optical density of the sample. Equation 3-19 suggests that, to achieve sufficient absorption, path lengths through gaseous samples must be very long, of the order of meters, because concentrations are low. Long path lengths are achieved by multiple passage of the beam between parallel mirrors at each end of the sample cavity. Conversely, path lengths through liquid samples can be significantly shorter, of the order of millimeters or less. The Beer-Lambert law implies that the intensity of electromagnetic irradiation transmitted through a sample at a given wavenumber decreases exponentially with the sample thickness and the molar concentration. The Beer-Lambert law is a limiting law for dilute solutions, i.e. the assertion that the extinction coefficient ε is independent of the concentration of a substance at the given wavelength λ applies only to dilute solutions. ε is no longer constant for concentrated solutions but depends on the refractive index of the solution [108].

3.3 Density Functional Theory and Gaussian calculations

The basis for DFT is the proof by Hohenberg and Kohn that the ground state electronic energy is determined completely by the electron density $\rho(r_i)$ [109]. It is defined as the following multiple integral over the spin coordinates of all electrons and over all but one of the spatial variables [110]:

$$\rho(r_1) = N \int \dots \int |\Psi(x_1, x_2, \dots, x_N)|^2 ds_1 dx_2 \dots dx_N \quad (3-20)$$

The main problem of DFT methods is that although it has been proven that the ground state electronic energy is determined completely by the electron density, the functional connecting these two quantities is not known.

The foundation for the use of DFT methods in computational chemistry was the introduction of orbitals by Kohn and Sham (KS) [111]. The basic idea in the KS formalism is splitting the kinetic energy functional into two parts, one of which can be calculated exactly, and a small correlation term. The key to KS theory is thus the calculation of the kinetic energy under the assumption of non-interacting electrons. In reality the electrons are interacting, however, the difference between the exact and kinetic energy and that calculated by assuming non-interacting orbitals is small. Following the work of Kohn and Sham, the approximate functionals employed by current DFT methods partition the electronic energy into several terms [112]:

$$E = E^T + E^V + E^J + E^{XC} \quad (3-21)$$

where E^T is the kinetic energy term (arising from the motion of the electrons), E^V includes terms describing the potential energy of the nuclear-electron attraction and of repulsion between pairs of nuclei, E^J is the electron-electron repulsion term (it is also described as the Coloumb self interaction of the electron density), and E^{XC} is the exchange-correlation term and includes the remaining part of the electron-electron interactions.

All terms except the nuclear-nuclear repulsion are functions of ρ , the electron density. E^J is given by the following expression:

$$E^J = \frac{1}{2} \iint \rho(\vec{r}_1) (\Delta r_{12})^{-1} \rho(\vec{r}_2) d\vec{r}_1 d\vec{r}_2 \quad (3-22)$$

$E^T + E^V + E^J$ corresponds to the classic energy of the charge distribution ρ . The E^{XC} term in equation 3-21 accounts for the remaining terms in the energy:

- the exchange energy arising from the antisymmetry of the quantum mechanical wave function;

- dynamic correlation in the motions of the individual electrons.

Hohenberg and Kohn demonstrated that E^{XC} is determined entirely by (is a functional of) the electron density. In practice, E^{XC} is usually approximated as an integral involving the spin densities and possibly their gradients:

$$E^{XC}(\rho) = \int f(\rho_\alpha(\vec{r}), \rho_\beta(\vec{r}), \nabla\rho_\alpha(\vec{r}), \nabla\rho_\beta(\vec{r})) d^3\vec{r} \quad (3-23)$$

where ρ_α refers to the α spin density, ρ_β refers to the β spin density, and ρ refers to the total electron density ($\rho_\alpha + \rho_\beta$).

E^{XC} is usually divided into separate parts, referred to as the exchange and correlation parts, but actually corresponding to same-spin and mixed-spin interactions, respectively:

$$E^{XC}(\rho) = E^X(\rho) + E^C(\rho) \quad (3-24)$$

All three terms are again functionals of the electron density, and functionals defining the two components on the right side of equation (3-24) are termed *exchange functionals* and *correlation functionals*, respectively. Both components can be of two distinct types: *local* functionals depend on only the electron density ρ , while *gradient-corrected* functionals depend on both ρ and its gradient, $\nabla\rho$ [112].

The *local exchange* functional is virtually always defined as follows:

$$E_{LDA}^X = -\frac{3}{2} \left(\frac{3}{4\pi} \right)^{1/3} \int \rho^{4/3} d^3r \quad (3-25)$$

Becke formulated the following *gradient-corrected exchange* functional based on the Local Density Approximation (LDA) exchange functional, which is now in wide use [113,114]:

$$E_{Becke88}^X = E_{LDA}^X - \gamma \int \frac{\rho^{4/3} x^2}{(1 + 6\gamma \sinh^{-1} x)} d^3r \quad (3-26)$$

where $x = \rho^{-4/3} |\nabla\rho|$; γ is a parameter chosen to fit the known exchange energies of the inert gas atoms, and Becke defines its value as 0.0042 Hartrees.

Pure DFT methods are defined by pairing an exchange functional with a correlation functional. For example, the well-known BLYP functional pairs Becke's gradient-corrected exchange functional with the gradient-corrected correlation functional of Lee, Yang and Parr (LYP) [115].

Another class of functionals are the so called *hybrid functionals*, conceptually defining E^{XC} as:

$$E_{hybrid}^{XC} = c_{HF} E_{HF}^X + c_{DFT} E_{DFT}^{XC} \quad (3-27)$$

where the c 's are constants. The best known of these hybrid functionals is Becke's three-parameter formulation, defined *via* the following expression:

$$E_{B3LYP}^{XC} = E_{LDA}^X + c_0 (E_{HF}^X - E_{LDA}^X) + c_X \Delta E_{B88}^X + E_{VWN3}^C + c_C (E_{LYP}^C - E_{VWN3}^C) \quad (3-28)$$

Here, the parameter c_0 allows any admixture of Hartree-Fock (HF) and LDA local exchange to be used. In addition, Becke's gradient correction to LDA exchange is also included, scaled by the parameter c_X . Similarly, the Vosko, Wilk and Nusair local correlation functional is used [116], and it may be optionally corrected by the LYP correlation correction *via* the parameter c_C .

Different functionals can be constructed in the same way by varying the component functionals—for example, by substituting the Perdew-Wang 1991 gradient-corrected correlation functional for LYP and by adjusting the values of the three parameters [117]. Among other DFT methods the hybrid functionals show the most satisfactory performance, sometimes with errors against the G2 set of only slightly above 8.3 kJ mol⁻¹ [118].

Gaussian includes many different quantum chemistry models. They are characterized by the combination of theoretical procedures and basis sets. The *Gaussian* program contains a hierarchy of procedures corresponding to different approximation methods (commonly referred to as different level of theory): HF, B3LYP, MP2, MP4, etc.

A *basis set* is a mathematical representation of the molecular orbitals within a molecule. The basis set can be interpreted as restricting each electron to a particular region of space. Larger basis sets impose fewer constraints on electrons and more accurately approximate exact molecular orbitals [112]. They require correspondingly more computational resources.

Although not strictly part of a quantum chemistry model, there is a third component to every *Gaussian* calculation involving how electron spin is handled: whether it is performed using an open shell model or a closed shell model; the two options are also referred to as unrestricted and restricted calculations, respectively. Restricted, closed shell calculations force each electron pair into a single spatial orbital, while open shell calculations use separate spatial orbitals for the spin up and spin down electrons (α and β respectively) [112].

Gaussian 98 (03) is capable of predicting many properties of molecules and reactions, in the gas phase and in solution, including the following:

- molecular energies and structures;
- bond and reaction energies, molecular orbitals;
- atomic charges, electrostatic potentials and electron densities;
- vibrational frequencies and thermochemical properties;
- ESR and NMR properties, etc.

Computations can be carried out in their ground state or in an excited state. The energies, structures and molecular orbitals can be predicted also for periodic systems. Thus, Gaussian can serve as a powerful tool for exploring areas of chemical interest like substituent effects, reaction mechanisms, potential energy surfaces, and excitation energies [119,120].

3.4 Non-fluorinated monomeric building blocks

3.4.1 Preparation of solutions

The oxidative and photochemical stability of 4,4'-sulfonyldiphenol (SDP), bisphenol A (BPA), 4,4'-diphenol (DP), sulfonated 4,4'-dichlorodiphenylsulfone (sDCPS), 4,4'-dihydroxybenzophenone (HBP), sPEK, sPEEK and sPEKEK was investigated in water (or

water-methanol mixtures) in the pH range 0.4-13.9 (Fig. 9). Direct photolysis of aqueous solutions of H_2O_2 was chosen as the source of HO^\bullet radicals as described in Chapter 2. Doubly distilled water was used and the pH was adjusted with H_2SO_4 or KOH , using a digital WTW pH-meter (Modell pH 330) calibrated with commercial buffer solutions. Before irradiation solutions were deoxygenated by bubbling with nitrogen for 15 minutes.

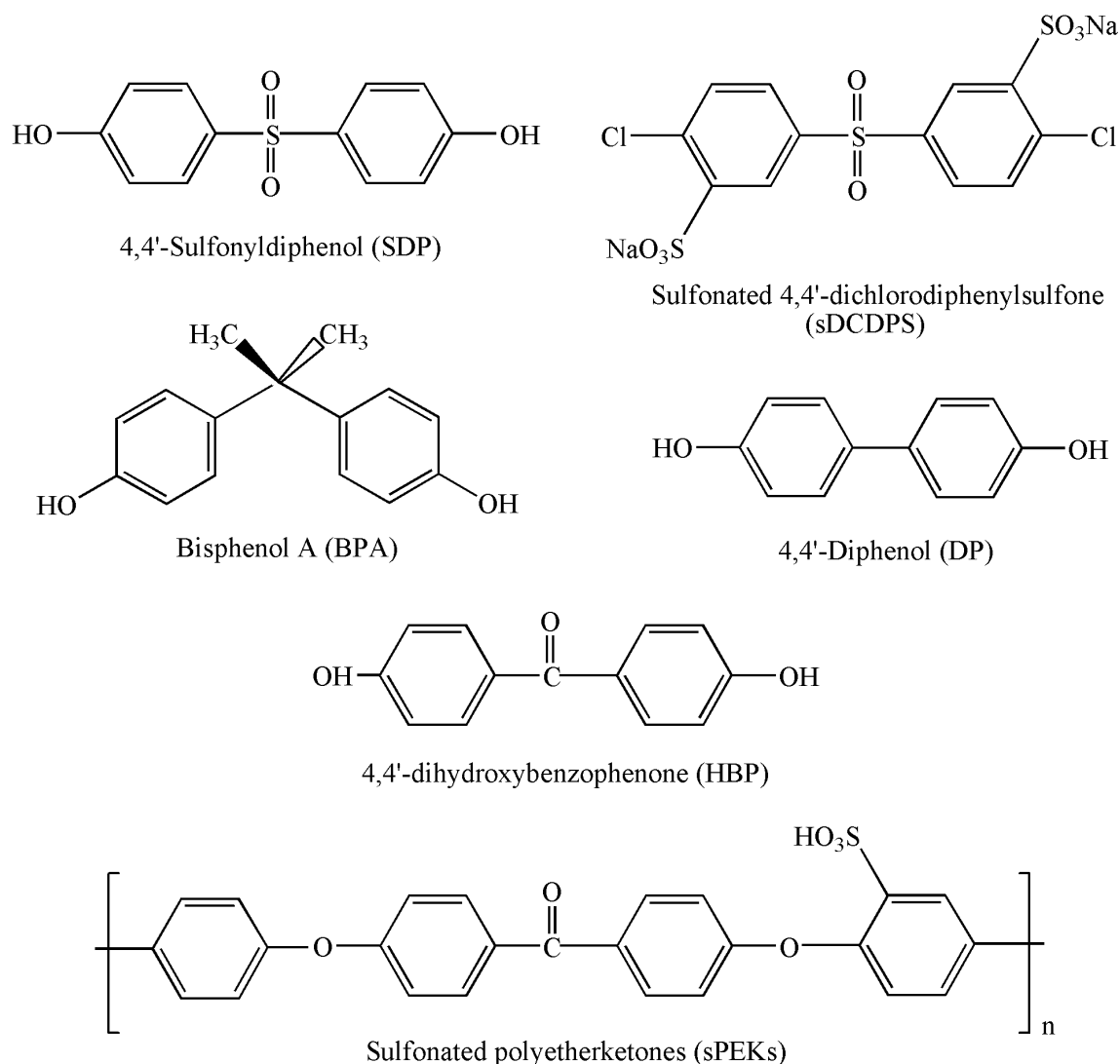


Fig. 9: Model compounds for the investigation of HO^\bullet initiated degradation reactions.

H_2O_2 (30% solution) was obtained from Merck[®], the SDP, BPA, DP and HBP monomers from Aldrich[®]. The sDCPS monomer and the sPEK, sPEEK and sPEKEK polymers were synthesized in the group of Dr. Kerres at the Institute for Chemical Engineering, Stuttgart University. In the case of non-water soluble monomers a 1:1 (v/v) water-methanol solution

was used. The concentration of H_2O_2 was fixed to 40 mmol l^{-1} in accordance with earlier investigations [57] and the optimal concentration of the monomeric building blocks for the ESR measurements proved to be 4 mmol l^{-1} , unless otherwise stated, based on their extinction coefficients. The DBNBS spin trap was purchased from Aldrich[®] and the applied concentration was 10 mmol l^{-1} . The applied concentrations for sPEK, sPEEK and sPEKEK polymers were 1.0, 1.5 and 2.3 g l^{-1} , respectively. Experiments were carried out with and without the addition of H_2O_2 to the solutions of the non-fluorinated monomers and polymers.

3.4.2 Apparatus and analysis of ESR spectra

ESR spectra were recorded with a Varian E-Line X-band spectrometer. Microwave power was held at 2.5 mW unless otherwise stated. Aqueous solutions of the monomer (polymer) and H_2O_2 were photolyzed in a flat quartz flow cell ($0.4 \text{ mm} \times 10 \text{ mm} \times 50 \text{ mm}$) at ambient temperature within the resonator. A 500 W Hg (Xe) high pressure mercury arc lamp (Oriental 66142) was used as an irradiation source. Wavelengths below 210 and above 400 nm were eliminated with a filter solution ($1.14 \text{ mol l}^{-1} \text{ NiSO}_4 / 0.21 \text{ mol l}^{-1} \text{ CoSO}_4 / 0.01 \text{ mol l}^{-1} \text{ H}_2\text{SO}_4$). A constant flow ($8\text{-}135 \text{ ml h}^{-1}$) of the solutions through the cell was maintained by a syringe pump. By changing the flow the residence time within the cavity was varied between 5 and 90 seconds, so that successive reaction products could be separately focused on. UV-VIS spectra were measured by a Perkin Elmer Lambda 2 UV/VIS spectrometer.

g-Values were calculated relative to the Bruker[®] weak pitch sample ($g=2.0028$). They are accurate to ± 0.0002 units. Second order effects are within this range of errors for the comparatively small coupling constants observed in our systems, and were neglected. The obtained digital spectra were analyzed using Microcal Origin[®], Version 5.0. Hyperfine splittings were derived from computer simulations using the WINEPR Simphonia program and assigned by comparison with literature values of similar radical systems [121].

3.5 E-beam irradiated fluoropolymer films

3.5.1 Preparation of irradiated fluoropolymer samples

The base polymers PVDF and ETFE were purchased in the form of $50 \text{ }\mu\text{m}$ and $100 \text{ }\mu\text{m}$ thick films, respectively, from Nowofol GmbH (Siegsdorf, Germany). The base polymer FEP

was purchased in the form of a 75 μm thick film from DuPont, Circleville, OH, USA. The molar weights and copolymer composition of the resins used to make these films have been reported previously [87]. The FEP films are about 17% crystalline, and the partially fluorinated ETFE and PVDF films are about 30% and 41% crystalline [87].

Three small stripes (approximately 1.5 mm \times 30 mm each) of the fluoropolymer films were cut in the machine direction of each film roll, washed with ethanol, dried and placed in quartz ESR measurement tubes with the machine direction aligned in the direction of the tube. Some sample tubes were melt-sealed at 500 mbar air atmosphere and others under inert atmosphere. The samples sealed under inert atmosphere were first placed under a vacuum of 1×10^{-5} mbar for 4 h at 70 $^{\circ}\text{C}$, intermittently purged with argon, and finally sealed under a 500 mbar argon atmosphere. For irradiation the film was placed in the upper end of the sample tube while the lower end was shielded in steel to avoid any large-scale interference of radiation defects in quartz during ESR experiments. Samples were irradiated using electron beam irradiation, and the dose was 40 kGy unless otherwise noted. The irradiation was performed nominally at room temperature at Studer AG in Däniken, Switzerland. Irradiated samples were stored at -70 $^{\circ}\text{C}$ until they were analyzed.

3.5.2 In-situ ESR measurements during grafting reactions

The grafting reactions were carried out using a specially constructed quartz cell (Fig. 10) in a somewhat similar manner as in the work of Tabata and Fujikawa [122]. This cell has a breakable seal so that the styrene monomer could be added to the quartz tube containing the irradiated film sample without any introduction of oxygen to the inert atmosphere. For the grafting reaction the *tert*-butylcatechol radical inhibitor was removed from the styrene (Fluka purum grade) by means of distillation. The styrene was then deoxygenated by carrying out three freeze-pump-thaw cycles while under vacuum. After attaching the quartz tube containing the irradiated film sample to the vacuum line along with the round-bottomed flask containing the purified styrene monomer (or styrene dissolved in ethanol or benzene), any gaseous products resulting from the film irradiation were first removed by vacuum from the cell. Then valve 1 (Fig. 10) was closed and the styrene transferred from the round-bottomed flask to the quartz tube containing the polymer film. An excess of styrene for the grafting reaction was used (approximate mass ratio of 5:1 for styrene:film). Then valve 2 was closed, and the quartz tube was melt-sealed under inert atmosphere. The part of the quartz tube containing monomer and film was kept cooled in liquid nitrogen throughout this sealing

process. The monomer was then quickly thawed, and the tube was finally placed in the preheated ESR resonance chamber ($t = 0$) at $+60\text{ }^{\circ}\text{C}$.

In-situ ESR spectra were subsequently measured approximately every 3 minutes during grafting and until only the residual ESR signal of the irradiated quartz remained detectable. In our experiments the role of temperature and irradiation atmosphere, as well as the role of diluent for the grafting reactions of FEP, ETFE and PVDF polymer films were investigated. The ESR experiments were carried out on a Bruker X-band spectrometer. All spectra were accumulated using a microwave power of 2.5 mW.

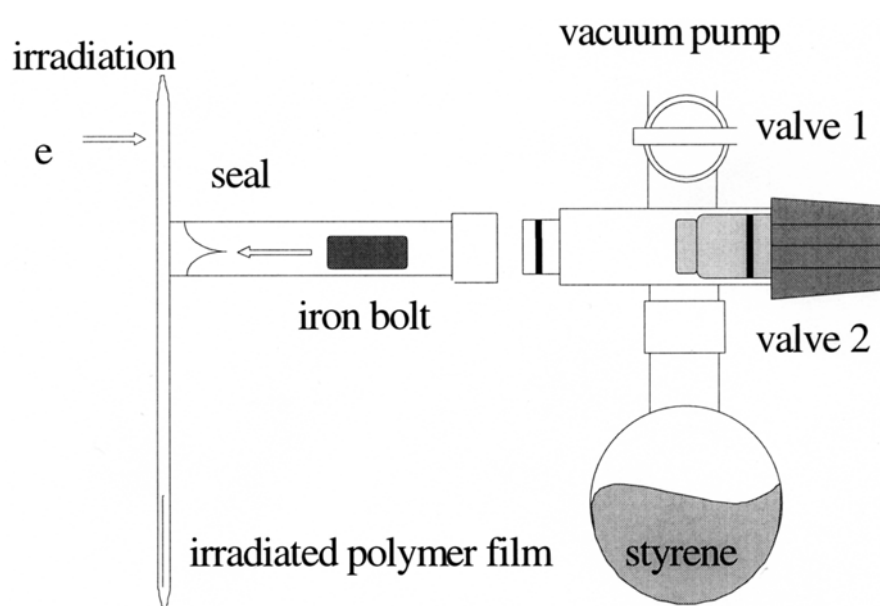


Fig. 10: Quartz cell for *in-situ* ESR experiments during grafting of irradiated polymer films [122].

3.5.3 Analysis of decay curves and grafting levels

Absolute spin concentrations were determined by double integration of the ESR signal and calibrated against a Bruker[®] standard sample. Experimental uncertainties lead to a systematic error of 25% [90]. Based on Gaussian error propagation absolute spin concentration values have a total error of 50% ($\pm 25\%$).

In the most general case the radical decay curves during grafting were analyzed according to the equation:

$$y = y_0 + A_1 \exp(-k_1 t) + A_2 \exp(-k_2 t), \quad (3-29)$$

where y_0 represents a constant offset that is related to a crystalline fraction that is not soluble in the grafting mixture, and A_1 and A_2 are given as normalized fractions ($y_0 + A_1 + A_2 = 1$) which react away with pseudo-first order rate constants k_i . The decay of alkyl radicals is monitored by the change of the double integral of the spectra, that of peroxy radicals by the change of the first integral of the positive part of the line, because of the overlap with the alkyl radical in the negative range of these spectra.

The grafted films obtained at the end of the reaction, as judged from the disappearance of any ESR signals, were Soxhlet extracted for 8 hours with toluene and dried for 4 hours under vacuum at +50 °C. The grafting levels of the films were determined from the mass of the starting films, m_i , and of their corresponding extracted and dried, grafted film, m_g , as shown in the following equation:

$$\text{grafting level} = \frac{m_g - m_i}{m_i} 100\% \quad (3-30)$$

From the grafted mass and the initial number of radical centers (spins) the average number of monomer units per grafted chain is estimated, assuming here that each radical initiates one chain.

3.6 DFT calculations for non-fluorinated and perfluorinated fragments

Thermodynamic properties of small alkyl and alkyl-peroxy radicals are studied to model primary, secondary and tertiary radicals in non-fluorinated and perfluorinated polymers. Bond strengths, bond lengths, and total atomic charges from the Mulliken population analysis for the alkyl and alkyl-peroxy radicals are calculated using the B3LYP DFT method with spin-restricted orbitals. A 6-311+G** basic set as implemented in Gaussian 98 was employed [119]. The symbol ** shows that a polarized basis set is used, e.g. p functions are added to hydrogen atoms in addition to the d functions on heavy atoms. The symbol + shows that diffuse functions are added to the heavy atoms as well. They allow orbitals to occupy a larger region of space. Bond dissociation energies (BDEs) were calculated as the difference between the computed total energies (including thermal corrections to enthalpy at 298 K and zero-point energies) of the products and those of the reactants.

Furthermore, energy barriers to internal rotation and hyperfine couplings for the optimized and forced planar structures of end-chain alkyl radicals were calculated using the Gaussian 03 package [120]. The initial geometries of the fragments and the energies were obtained in gas

phase DFT calculations using the UB3LYP hybrid functional and a 6-311+G** basis set. The defined dihedral angle θ is between the axis of the $2p_z$ or hybrid orbital hosting the unpaired electron at the C^α atom and the plane containing the C^α , C^β and F^β (H^β) atoms. In some separate calculations the C^α , C^β and the two F^α (H^α) atoms were constrained to the same plane to enforce planarity at the radical centre. Hyperfine coupling constants were obtained from single point calculations using the UB3LYP/EPR-II option. EPR-II is a double zeta basis set with a single set of polarization functions and an enhanced s part [123]. For the g -tensors the MAG program from the University of Würzburg was used [124].

The two-fold rotation symmetry with 180° periodicity in equation (3-11) has its origin in the hyperconjugative overlap of the C–X bond with the unpaired electron density in the half-filled p_z orbital at the radical centre which scales as $\cos^2\theta$. For increasing non-planarity at the radical centre the half-filled orbital adopts more and more s -character, resulting in sp^3 character for tetrahedral symmetry. In representations of the rotational dependence of the β -hyperfine coupling non-planarity can be accounted for by adding a one-fold term to equation (3-11). ρ_π is no longer defined so that the new coefficients are just phenomenological. Furthermore, in the present theoretical work we have not performed any Boltzmann and vibrational averaging. We report the accurate calculated angular dependence at zero absolute temperature and omit therefore the symbols for the expectation values:

$$a^\beta = a_0^\beta + b^\beta \cos^2(\theta - \theta_0) + c^\beta \cos(\theta - \theta_0) \quad (3-31)$$

Also related to symmetry but based on a somewhat different origin is the potential to internal rotation. $V(\theta)$ is in general given by a sum of periodic terms:

$$V(\theta) = V_0 + \frac{V_1}{2} \cos(\theta - \theta_1^0) + \frac{V_6}{2} \cos(6\theta - \theta_6^0) \quad (3-32)$$

V_0 provides a constant offset. As a consequence of the C_3 symmetry of the methyl group and the C_2 symmetry at the radical centre V_6 is the only other non-zero term for $\text{CH}_3^\bullet\text{CH}_2$, whereas V_1 comes in for non-planar radicals. $V(\theta)$ determines the wave function for the internal rotational motion which is responsible for $\langle a^\beta \rangle$.

The dipolar contribution to the electron-nuclear hyperfine interactions scales as $\langle (3\cos^2\theta - 1)/r^3 \rangle$. The expectation value is calculated as the integral over the orbital containing the unpaired electron. The angular dependence defines a double cone with an opening angle that is twice the magic angle, i.e. 109.4° . The orientation of the double cone (centered at the nucleus) that can accommodate the largest fraction of the electron spin density distribution in the section around the symmetry axis of the cone defines the positive axis of the anisotropy

tensor. Spin polarization creates a significant amount of negative spin density at other atoms and can therefore complicate the situation.

Chapter 4

4 OXIDATIVE AND PHOTOCHEMICAL STABILITY OF NON-FLUORINATED IONOMERS

4.1 ESR results and specific discussion

4.1.1 4,4'-Sulfonyldiphenol (SDP)

SDP is a monomeric building block of the sulfonated PSU. The only species that was detected both in the presence and the absence of H_2O_2 is the multiplet of radical **1** with five equidistant ESR lines with relative intensities corresponding to four equivalent protons. Based on its g -value (2.0049) and its proton hyperfine coupling constant there is little doubt that it corresponds to the p -semiquinone radical anion (Fig. 11, Table 4).

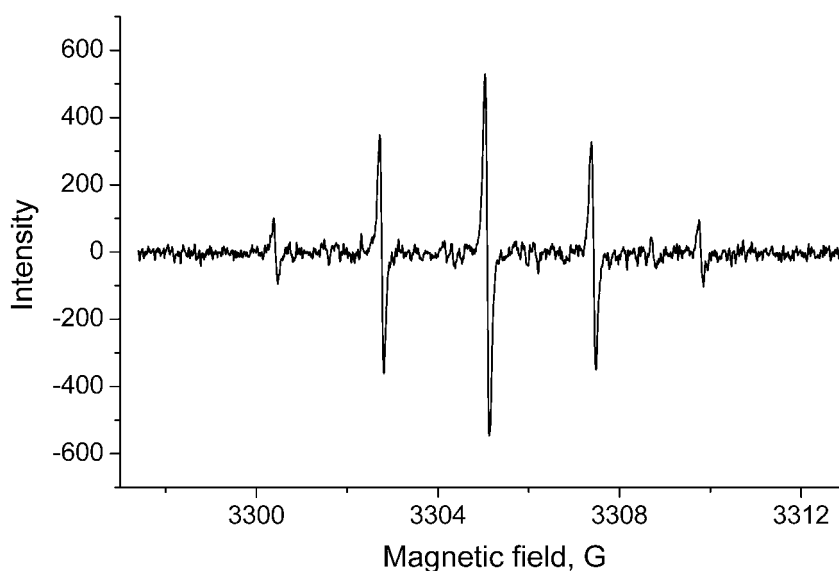


Fig. 11: Experimental ESR spectrum of the p -benzosemiquinone radical anion **1** obtained with SDP at pH 12.2 and 135 ml h^{-1} flow rate.

SDP has a high molar extinction coefficient ($\epsilon_{296} = 20600 \text{ L mol}^{-1}\text{cm}^{-1}$ at pH 12.2 and $\epsilon_{260} = 17600 \text{ L mol}^{-1}\text{cm}^{-1}$ at pH 7.2) so that also in the presence of H_2O_2 , the dominant fraction of

the light is absorbed directly by the monomer and leads to its cleavage. The signal amplitude increases by a factor of five between the flow rates 8 and 135 ml h⁻¹. At lower flow rates no signals were detected, indicating that the radical is short lived or the monomer gets depleted.

In the presence of H₂O₂, ESR signals were observed in the range between pH 7.6 and pH 13.9 (Fig. 12), with a maximum at pH 12.2, near the pK_S of the HO• radicals (11.9) and the pK_S of H₂O₂ (11.7). No signals were observed under acidic or neutral conditions.

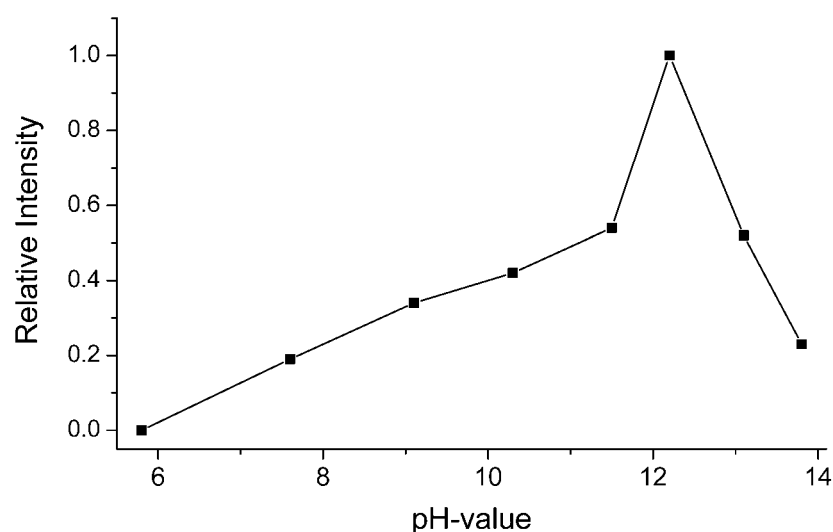


Fig. 12: Relative intensities of the ESR signals of radical **1** observed with SDP at 135 ml h⁻¹ flow rate in dependence on the pH-value.

Spin trap experiments with DNBNS were performed at acidic conditions aiming at the identification of possible radicals. The applied spin trap concentration was fixed at 10 mM, all other experimental conditions were identical with the previous measurements. As seen from Fig. 13, the observed signals at pH 0.4 consists of a 1:1:1 triplet (due to $a_N = 13.54$ G) of a 1:2:1 triplet (due to two equivalent protons with $a_H = 8.95$ G). This spectrum clearly arises from the •CH₂OH radical adduct to DNBNS and not from SDP. The hydroxyl radicals react first with methanol, which is to be expected as the initial methanol concentration (12 M) is a factor of 3000 higher than that of SDP (4 mM). In view of the high reaction rate of HO• radicals with methanol (see Table 3) it is clear that in the presence of solvents other than water one should not expect to see products of HO• reactions with a substrate that is present only in millimolar concentrations. Water-soluble monomers are therefore more suitable for experiments involving hydroxyl radicals under acidic conditions. Furthermore, at the higher

flow rate (Fig. 13b) a small triplet splitting is observed that is due to the H_{meta} of the spin trap molecule DNBBS ($a_{\text{H}} = 1.02$ G).

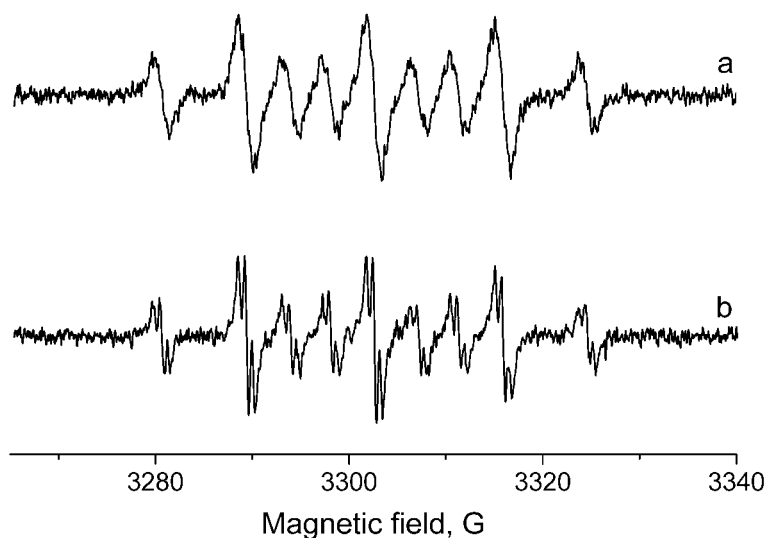


Fig. 13: ESR spectrum of an SDP/DNBBS/water/methanol/ H_2O_2 mixture at pH 0.4 and at a) flow rate of 8 ml h^{-1} ; b) flow rate of 90 ml h^{-1} .

4.1.2 Bisphenol A (BPA)

BPA (also termed 4,4'-isopropylidendiphenol) is a monomeric building block of the sulfonated PSU, which together with PEK is an alternative for the replacement of the most widely used but expensive perfluorinated Nafion[®]. PSU is usually sulfonated by electrophilic substitution at the position *ortho* to the ether bridge of the BPA fragment, because this part of the molecule has a high electron density (+ M effect from the ether bridge, + I effect from the isopropylidene group), in contrast to the diarylsulfone portion of the monomer repeating unit which has a low electron density due to the electron-withdrawing SO_2 group (- I , - M effect).

In the absence of H_2O_2 the same multiplet spectrum that was found with SDP and assigned to the *p*-semiquinone radical anion is observed. This multiplet is superimposed by further lines at lower intensity which appear more strongly in the presence of H_2O_2 . BPA has a lower absorption coefficient at λ_{max} ($\epsilon_{293} = 4000 \text{ L mol}^{-1}\text{cm}^{-1}$ at pH 12.0) than SDP but absorbs strongly at shorter wavelength ($\epsilon_{242} = 16960 \text{ L mol}^{-1}\text{cm}^{-1}$).

In the presence of H_2O_2 the spectrum at pH 12 and flow rate 135 ml h^{-1} is quite different (Fig. 14). H_2O_2 or its anions are obviously photolyzed, most likely at wavelengths near 267 nm where there is a window between the above absorption bands. The spectrum is nearly symmetric and consists of two groups of lines, which based on their intensities and their variation with experimental conditions cannot be assigned to a single radical. From simulations and comparison of the coupling constants with literature values [121] it was concluded that the observed spectrum consists of a superposition of the four different radical species **1-4** with almost identical g -values (Table 4). Due to the mesomerism, the largest coupling constants are in the *ortho*- and *para*-positions relative to the phenoxy radical centre.

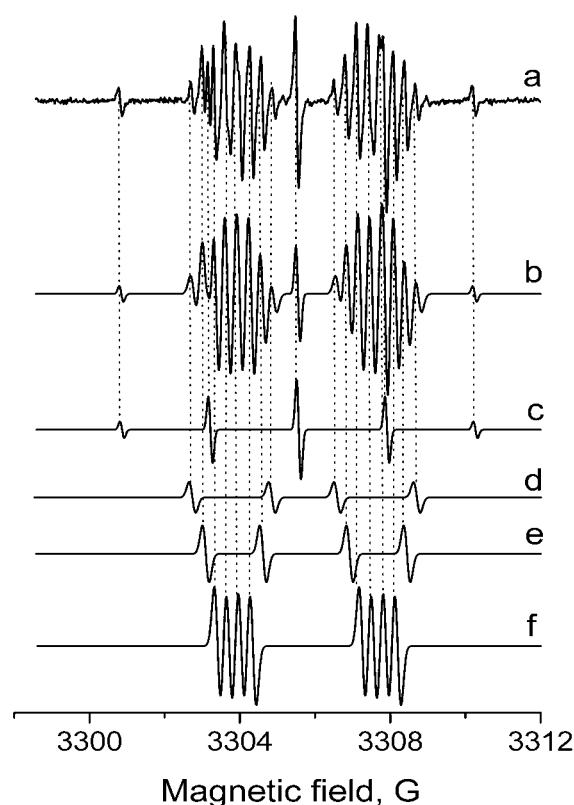


Fig. 14: a) Experimental ESR spectrum obtained with BPA at pH=12 and 135 ml h^{-1} flow rate; b) simulation for the sum of radicals **1-4**; c) simulation of radical **1** (33%); d) simulation of radical **2** (5%); e) simulation of radical **3** (14%); f) simulation of radical **4** (48%). Measurement and interpretation by O. Delmer [69].

Table 4: ESR parameters of intermediates in the reaction of HO• radicals with sulfonated aromatics. Hyperfine splittings were derived from computer simulations using the WINEPR Simphonia program and assigned by comparison with literature values of similar radical systems [121]. Due to the similarity of all parameters the structural assignments are somewhat tentative.

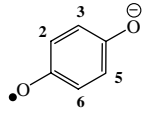
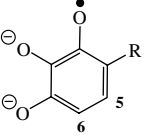
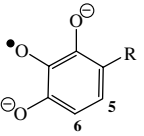
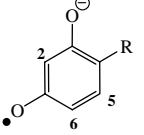
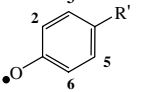
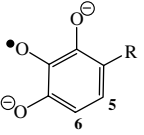
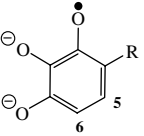
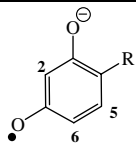
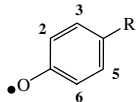
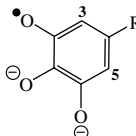
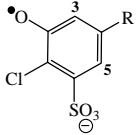
Substrate and Conditions	Hyperfine splittings, G	<i>g</i>	Nr.	Structure
SDP pH=12.2, 135 ml h ⁻¹	4 H (2,3,5,6): 2.35	2.0049	1	
BPA pH=12.0, 135 ml h ⁻¹	4 H (2,3,5,6): 2.35	2.0049	1	see above
	1 H (5): 3.85 1 H (6): 2.12	2.0048	2	 R = C(CH ₃) ₂ C ₆ H ₄ OH
	1 H (5): 1.52 1 H (6): 3.83	2.0048	3	
	1 H (2): 0.64 1 H (5): 0.31 1 H (6): 3.85	2.0048	4	
DP pH=12.2 (10.3), 135 ml h ⁻¹ no H ₂ O ₂	4 H (2,6,2',6'): 1.84 4 H (3,5,3',5'): 0.92	2.0047	5	 R' = C ₆ H ₄ O ⁻
DP pH=10.3, 135 ml h ⁻¹ with H ₂ O ₂	1H (5): 1.22 1H (6): 3.24	2.0044	6	 R = C ₆ H ₄ OH
	1 H (5): 3.25 1 H (6): 1.72	2.0044	7	

Table 4 (continued)

Substrate and Conditions	Hyperfine splittings, G	g	Nr.	Structure
DP pH=10.3, 135 ml h ⁻¹ with H ₂ O ₂	1 H (2): 0.50 1 H (5): 0.24 1 H (6): 3.23	2.0044	8	 R = C ₆ H ₄ OH
	1 H (2,6): 3.13 1 H (3,5): 0.26	2.0044	9	
	1 H (3): 0.26 1 H (5): 0.74	2.0044	10	
sDCPS pH=12.2, 13 ml h ⁻¹	1 H (3): 1.90 1 H (5): 3.60	2.0047	11	 R = SO ₂ C ₆ H ₃ SO ₃ NaCl

BPA is a symmetric compound; therefore only one aromatic ring will be taken into consideration. No coupling through the C(CH₃)₂ group is observed (Table 4). Radical **1** is the same *p*-semiquinone radical anion as observed in the absence of H₂O₂. It arises from the fraction of light that is absorbed directly by the monomer. For the other species the number of doublet splittings in the spectrum shows that there are only two H-atoms for radicals **2** and **3**, and three for radical **4**. The lack of H-couplings within aromatic rings suggests that secondary reactions like further hydroxylation or dimerization of the monophenoxy radicals occur. The latter can be excluded at higher flow rates, because of the absence of the expected additional splittings from the H-atoms in the neighboring ring. At lower flow rates the spectra are different (Fig. 15), but in contrast to Fig. 13 where additional structure appears at the higher flow rate we have more and narrower lines at low flow rate. This points to an explanation involving primary radicals predominantly at high flow rates and secondary ones at lower rates with corresponding extended residence time in the ESR active zone of the cell. Due to dimerization, additional smaller coupling constants appear. Coupling of phenoxy radicals forming either phenoxy-, phenol- or biphenyl-like radicals has previously been described [125,126], but the possible formation of consecutive new monomeric species should nevertheless not be excluded.

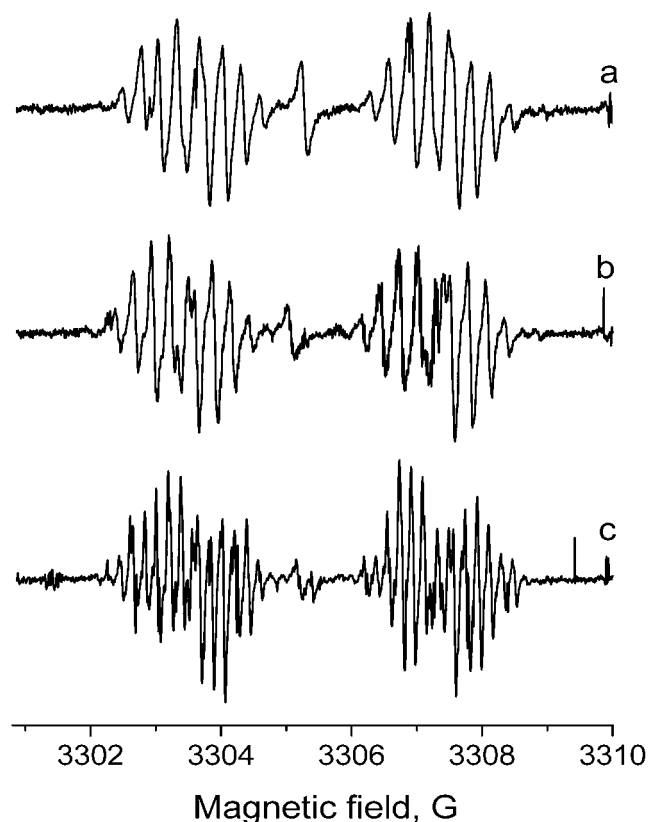


Fig. 15: ESR spectra obtained with BPA at pH 12 and different flow rates: a) 90 ml h⁻¹; b) 20 ml h⁻¹; c) 8 ml h⁻¹.

An additional contribution to the formation of higher-substituted products may be due to the increased absorption coefficients of H₂O₂ solutions under alkaline conditions (pH 0.45: $\epsilon_{230} = 42 \text{ L mol}^{-1} \text{ cm}^{-1}$ for H₂O₂, pH 12.6: $\epsilon_{230} = 317 \text{ L mol}^{-1} \text{ cm}^{-1}$ for HOO⁻). The signal amplitudes arising from the four observed radicals depend only slightly on the flow rates (not shown) and do not permit a clear conclusion as regards radical formation mechanism. For the determination of the relative intensities a clear ESR line, not overlapping with other signals, was chosen for each individual radical. Its intensity ($1/2 \times \Delta H$ (line width) \times signal intensity) was used to determine the cumulative intensity of all lines of the individual radical.

It is clearly seen that all four radical species exist in a specific pH range between pH 9 and pH 14 (Fig. 16). The relative concentrations of the four radicals remain the same, and a maximum of the absolute intensity is adopted at pH 11.8. This behaviour will be discussed in subchapter 4.2.

Experiments with DNBNS spin trap at pH 0.4 and a flow rate of 90 ml h^{-1} led to the same spectrum (not shown) as observed with SDP, arising from the $\cdot\text{CH}_2\text{OH}$ radical. At the given concentration BPA cannot successfully compete for $\text{HO}\cdot$ with the methanol solvent. Nevertheless, a change of color of the solution demonstrates that photochemical reactions do occur.

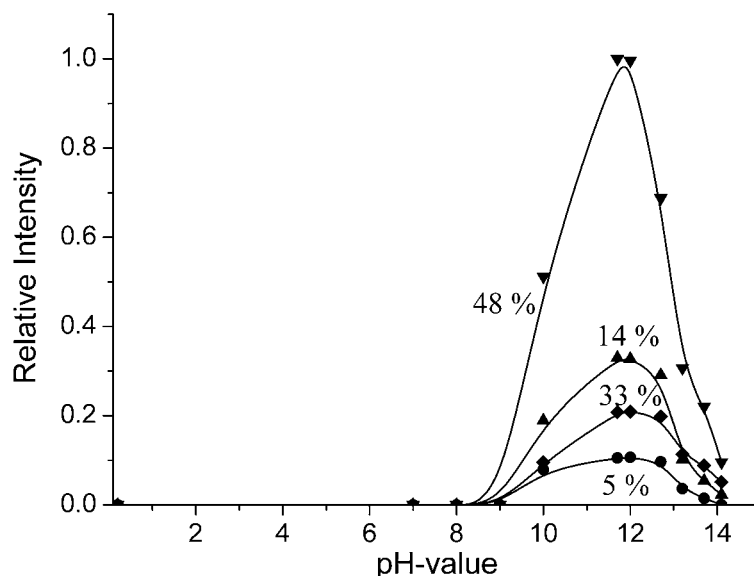


Fig. 16: Relative intensities of the ESR signals of the radicals **1** (\blacklozenge), **2** (\bullet), **3** (\blacktriangle) and **4** (\blacktriangledown) observed with BPA at 90 ml h^{-1} flow rate in dependence on the pH-value.

4.1.3 4,4'-Diphenol (DP)

DP has a strong absorption band at 286 nm ($\epsilon_{286} = 32400 \text{ L mol}^{-1} \text{ cm}^{-1}$ at pH 11.7) which shifts to 262 nm and somewhat lower absorption at pH 10.35. In the absence of H_2O_2 the experimental spectrum of a 2 mM solution of DP consists of a multiplet with 13 equidistant lines (Fig. 17a). The intensity distribution is compatible with two sets of four equivalent protons with coupling constant which are a factor of two different (0.92 G and 1.84 G) but not with 12 equivalent protons. It is conceivable that this spectrum is due to the *p*-diphenosemiquinone anion radical **5** which may be formed by photooxidation followed by deprotonation of DP, although a somewhat different set of coupling constants (0.56 G and 2.25 G, the sum of which is nearly the same as that of the present observation) has been reported for this species in literature [127]. The spectrum is considerably weaker near pH 10 than at pH 12.2.

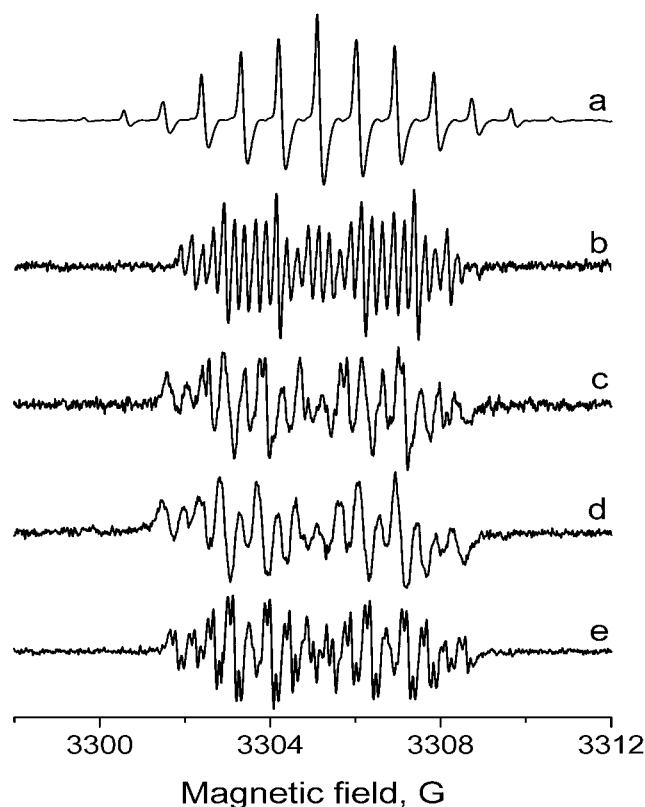


Fig. 17: ESR spectra obtained with DP acquired at 135 ml h^{-1} flow rate and: a) pH=12.2, no H_2O_2 ; b) pH 10.3; c) pH 11.3; d) pH 12.2; e) pH 13.0. Spectra (b-e) are measured in the presence of H_2O_2 .

In the presence of H_2O_2 , the 13 line spectrum of radical **5** (Fig. 17a) is absent and the observed ESR signals are strongly pH dependent (Fig. 17b-e), in a similar sense as seen before with BPA. It should be noted that there is a pronounced change in the spectra as the pH increases from 10.3 to 13.0. The well-resolved spectrum with 27 almost equidistant lines at pH 10.3 (Fig. 17b) transforms into a less well resolved 16 line spectrum at pH 12.2 (Fig. 17d). On further increase to pH 13.0 most but not all of the lines split into 0.1 G doublets. The total width and one dominant hyperfine splitting of ca. 3.2 G remain roughly constant. It is likely that the changes reflect protonation equilibria, but the details remain elusive.

Simulating the experimental ESR spectrum at pH 10.3 and flow rate 135 ml h^{-1} , and comparing the coupling constants with literature values [121] it was concluded that the observed spectrum consists of five different, simultaneously appearing radical species. The g -value is identical for all of them (2.0044) and typical for phenoxyl type radicals (Table 4, Fig. 18). Since the coupling constants are small these assignments are not unique. The fractions which are determined by matching the intensities in the simulation are 26% for radical **6**, 14%

for radical **7**, 35% for radical **8**, 17% for radical **9** and 8% for radical **10** (Fig. 18) [35]. The number of doublet splittings shows that there are only two H-atoms for radicals **6**, **7** and **10**, and three for radical **8**. The lack of H-couplings within aromatic rings suggests that secondary reactions like further hydroxylation of the monophenoxy radicals occur. Only radical **9** possesses four H-atoms, but two pairs of them are equivalent, leading to the triplet of triplet observed in our spectrum. It is remarkable that the observed phenoxy radicals appear in the pH range close to the pK_s of the HO^\bullet radical (11.9) and of H_2O_2 (11.7).

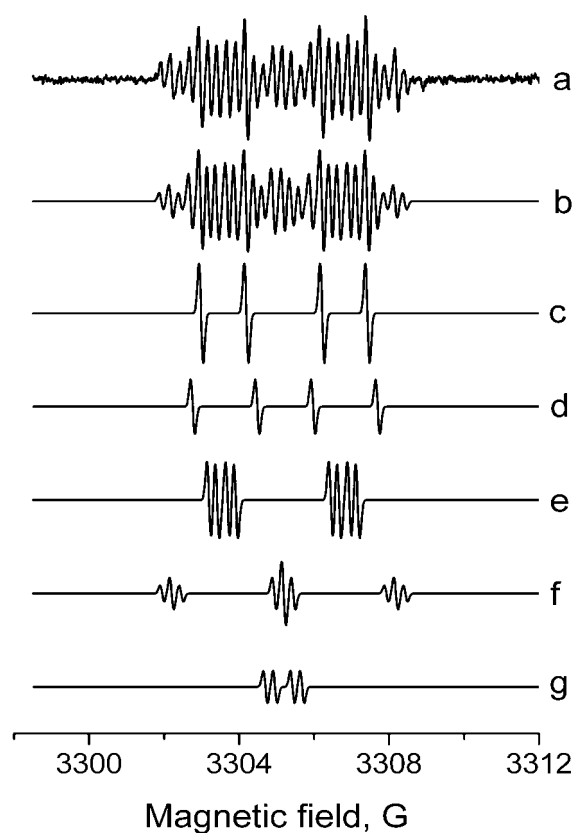


Fig. 18: a) Experimental spectrum obtained with DP at pH=10.3 and 135 ml h^{-1} flow rate; b) simulation for the sum of radicals **6-10**; c) simulation radical **6**; d) simulation radical **7**; e) simulation radical **8**; f) simulation radical **9**; g) simulation radical **10**.

Formation mechanisms for such radicals were proposed previously [47] and at $\text{pH} > 10$ all radicals derive from the deprotonated form of DP. The ability of $^1\text{O}_2$ to add directly to aromatic rings may be the reason for the formation of phenoxy radicals such as **6**, **7**, and **10**. Alternatively, the $\text{O}_2^{\bullet-}$ radical also shows tendencies to add directly to the aromatic rings, in

contrast to its protonated form (HOO^\bullet , $pK_S = 4.8$), and hence must be considered as an intermediate to phenoxyl radical formation (further details are given in subchapter 4.2.2).

4.1.4 Sulfonated 4,4'-Dichlorodiphenylsulfone (sDCPS)

sDCPS has a similar structure as SDP, therefore we aimed at a study comparable with SDP. Although a large number of experiments were done with sDCPS, only a few well resolved spectra were acquired. At 13 ml h^{-1} flow rate the phenoxyl radical **11** with the additional oxygen in the *ortho* position to the sulfonate substituent was identified (Fig. 19, Table 4). The spectrum measured at pH 12.2 and flow rate 20 ml h^{-1} is more complicated, as additional lines are observed, confirming the existence of dioxysubstituted species together with the phenoxyl radical **11**. A simulation of these was not possible, because of the complexity of the spectrum and the low signal-to-noise ratio. The signal marked with an asterisk is due to overlapping signals from the phenoxyl radical **11** and the $\text{SO}_3^{\bullet-}$ radical, originating from direct photolysis of sDCPS. The observed g -value (2.0030) agrees well with the g -value for the $\text{SO}_3^{\bullet-}$ radical observed in experiments with *para*-toluenesulfonic acid and identified in the reaction with the DMPO spin trap molecule [47]. Between pH 9 and pH 13 the signal arising from the $\text{SO}_3^{\bullet-}$ radical was always present in our ESR spectra.

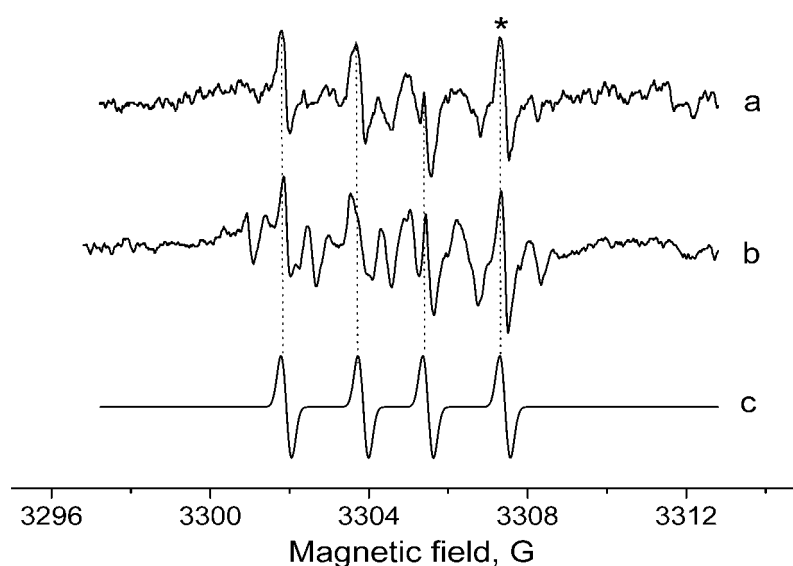


Fig. 19: Experimental ESR spectrum obtained with sDCPS at pH 12.2 and a) flow rate 13 ml h^{-1} ; b) flow rate 20 ml h^{-1} ; c) simulation of radical **11**. The asterisk denotes the $\text{SO}_3^{\bullet-}$ radical.

4.1.5 4,4-Dihydroxybenzophenone (HBP)

HBP is a monomeric building block of the sPEK. As discussed before, sPEK is an alternative for the replacement of the most widely used, but expensive perfluorinated Nafion[®]. The microwave power was held at 5 mW. The only species detected both in the presence and absence of H₂O₂ is the multiplet of radical **1**, as seen before with SDP, the only difference being that the observed line widths in the ESR spectrum of HBP were larger. HBP has a high molar extinction coefficient ($\epsilon_{240}=14800 \text{ L mol}^{-1} \text{ cm}^{-1}$ at pH 12.2 and $\epsilon_{262}=22800 \text{ L mol}^{-1} \text{ cm}^{-1}$ at pH 7.7) thus the dominant fraction of the light is absorbed directly by the monomer and leads to its cleavage. Based on its *g*-value (2.0049) and its proton hyperfine coupling constant it corresponds most probably to the *p*-semiquinone radical anion. Interestingly the signals were observed only between pH=11 and pH=13. At pH < 11 only the signal from the [•]CH₂OH radical was detected. This is plausible, since the rate constant for abstraction from methanol by HO[•] is less than an order of magnitude slower than addition to aromatic rings (Table 3), but the methanol concentration is higher by a factor of 3100 than that of HBP.

4.1.6 Sulfonated Polyetherketones (sPEK, sPEEK and sPEKEK)

The water soluble polymer sPEK was measured under the same experimental conditions as its monomer HBP. The ESR lines appear in the same range as observed before for the monomers, suggesting the formation of phenoxyl radicals (Fig. 20), but in the absence of H₂O₂ weak signals were also observed. As a common feature the intensity of the signals was weak, therefore further experiments are needed in order to assign correctly the radicals. All spectra were measured at 90 ml h⁻¹ flow rate, and no signals were detected at lower flow rates. New radical species appear at pH < 11.5, but because of their low intensities it is difficult to identify them. Under acidic or neutral conditions no radicals were detected. It is expected that the dominating reaction is addition of HO[•] to the aromatic ring, preferentially in the *ortho* position to alkyl- and RO-substituents (since in sulfonated PEK the *para* position is substituted and thus blocked) [47].

sPEEK and sPEKEK were measured under the same experimental conditions as for sPEK, and under basic conditions the ESR spectra were quite similar with those obtained for sPEK (Fig. 20). No radical species were observed in experiments under acidic conditions. The fact that no radicals are observed leads to the conclusion that the lifetime of these radicals

(if formed) should be very short so that their concentration is too low, or the signals too broad or split into too many lines so that their signal is below the limit of ESR detection.

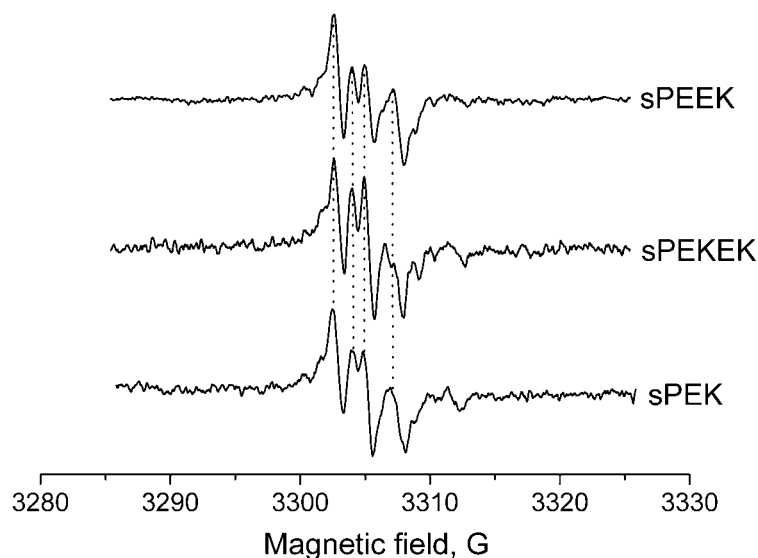


Fig. 20: Experimental ESR spectra obtained with sPEKs at pH=12.1 and 90 ml h⁻¹ flow rate.

4.2 Discussion

4.2.1 Aspects of direct photolysis

While it is clear that SDP and related sulfones are degradable by UV light, little is known about the mechanism. The formation of the *p*-benzosemiquinone radical anion establishes that the molecule is cleaved in α -position to the sulfone group, which is conceivable in analogy to the known Norrish type II cleavage of ketones under conditions where photoreduction is suppressed. It is less clear though why this does not work under acidic pH where only the spin-trap adduct of the hydroxymethyl radical is observed. These conditions may point to the involvement of HO⁻ to trap the phenyl fragment and produce the semiquinone. It is furthermore noteworthy but not so rare that the counter radical from photolysis is not observed, a fact that may be related to a short lifetime.

It is known that BPA photoionizes at 308 nm to give a bis-phenoxy radical and a solvated electron [128]. It is perhaps the shorter wavelength employed here which leads to cleavage of the carbon-carbon bond in the bridge to provide the *p*-benzosemiquinone radical. Again, the

latter is not observed under acidic pH, suggesting that an analogous mechanism as suggested for SDP is operative.

The DP does not cleave but photo-oxidizes to the *p*-dipheno-semiquinone radical anion. There can be little doubt about the nature of this species, and it is unclear why the spectrum is different from the one reported in literature [127].

4.2.2 Formation of phenoxyl and semi-quinone radicals and the origin of its pH dependence

The pH dependence shown by the HO[•] radical in reactions with substituted aromatic hydrocarbons is related to its deprotonation (pK_s 11.9) under alkaline conditions [67]. The resulting O^{•-} radical possesses only negligible tendency to add to the aromatic ring, so that at pH values exceeding the pK_s of HO[•], H-abstraction from the substituents leading to phenoxyl radicals is expected to be the predominating process.

As detailed in Subchapter 4.1.1 the presence of methanol as a solvent scavenges HO[•] efficiently so that no addition to the aromatic rings is observed.

It is remarkable that the maximum formation of phenoxyl radicals from BPA and SDP occurs in the pH range close to the pK_s of the HO[•] radicals (11.9) and of H₂O₂ (11.7). This has been shown to be due to the rates of formation of O₂^{•-} and of ¹O₂ which are proportional to the products of the rate constants and the pH dependent concentrations of the reactants [47]. H-abstraction from the deprotonated form HO₂⁻ is *ca.* 300 times faster than from H₂O₂ (see Table 2, reactions *a* and *b*) [67]. The resulting O₂^{•-} undergoes oxidation by HO[•] or O^{•-}, so that oxygen is formed *in-situ* in the reaction solutions (see Table 2, reactions *c* and *g*) [67]. Oxygen formed by this reaction has been reported to be of a singlet character [129]. This is obviously true, since ³O₂ would lead to an extensive spin exchange and thus to the loss of hyperfine structure in the ESR spectra, in contrast to our observations (see e.g. Fig. 17e). The evolution of oxygen is apparent by the bubble formation in the photolysis cell at high pH.

O₂^{•-} plays a determining role for the production of all radicals formed at high pH. Moreover, O^{•-} and O₂^{•-} are radicals with nucleophilic nature that leads to H-abstraction from phenolic OH-substituents, thus producing the primary phenoxyl radicals. O₂^{•-} can also attach directly to the aromatic ring. A suggested reaction mechanism is displayed in Fig. 21. As may be evidenced by mesomeric structures there is a higher probability that the unpaired electron is at the *ortho* or *para* position to the primary oxy group. The O₂^{•-} attacks the *ortho* position

(the *para* position is sterically hindered), and the proton is readily split off due to rearomatization under alkaline conditions. The O–O bond is broken by irradiation with UV-light and an intermediate is formed which reacts very fast *via* the same reaction pathway and cannot be detected at the used flow rate. The formation of other radicals may be rationalized by a similar mechanism.

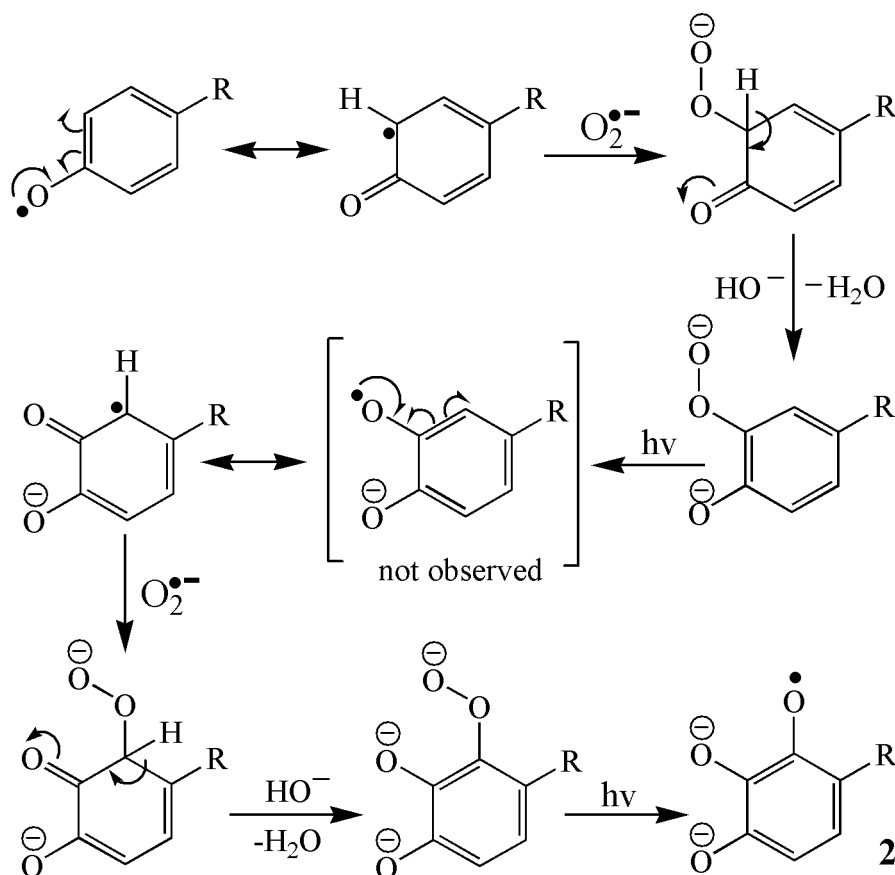


Fig. 21: Suggested formation mechanism of radical **2** ($R = C(CH_3)_2C_6H_4OH$) [130].

Alternatively, radicals may be formed by reaction with singlet oxygen. 1O_2 is known to have a pronounced tendency to undergo [2+2] and [2+4] cycloadditions to organic double bonds [131,132]. Thus, the addition of 1O_2 directly to the aromatic ring leads to the formation of the observed dioxysubstituted radicals. The $O_2^{\bullet-}$ radical forms according to reactions *a* and *f* (Table 2), and in contrast to its protonated form (HOO^{\bullet} , pK_S 4.8) it also shows tendencies to add directly to the aromatic rings and hence must be considered as an intermediate to phenoxyl radical formation (Fig. 22), as already mentioned before.

Strongly deactivating substituents such as SO_3^- and SO_2 which exert a $-I/-M$ effect direct nucleophilic substitution to the *meta* position. An oxy substituent which is strongly activating, with a $+I/+M$ effect, favors further substitution at *ortho* and *para* positions.

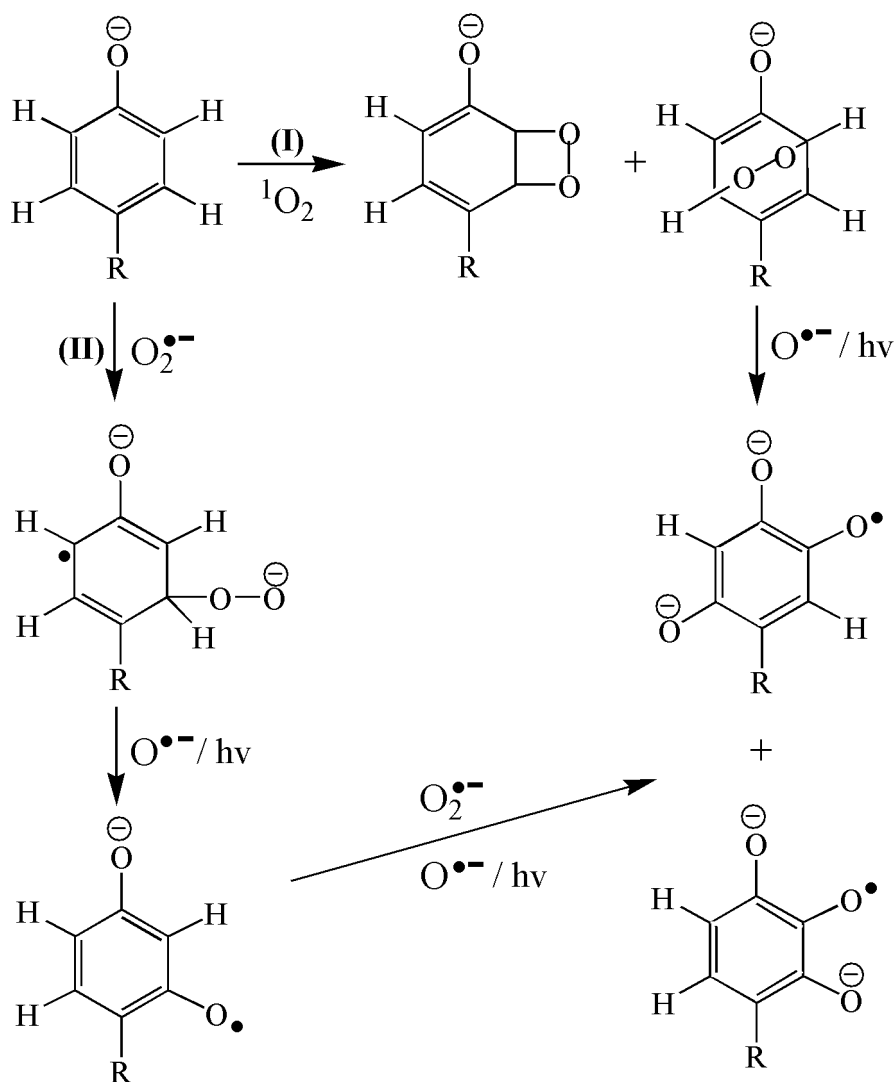


Fig. 22: Possible formation mechanism of radical **6** and further dioxysubstituted species ($R = C_6H_4OH$) [66,131,132].

4.3 Relevance for fuel cell membranes

The proton exchange membrane is a key component of the PEFC. In the current state of technology, perfluorinated membrane materials such as Nafion[®] (DuPont, USA) and Flemion[®] (Asahi Kasei, Japan) are used predominantly due to their attractive conductivity and chemical stability of the material. However, for market introduction of fuel cell products to take place, cost-competitive membrane technology has to be available.

The present work investigates monomeric membrane building blocks, under conditions which are not in every aspect those in fuel cells. However, when high currents are drawn this can give rise to significant pH inhomogeneities as a consequence of local variations in catalytic activity and in proton conductivity. Oxidative degradation of polymers is usually a free radical process which involves attack of the hydroxyl and the hydroperoxyl radicals, HO^\bullet and HOO^\bullet . Both radicals are intermediates of the oxygen reduction in a fuel cell process, and since hydrogen peroxide has been detected as a trace by-product of the fuel cell reaction it is plausibly assumed that attack of these two radicals is an important degradation pathway of the proton conducting polymer membrane. At $\text{pH} \geq \text{p}K_{\text{S}}$ of HO^\bullet and H_2O_2 , reactions between the model compounds and $\text{O}_2^{\bullet-}$ or $^1\text{O}_2$ are the most probable ways to the phenoxyl and semi-quinone radicals observed in this pH range in our ESR spectra and the dominating reaction is that with the aromatic ring.

It is normally essential for the ESR technique that the samples are deoxygenated. $^3\text{O}_2$ reacts with free radicals by spin exchange, but in particular it adds and thus forms peroxy radicals which are more difficult to see. Under fuel cell operating conditions there is plenty of $^3\text{O}_2$ present, at least near the cathode, but $^1\text{O}_2$ is not expected to form. Only under local pH inhomogeneities, $^1\text{O}_2$ should also be considered as a possible reaction pathway especially at $\text{pH} \geq 11.7$. In the presence of both HO^\bullet radicals and oxygen, complete degradation of the aromatic rings can be achieved within a few hours [66]. In view of this, the perfluorinated Nafion[®] which is much more inert has an inherent advantage over the new membranes based on aromatic hydrocarbons.

It is known that the sulfone group has a deactivating role. Thus, in comparison with the other monomeric building blocks SDP has an advantage in terms of chemical stability towards HO^\bullet addition. Furthermore, blocking of the aromatic ring by suitable substitution, for example by fluorine, limits the HO^\bullet addition reactions. SO_3^- substituents are introduced to give rise to proton conductivity, but as an additional benefit they reduce the activity of the aromatic ring towards hydroxyl radical addition (see Table 3). Another possibility, as briefly mentioned in the introduction, is the polymer blending. In DMFC, the most promising fuel cell performance is obtained on membranes based on sPEKs and their blends, and recent results indicate a power density as good as the ones obtained with Nafion[®], with the difference that polyaromatic membranes can be restarted over several weeks without degradation at temperatures $> 100^\circ\text{C}$ [29].

In addition future in-situ ESR experiments using a complete MEA in an operating fuel cell are needed to investigate the membrane under realistic and forced running conditions. Here,

radicals are no longer generated photolytically. Instead, it will be the key aim of these investigations to see whether the same radicals which are intermediates of the oxygen reduction can be liberated from the catalyst surface and cause their havoc on the membrane. Furthermore, spin trap agents are used to make elusive radicals visible. The novel method for a direct investigation of radical processes in a running fuel cell is already developed and first results have been reported [96].

Chapter 5

5 In-situ study of styrene grafting of electron irradiated fluoropolymer films

5.1 Results

5.1.1 Spin concentrations for FEP, ETFE and PVDF

The difference in the behavior of the three polymers upon irradiation can be understood based on the difference in typical relative bond strengths in fluoropolymers: $C-H < C-C < C-F$, so that that $C-H$ bond scission is expected to dominate in the case of ETFE and PVDF and $C-C$ bond scission in FEP. ETFE is expected to form a greater number of radicals per unit irradiation dose, thus lowering the irradiation dose required to achieve a particular level of grafting [84]. FEP probably forms fewer radicals because of greater bond energies (perfluorinated versus partially fluorinated), resulting in fewer bond breakages [84].

The spin concentrations of the polymers irradiated under Ar and air at 40 kGy are shown in Table 5 (only the starting values for the relevant peroxy or alkyl radicals are compared). Under air the radical yield is reduced by a factor of two for both ETFE and PVDF polymer films, but not for FEP. This may be related to the high oxygen solubility in perfluorinated media. The irradiation atmosphere and temperature play important roles in determining the effects of radiation processing on the base polymer. It should be noted that the energy deposited during irradiation is only partly spent for breaking bonds; another fraction is dissipated as heat so that the local temperature during irradiation exceeds the nominal ambient temperature. Irradiation under inert atmosphere leads to less oxidative degradation of the polymer film than in the case of irradiation in air, but irradiation under inert atmosphere is more expensive, because of the additional handling necessary [133]. It was reported that chain scission reactions could be minimized or even eliminated by using ETFE as the base polymer film, and by carrying out the pre-irradiation under inert atmosphere [84]. In contrast, although chain scission reactions in FEP could be minimized by carrying out the irradiation under inert atmosphere, they dominated under both oxygen-containing and inert atmospheres [84].

Table 5: Spin concentrations at 40 kGy electron radiation dose for FEP, ETFE and PVDF polymer films.

Polymer film	Irradiation atmosphere	Spin concentrations	
		10^{-6} mol spins g^{-1}	10^{-6} spins CX_2 unit *
FEP	Ar	1.9±0.5	95±25
FEP	air	2.9±0.7	145±35
ETFE	Ar	6.0±1.5	192±48
ETFE	air	3.9±1.0	124±32
PVDF	Ar	3.9±1.0	124±32
PVDF	air	2.3±0.6	74±19

* X = F or H

It is interesting that PVDF shows much lower spin concentrations compared to ETFE, although the structures are very similar. PVDF has a lower molar mass compared to the other two polymers (110'000 Dalton, compared to 400'000 and 325'000 for ETFE and FEP, respectively). Shorter polymer chains show less interaction between each other, thus the polymer chain mobility will be enhanced. The higher mobility leads to a higher termination probability during irradiation, causing more cross-links and a lower radical yield. Also, PVDF has a much lower glass temperature (-40 °C), so during the irradiation processing many of the generated radicals have sufficient time and mobility to recombine and create cross-links [134]. The higher mobility of the polymer chains is seen in the spectrum of PVDF at -120 °C (irradiated under Ar) where we already see a fine structure, and it is not better resolved by further heating to $+60$ °C (Fig. 23).

At lower radiation doses the spin concentrations for the three polymer films grow proportionally with the radiation dose. At higher doses the curves reach saturation levels because of partial recombination at high concentrations and elevated local temperature [57,135]. The spin concentration values for ETFE are always a factor of two higher than the corresponding values for FEP for both irradiation atmospheres, which is to be expected as mentioned earlier.

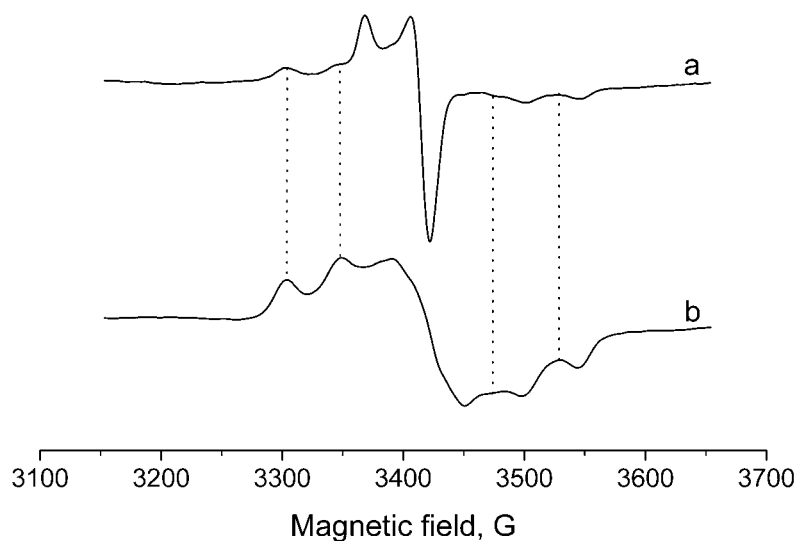


Fig. 23: *Teflon*-PVDF: a) peroxy radical at -120 °C, superimposed partly by alkyl radicals; b) alkyl radical at -120 °C.

5.1.2 Interpretation of ESR spectra obtained with FEP and ETFE

5.1.2.1 ESR spectra of irradiated FEP

High energy radiation can affect the molecular weight of a polymer through chain-scission and cross-linking [136]. Chain-scission and cross-linking occur simultaneously in an irradiated polymer, however, depending on the polymer structure, the environment and the conditions of the irradiation, one process will predominate [137]. The most expected radicals to be formed on high energy radiolysis of FEP irradiated under Ar arise from C–C or C–F bond scissions (see Fig. 24). In practice only a much smaller number of radical species have been positively identified, as will be discussed next.

Iwasaki and co-workers used ESR spectroscopy to study radical formation and thermal conversion in FEP that had been γ -irradiated with total doses of between 100 and 1000 kGy [138]. Three radical species were tentatively identified, and the main component was found to be the in-chain secondary radical species E. Another component was tentatively identified as a chain-end oxy radical, although it was unclear as to the source of the oxygen (the samples were irradiated under vacuum) and why an oxy radical was formed instead of a peroxy one

[138]. The third component was identified as the tertiary radical species F. Interestingly this tertiary radical was reported to be unstable and was easily converted photochemically into the primary radical G. This conversion could subsequently be reversed by a thermal annealing process [138]. It was subsequently found that radical G was one of the main radicals produced initially at low temperatures. This radical was quickly converted to the tertiary F as the sample temperature was increased [139]. The influence of oxygen on the radiation chemistry of FEP was investigated by Schlick and co-workers [140]. These investigators created peroxy labels in FEP copolymers by γ -irradiation under vacuum followed by subsequent exposure of the copolymer to oxygen. The γ -irradiation was found to generate mostly in-chain secondary radicals (species D and E), some chain-end primary radicals (species A), and perhaps a small amount of in-chain tertiary radical (species F). Addition of oxygen to the sample generated almost exclusively the in-chain peroxy radical, which was then used to study chain rotation and structure [140].

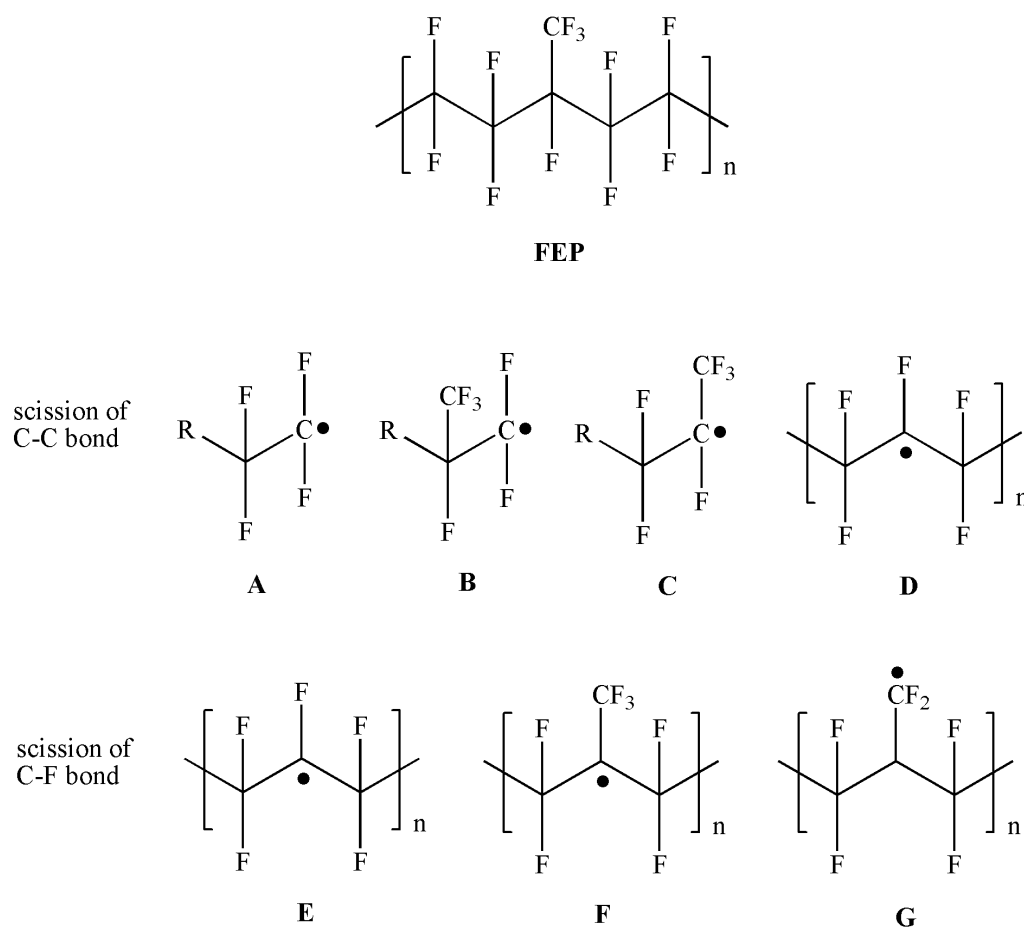


Fig. 24: Potential radical species formed in irradiated FEP.

Other radiation sources have also been investigated as a means for generating radicals in FEP. For example, two ESR studies of radicals in irradiated FEP were carried out using ultraviolet and vacuum ultraviolet radiation sources [141,142]. Two main radicals were found: a terminal and/or side group-based primary radical (species A, B or G) and an in-chain secondary radical (species D or E) [141]. However in a later study only a terminal primary radical and no secondary or tertiary radical species were observed [142].

In contrast to the earlier study of Iwasaki and co-workers, Hill and collaborators found that radiolysis at low temperatures led to the formation of mostly terminal primary radicals (species A) and some in-chain secondary radicals (species E) [143]. At higher temperatures the features of the secondary radicals became more prominent in the ESR spectra. The G-value for the total radical yield was determined at both 77 and 300 K. Interestingly the G-values and radical yields were higher at the higher temperature. The authors ascribed this difference to higher chain mobility limiting cage recombination at the higher temperature. The authors did not however attempt to quantify the relative content of the two identified radical species as a function of dose or temperature [143]. It was also shown that at 100 kGy and +80 °C the primary radical disappeared and only the resulting radicals from the C–F scission were identified [57]. At higher temperatures and under the influence of the irradiation dose the primary radicals may abstract an F-atom from the alkyl chains and thus transform into secondary radicals [144]. Furthermore, irradiation at elevated temperatures tends to increase the extent of radiation-induced cross-linking relative to chain scission, because of the increased mobility and thus rates of combination reactions, especially at temperatures above the glass or melting temperatures [133]. Therefore the irradiation dose and type, the irradiation atmosphere and temperature all play an important role in defining the effects of the radiation processing on the base polymer.

In the experimental ESR spectrum of FEP (e-beam irradiated at 40 kGy) and measured at +60 °C radicals A, E and F are identified by simulating the same radicals with the following coupling constants: $2F^{\beta}=16$ G, $g=2.0040$ for radical A; $1F^{\alpha}=83$ G, $4F^{\beta}=30$ G, $g=2.0030$ for radical E; $3F^{\beta}=23$ G, $4F^{\beta}=23$ G, $g=2.0020$ for radical F. The simulation is done using the WINEPR Simphonia program. Any anisotropic interactions could not be accounted for by the simulation software which assumes isotropic tensors. The ratio between the identified radicals obtained by the simulation is: 55% for radical A, 21% for radical E and 24% for radical F (Fig. 25).

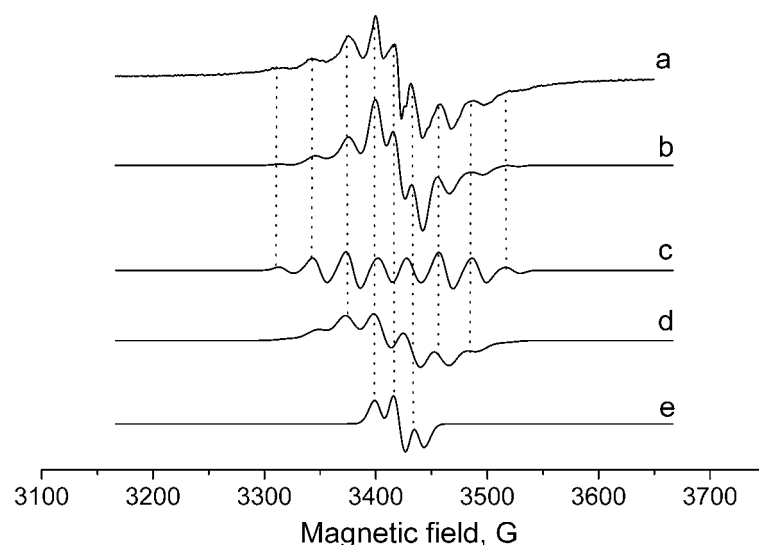


Fig. 25: a) Experimental spectrum obtained with FEP after electron irradiation under Ar; b) sum of all simulated radicals; c) simulation radical E; d) simulation radical F; e) simulation radical A.

The spectra obtained with FEP electron irradiated under air are typical of a peroxy radical with a clear g -anisotropy at $-120\text{ }^{\circ}\text{C}$ ($g_{\parallel}=2.0375$, $g_{\perp}=2.0080$, $g_{\text{iso}}=2.0178$) (Fig. 26). Increasing the temperature from $-120\text{ }^{\circ}\text{C}$ to $+80\text{ }^{\circ}\text{C}$ leads to changes in the g -factors as seen from Fig. 27 and at $0\text{ }^{\circ}\text{C}$ we have an isotropic g -factor ($g_{\text{iso}}=2.0141$). The transition to an isotropic spectrum is not due to the fast degradation of the anisotropic component, but it is due to a temperature dependent change in the averaged geometry of the radical and its motional degrees of freedom. It has been indicated from previous works that the peroxy mid-chain radical ($-\text{CF}_2\text{CF}(\text{OO}^{\bullet})\text{CF}_2-$) has axially symmetric g -values at room temperature ($g_{\parallel}=2.0055$, $g_{\perp}=2.0220$, $g_{\text{iso}}=2.0165$) whereas the peroxy end-chain radical ($-\text{CF}_2\text{CF}_2\text{OO}^{\bullet}$) has an isotropic g -factor at room temperature ($g_{\text{iso}}=2.0168$) [145,146]. At $+80\text{ }^{\circ}\text{C}$ the peroxy radical is converted into an alkyl radical (Fig. 26). Based on the bond dissociation energies it is expected that detachment of molecular oxygen, favored by the gain of entropy, is the most likely process of peroxy to alkyl conversion for both FEP and PE (see subchapter 6.1 for further details) [99].

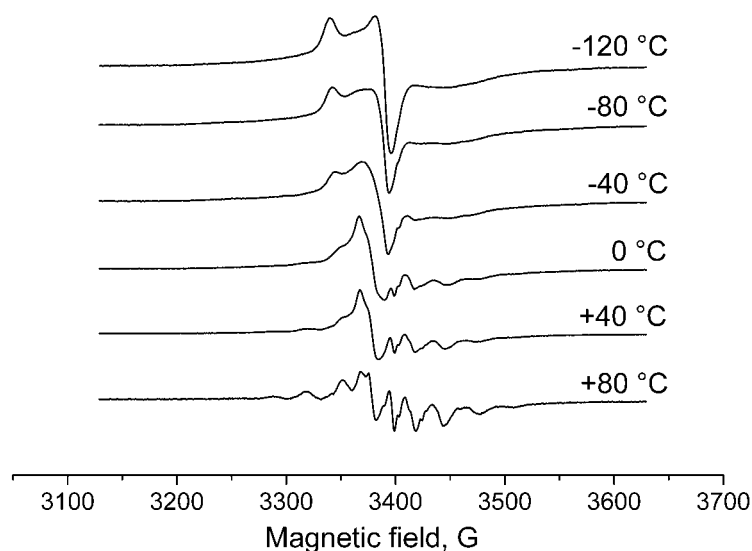


Fig. 26: Temperature dependence of ESR spectra obtained with FEP after electron irradiation under air.

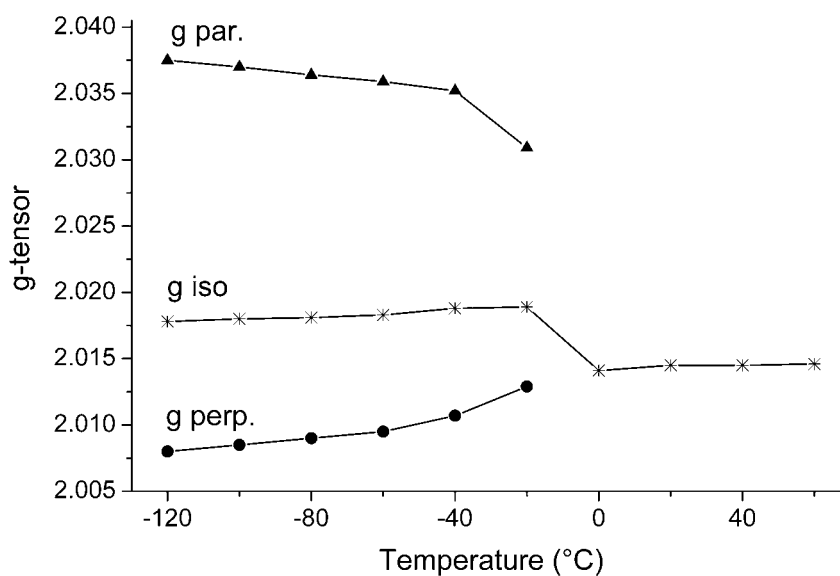


Fig. 27: Temperature dependence of the g-tensor of the peroxoradical obtained with FEP after electron irradiation under air.

5.1.2.2 ESR spectra of irradiated ETFE

Similar to the case of the other copolymer FEP, a large variety of radical species could potentially be formed upon irradiation of ETFE, as is shown in Fig. 28. Comparatively little work has been published about the radicals generated in ETFE upon irradiation, especially

under conditions similar to those used in the radiation grafting method for preparing membranes. For example, Kuzuya and co-workers investigated plasma-induced surface radicals on ETFE copolymers by means of ESR spectroscopy [147]. Two main radical species were identified and their concentration quantified, an in-chain secondary radical created by scission of a C–H bond (species F in Fig. 28) and a dangling bond site (DBS). The quoted coupling constants are: $1H^{\alpha}=28.8$ G, $2H^{\beta}=21.9$ G, $2F^{\beta}=28$ G, $g=2.0029$ [147]. The concentration of the in-chain secondary radical increased linearly with increased time of plasma treatment, whereas the concentration of the DBS was low but approximately constant for all irradiation times.

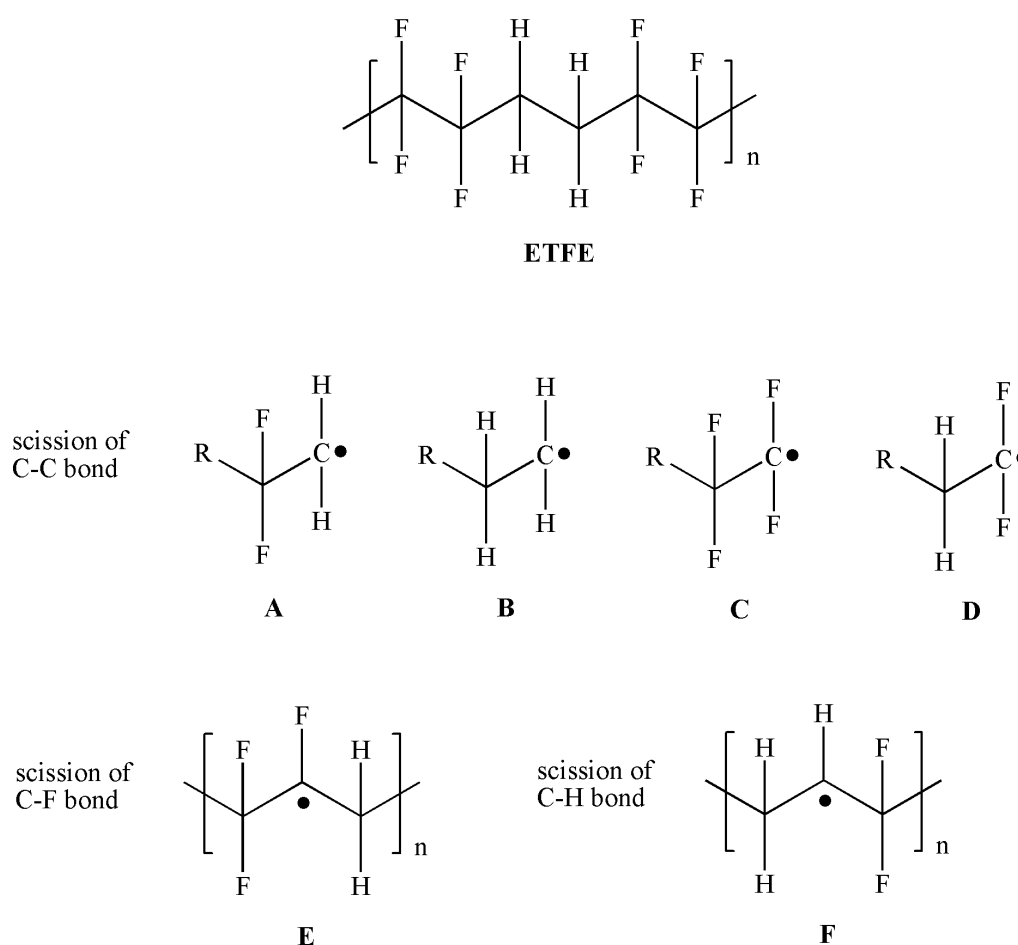


Fig. 28: Potential radical species formed in irradiated ETFE.

In the experimental ESR spectrum of ETFE (e-beam irradiated at 40 kGy) and measured at +60 °C radical F (98%) and radical E (2%) are confirmed by simulation of the same radicals with the following coupling constants: $1H^{\alpha}=23$ G, $2H^{\beta}=23$ G, $2F^{\beta}=25$ G, $g=2.0029$ for radical F; $1F^{\alpha}=93$ G, $2H^{\beta}=19$ G, $2F^{\beta}=24$ G for radical E (Fig. 29). The simulation is done using the WINEPR Simphonia program which assumes only isotropic tensors. The same

radicals were identified in a previous research work, just the radiation dose and measuring temperature were different [57]. This result coincides with the expectation that C–H bond scission will dominate in ETFE.

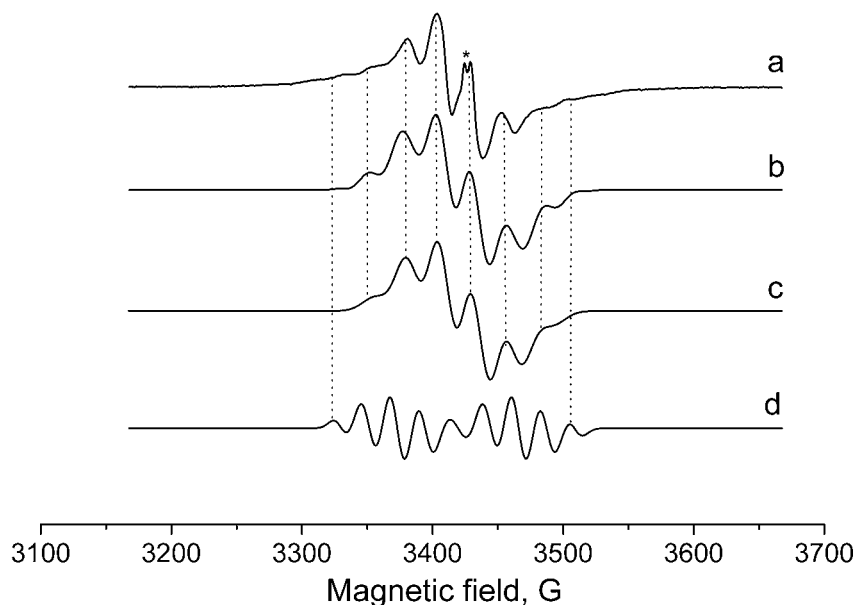


Fig. 29: a) Experimental ESR spectrum obtained with ETFE electron irradiated under Ar; b) sum of all simulated radicals; c) simulation radical F; d) simulation radical E; (* irradiated quartz).

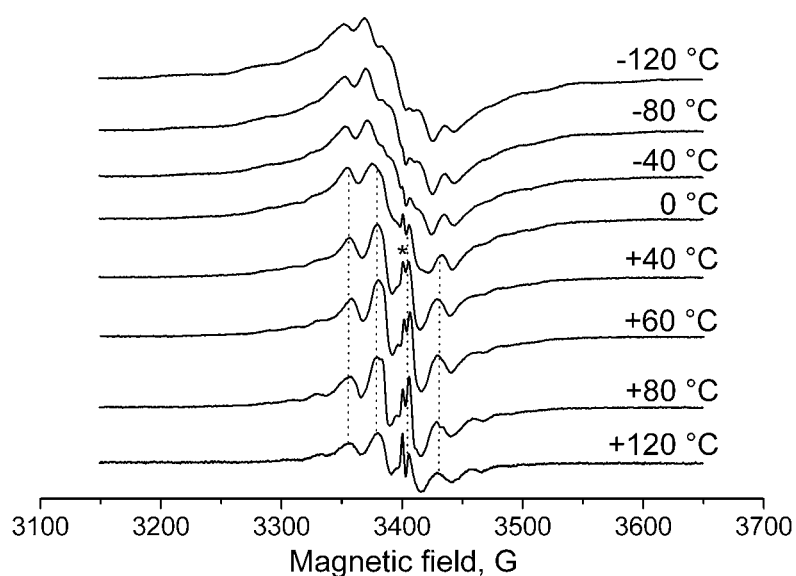


Fig. 30: Temperature dependence of ESR spectra obtained with ETFE after electron irradiation under Ar (* irradiated quartz).

In another experiment, ESR spectra obtained with ETFE irradiated under Ar were measured at different temperatures. There was no effect of the temperature on the ratio between the two different radicals - always radical F was the majority species (Fig. 30). Also no change was observed in the ratio between the radicals with time.

The spectra obtained with ETFE electron irradiated under air are typical of a peroxy radical with a clear g -anisotropy at -120 °C ($g_{\parallel}=2.0344$, $g_{\perp}=2.0081$, $g_{\text{iso}}=2.0169$). Again a clear temperature dependence of the g -tensor is observed (Figs. 31,32). The increase of temperature leads to a change in the values of g_{\parallel} and g_{\perp} and at -20 °C we have an isotropic g -factor ($g_{\text{iso}}=2.0113$). There are two possibilities for this transition: it is due to a temperature dependent change in the averaged geometry of the radical and its motional degrees of freedom, or alternatively the parallel axis of the g -tensor stands in a magic angle to the rotation axis of the peroxy group, leading to an averaging out of the anisotropy. Interestingly further annealing to $+80$ °C leads again to an anisotropic g -tensor (Fig. 31c). Thus, the rotation axis changes and a new anisotropy appears in which $g_{\perp} > g_{\parallel}$.

For FEP irradiated under air the spectrum at -120 °C differs from the spectrum obtained with ETFE by a slightly higher value of g_{\parallel} ($g_{\parallel}=2.0375$ for FEP, $g_{\parallel}=2.0344$ for ETFE) (Figs. 27,32). The stronger anisotropy is due probably to the side chains in the molecules. Side chains hinder the rotation around the main axis and hinder the averaging of the anisotropy.

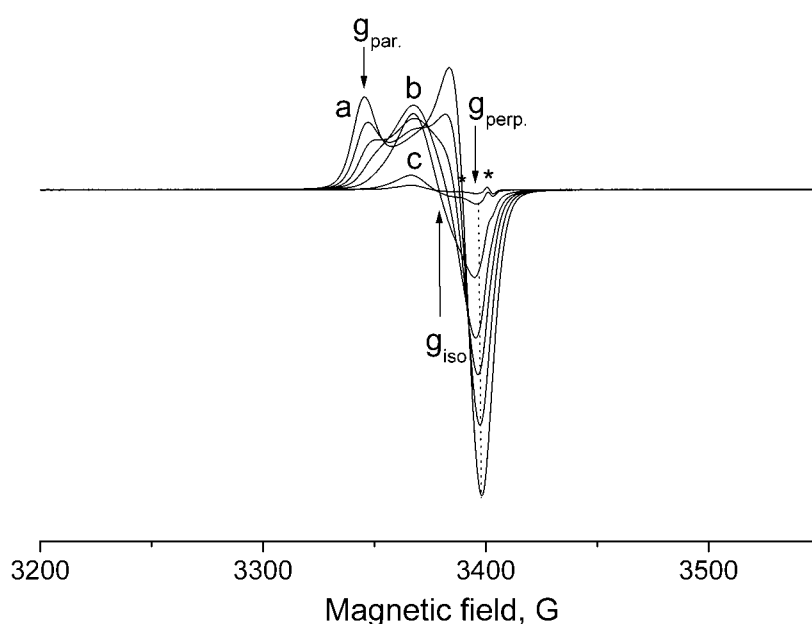


Fig. 31: Temperature dependence of ESR spectra obtained with ETFE after electron irradiation under air: a) -120 °C; b) 0 °C; c) $+80$ °C (* irradiated quartz).

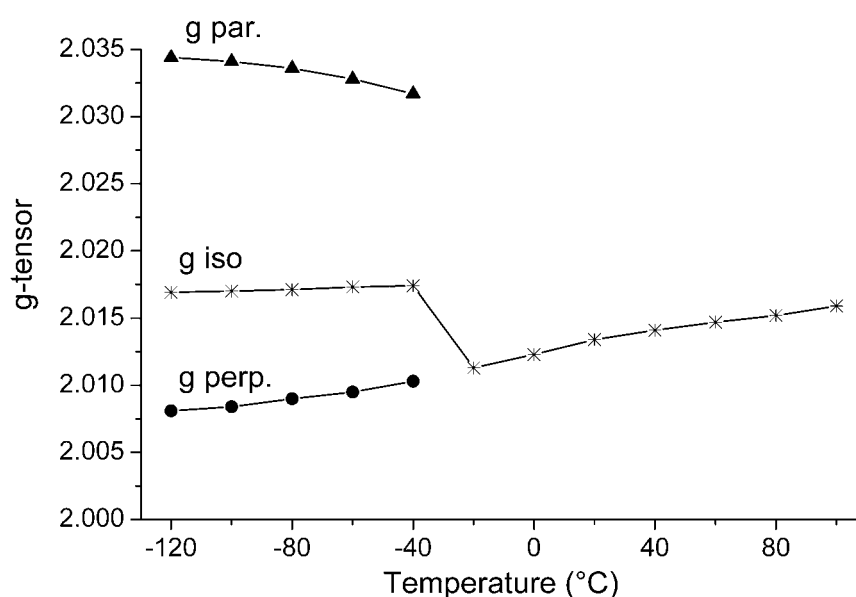


Fig. 32: Temperature dependence of the g -tensor of the peroxoradical obtained with ETFE after electron irradiation under air.

5.1.2.3 ESR spectra of irradiated PVDF

The radicals expected to be formed upon irradiation of PVDF under inert atmosphere are shown in Fig. 33. These radical types all involve α and β -fluorine or proton hyperfine couplings. Helbert and co-workers used ESR, ENDOR and infrared spectroscopies to study PVDF pellets irradiated by γ -irradiation with doses of up to 280 kGy [148]. These investigators observed a broad unresolved quintet and an abnormally intense central line in the ESR spectra of samples irradiated with doses of up to 100 kGy. They attributed these features to allylic and polyenyl radicals, respectively. In contrast to this work, Ilicheva et al. found that only the alkylfluoro primary end-chain and secondary in-chain radicals were formed (species B and C in Fig. 33) [149]. Aymes-Chodur et al. also found that the main radical species formed in γ -radiation processing of PVDF films in air was the secondary in-chain fluoroalkyl radical (species C) and the in-chain and end-chain peroxy radicals [77]. However Suryanarayana and co-workers reported that the alkyl primary end-chain radical was formed nearly exclusively with perhaps some low levels of the alkyl secondary in-chain radical (species A and D in Fig. 11) and they showed that the total spectral width was 220 G with $g \approx 2.002$ for radical A [150]. Exposure to oxygen resulted in the conversion to the corresponding end-chain peroxy radical. The total spectral width for the various radical types

considered, A to D, can roughly be approximated as about 170 G for radical A, 420 G for radical B, 300 G for radical C and 260 G for radical D [150].

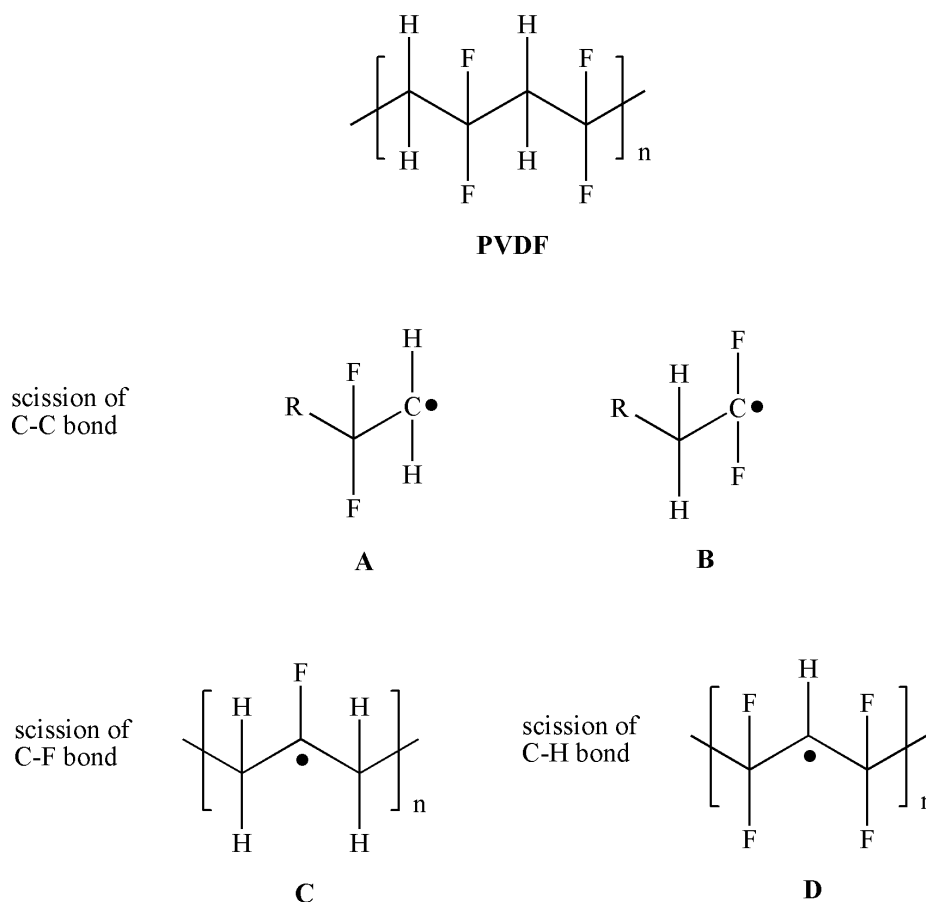


Fig. 33: Potential radical species formed in irradiated PVDF.

At $-120\text{ }^\circ\text{C}$ in the experimental ESR spectrum obtained with PVDF irradiated under Ar (Fig. 23) we already have a fine structure and it is not better resolved by further heating to $+60\text{ }^\circ\text{C}$, as mentioned before. The spectrum in Fig. 23b is quite symmetrical with a total width of about 300 G and $g \approx 2.002$. If we take into account only the total spectral width, the observed alkyl radical in our ESR spectrum corresponds probably to radical C but it is interesting that the g -factor is 2.002 - the same value quoted in ref. [150] and it was assumed that radical A was the species observed. We need better resolved spectra in order to be able to confirm the radicals formed by irradiation under inert atmosphere for PVDF. The quoted g -factors for the end-chain peroxy radical at 77 K are: $g_{\parallel}=2.037$, $g_{\perp}=2.005$ [150]. The g -factors at $-120\text{ }^\circ\text{C}$ in the experimental ESR spectrum obtained with PVDF irradiated under air

($g_{\parallel}=2.0355$, $g_{\perp}=2.0088$, Fig. 23a) are in a good agreement with the values above, but the possibility of having a mid-chain peroxy radical should however not be excluded.

5.1.3 Grafting of ETFE

Once we expose the samples to styrene in the preheated chamber ($t = 0$) at $+60\text{ }^{\circ}\text{C}$ the grafting reaction starts. The ESR spectra during styrene grafting onto ETFE under oxygen-free conditions at $+60\text{ }^{\circ}\text{C}$ are similar to the spectra corresponding to alkyl radicals in the absence of styrene (Fig. 34). No additional signals due to the propagating polystyryl radical are observed.

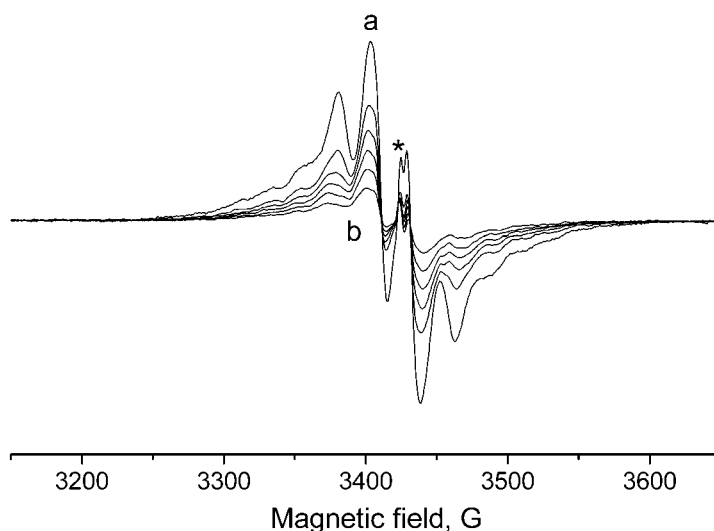


Fig. 34: ESR spectra during the grafting process of styrene on *Teflon*-ETFE (40 kGy) at $+60\text{ }^{\circ}\text{C}$: a) after 2 min; b) after 150 min (* irradiated quartz).

The ESR spectra during styrene grafting under air at $+60\text{ }^{\circ}\text{C}$ correspond to terminal peroxy radicals with a characteristic near-isotropic singlet signal ($g \approx 2.0155$). Weak traces of additional signals due to alkyl radicals are observed in the spectra of ETFE irradiated under air and grafted with styrene (Fig. 35). Interestingly, these signals were not present during thermal treatment without styrene at the same temperature, where only the typical isotropic signals of the terminal peroxy radicals appeared [57,135]. This may mean that the alkyl radicals are built up directly after the addition of styrene and simultaneous heating during the grafting process. Guilmeau et al. found that the rate of peroxy radical decay is much higher than the initial rate of styrene grafting, thus concluding that peroxy radicals do not initiate the grafting process [76]. The grafting reaction with ETFE is therefore expected to proceed over

alkyl radicals, which have been previously formed by hydrogen abstraction by the peroxy groups in the swollen regions of the polymer. Based on bond dissociation energies it is expected that detachment of molecular oxygen, favored by the gain of entropy, is the most likely process of peroxy to alkyl radical conversion for both FEP and polyethylene [99]. The detachment of atomic oxygen is unlikely. Peroxy radicals are also unlikely to abstract F from C–F bonds, but H-abstraction may compete with oxygen detachment to some extent. For alkoxy radicals (formed for example when peroxides are photolyzed, or when ether bonds are cleaved in polymers like Nafion[®]) abstraction of H but not F atoms is thermodynamically favored [99].

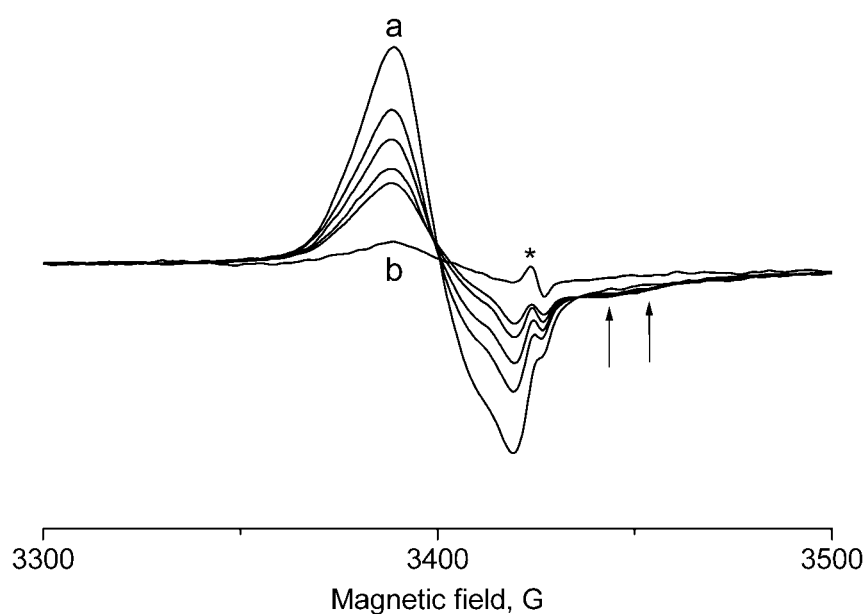


Fig. 35: ESR spectra during the grafting process of styrene onto peroxy radicals in *Teflon-ETFE* (40 kGy) at +60 °C: a) after 2 min; b) after 160 min (* irradiated quartz, arrows: alkyl radicals).

In the case of benzene after 1 hour we have anisotropic g -values ($g_{\perp} = 2.0212$, $g_{\parallel} = 2.0055$) compared with the isotropic g -factor obtained after 15 minutes grafting ($g = 2.0158$, Fig. 36). This is probably a pseudo-isotropic case (a planar hyperfine anisotropy) which on further averaging then becomes axial. In the first hour the radicals in the amorphous regime induce the grafting process, but what remains thereafter is located inside crystallites and therefore more anisotropic.

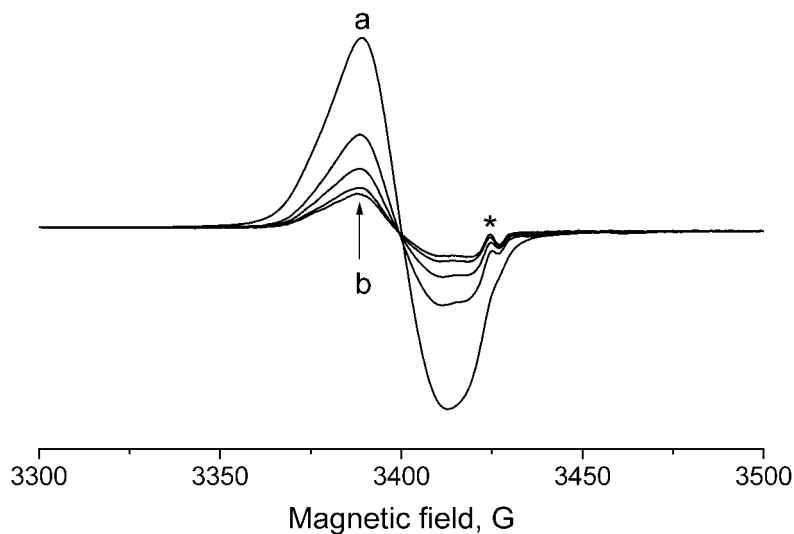


Fig. 36: ESR spectra during the grafting process of 25% styrene in benzene onto peroxy radicals in *Teflon-ETFE* (40 kGy) at +60 °C: a) after 2 min; b) after 180 min (* irradiated quartz).

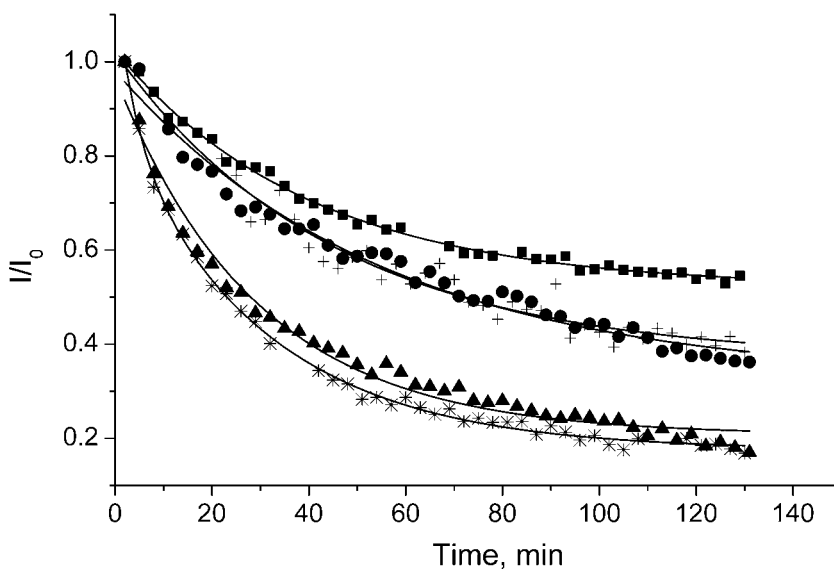


Fig. 37: Normalized intensities of the ESR spectra of ETFE radicals during the grafting process at +60 °C relative to their initial concentration: alkyl radicals, 25% styrene in benzene (■); peroxy radicals, 25% styrene in ethanol (+); alkyl radicals, styrene (●); peroxy radicals, styrene (▲); peroxy radicals, 25% styrene in benzene (*).

The influence of the diluent is also investigated for the grafting reactions at +60 °C (Fig. 37). ETFE peroxy radicals grafted with pure styrene and 25% styrene in benzene show a similar time dependence of the signal intensity. During the first 30 minutes, there is a fast

decay, and then the signal seems to reach a plateau. The decrease of radical concentration is correlated with the monomer penetration in the polymer films. In the case of ETFE-alkyl radicals grafted with styrene and ETFE-peroxy radicals grafted with 25% styrene in ethanol the decay is less rapid in the first 60 minutes, and after that no clear plateau is observed (Fig. 37). The highest intensities of the signals are obtained for ETFE-alkyl radical grafted with 25% styrene in benzene. At the same temperature (+60 °C) the grafting of styrene under inert atmosphere proceeds more slowly than under air.

Table 6: Solvent effect on the grafting reactions of *Teflon*-ETFE and *Teflon*-FEP at +60 °C ^{a)}.

Polymer film	Solvent	y_0	A_1	k_1	A_2	k_2
				10^{-2} min^{-1}		10^{-2} min^{-1}
FEP/peroxy	styrene	0.00 ^{b)}	1.00	4.5±0.2	0.00	–
FEP/peroxy	25% styr. in benz.	0.04±0.01	0.85±0.02	43±1	0.11±0.01	3.3±0.1
FEP/peroxy	25% styr. in EtOH	0.18±0.01	0.82±0.02	4.4±0.2	0.00	–
FEP/alkyl	styrene	0.05±0.13	0.95±0.12	2.5±0.5	0.00	–
FEP/alkyl	25% styr. in benz.	0.15±0.01	0.85±0.03	9.0±0.6	0.00	–
ETFE/peroxy	styrene	0.22±0.01	0.78±0.02	3.5±0.2	0.00	–
ETFE/peroxy	25% styr. in benz.	0.16±0.01	0.24±0.03	22±6	0.60±0.03	3.3±0.2
ETFE/peroxy	25% styr. in EtOH	0.36±0.02	0.64±0.03	2.2±0.2	0.00	–
ETFE/alkyl	styrene	0.34±0.02	0.66±0.02	1.9±0.2	0.00	–
ETFE/alkyl	25% styr. in benz.	0.51±0.01	0.49±0.01	2.5±0.1	0.00	–

a) fitting parameters are the normalized fractions A_i and pseudo-first order rate constants k_i according to eqn. (3-29).

b) This entry was fixed at zero to prevent it from going negative.

It is not possible to propose an exact mechanism for the grafting reactions from the curves for radical decay because of the simultaneous influence of several potential factors. For the grafting of styrene onto ETFE-peroxy radicals at 100 kGy radiation dose Guilmeau assumed a double exponential function. The early time (large k_1) was assigned to the full permeation of

the styrene monomer into the amorphous regions of the polymer, while the following longer reaction time (small k_2) described the reaction in the crystalline regions [76]. Dobo and Hedvig suggested that the curve for the signal intensities during the grafting reaction with ETFE consisted of several linear regions [88]. However, the experiment was done at lower temperature, and the films were considerably thicker (≈ 0.2 mm). In our experiments the resulting curves for radical decay of ETFE polymer film irradiated at 40 kGy fit better to a mono exponential function (except when benzene is used as a diluent for the peroxy radicals, Table 6). This gives rate constants which allow direct comparison of the grafting reactions under different experimental conditions.

5.1.4 Grafting of FEP

The ESR spectra during the grafting reactions of styrene onto FEP under oxygen-free conditions at +60 °C resemble the spectra corresponding to alkyl radicals without the addition of styrene (Fig. 38).

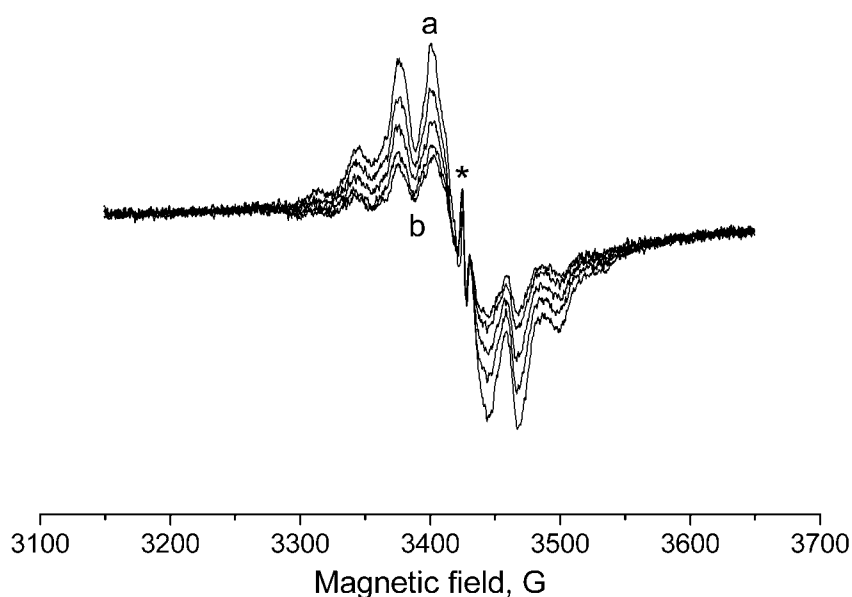


Fig. 38: ESR spectra during the grafting process of styrene on *Teflon*-FEP (40 kGy) at +60 °C: a) after 2 min; b) after 40 min (* irradiated quartz).

The ESR spectra during styrene grafting under air at +60 °C correspond mainly to terminal peroxy radicals with an isotropic g -value ($g \approx 2.0161$), but additional signals due to alkyl radicals are observed, suggesting that they are trapped in oxygen impermeable crystalline zones (Fig. 39).

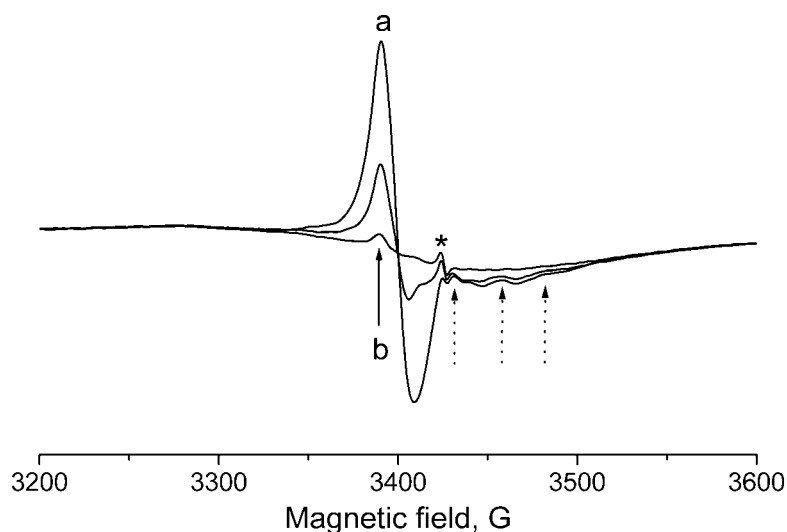


Fig. 39: ESR spectra during the grafting process of styrene onto peroxy radicals in *Teflon-FEP* (40 kGy) at +60 °C: a) after 2 min; b) after 60 min (* irradiated quartz, dotted arrows: alkyl radicals).

The influence of the diluent is investigated for the grafting reactions at +60 °C (Fig. 40), as done previously for ETFE. When FEP alkyl radicals are grafted with styrene the decay is very rapid. When grafting is done with 25% styrene in benzene we have a rapid decay of radicals during the first 30 minutes, then the decay reaches a plateau, but after 80 minutes almost all radicals have been consumed. We conclude that by this time the FEP crystallites are dissolved in benzene/styrene. When the FEP-peroxy radical is grafted with styrene the decay is rapid, and within 1 hour all peroxy radicals are consumed (Fig. 40). The signal of FEP peroxy radical grafted with 25% styrene in benzene decreases very rapidly in the first 10 minutes, and then the decay seems to reach a plateau. The survival of the radicals can be explained by the fact that radicals are trapped in crystallites impermeable to styrene. In the crystalline phase free radicals are very stable owing to reduced molecular motion, and the signals remain detectable even after 180 minutes. For FEP peroxy radical grafted with 25% styrene in ethanol a similar behavior is observed, only the decay is not that fast at the beginning of the grafting reaction and the intensity of the signals is higher. The radical decays follow a mono-exponential function (except for the peroxy radicals when benzene is used as a diluent, see Table 6).

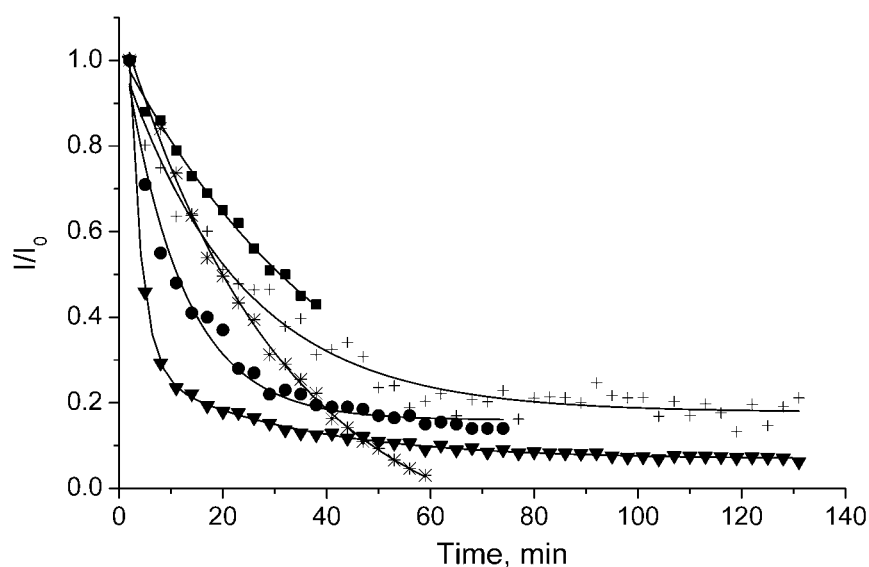


Fig. 40: Normalized intensities of the ESR spectra of FEP radicals during the grafting process at +60 °C relative to their initial concentration: alkyl radicals, styrene (■); peroxy radicals, 25% styrene in ethanol (+); alkyl radicals, 25% styrene in benzene (●); peroxy radicals, styrene (*); peroxy radicals, 25% styrene in benzene (▼).

It was shown that the grafting reactions with alkyl radicals (i.e. after irradiation under inert atmosphere) at +80 °C are about 8 times faster than at +60 °C [57,135]. At higher reaction temperatures the reactivity of all reaction partners is higher and the spreading of the grafted zones in the polymer obviously proceeds faster. Interestingly the signal intensities at +80 °C in the absence of styrene decayed much more slowly compared with the grafting reactions for both FEP and ETFE [57,135].

5.1.5 Grafting of PVDF

In the case of PVDF it was not possible to obtain reliable first or second integrals because of the unstable baseline in the spectra. For this reason we do not analyze these cases, but qualitatively the decay was faster than for FEP and ETFE. Also, in the spectra of PVDF irradiated under air and grafted with styrene, alkyl radicals are detected even at -120 °C, meaning that they are trapped in oxygen impermeable zones (Fig. 23). With time the peroxy radicals react away, but the alkyl do not, suggesting that they are located within crystallites.

5.2 Discussions

5.2.1 Styrene attachment products

It is difficult to discern in the ESR spectra any indication of the styryl radical at the end of the propagating polystyrene chain. At any time its concentration must be much lower than the initial radical concentration on the backbone. This means that the grafted chains grow very fast and terminate before a detectable concentration of styryl radicals has built up. Furthermore, each new monomer adds with random proton spin so that the line positions in an ESR spectrum may continuously switch for a given electron spin. As long as this process is sufficiently slow we expect to see a well-resolved spectrum of the propagating radical, as shown in [90], if it is too fast this should result in a singlet in the center, but at intermediate conditions the lines would be dynamically broadened and not detectable.

There are many influencing factors leading to a sufficiently high stationary concentration of styrene attachment products. For instance, the higher mobility of the substituted alkyl chains in FEP compared to ETFE should lead to narrower lines which should be more easily detectable but at the same time makes it easier to terminate. In the crystalline phase the thermal motion and decay of the radicals by termination is less pronounced. However, the grafting reaction of the peroxy radical proceeds over alkyl radicals, previously formed by hydrogen abstraction by the peroxy groups, or by the detachment of molecular oxygen favored by the gain of entropy, as mentioned before. This reaction assumes a high mobility of the polymer fragments and therefore proceeds preferentially in the more amorphous regions of the polymer.

5.2.2 The influence of crystallinity

Graft polymerization proceeds both, in the amorphous regions and at the surface of crystallites [151,152]. Radicals in the amorphous regions above the glass temperature are more accessible but have shorter lifetimes than radicals in crystalline regions. Moreover, because of chain mobility the termination rate in the grafting reaction is higher in the more amorphous regimes. Polymer crystallinity is well-known to be affected by radiation processing, and polymer irradiation can result in either increase or decrease in crystallinity. It can decrease due to the radiation-induced disruption of crystallite structure [70].

Alternatively, an increase can be due to the formation of short chain segments resulting from radiation-induced chain scission reactions and the subsequent ready crystallization of these mobile chain segments, especially at the elevated local temperatures occurring during film irradiation [70]. In previous experiments it was reported that crystallinity increases upon irradiation in the case of ETFE [84], while in contrast, it was shown that the pre-irradiation grafting with styrene results in a reduction of crystallinity for PVDF, ETFE and FEP polymer films [134].

The FEP films used here are to about 17% crystalline, and the partially fluorinated ETFE films to about 30% [87]. In agreement with literature [84], irradiation of ETFE under inert atmosphere at +60 °C leads to an increase in crystallinity, as the constant offset y_0 that is assumed to be related to a crystalline fraction which is not soluble in the grafting mixture is higher than the initial crystalline fraction (Table 6). Irradiation under air gives y_0 values that are lower or close to the initial crystalline fraction (Table 6). Irradiation of FEP under both air and Ar atmospheres leads to a decrease of inherent crystallinity, probably by partial disruption of the initial crystallites due to significant internal stress (Table 6). The crystallinity values of the base polymers would be expected to have some influence on the extent of grafting, because grafting is expected to occur primarily in the amorphous or amorphous/crystalline regions [70,71]. The crystalline fractions are always higher for ETFE compared to FEP, both before and after irradiation, suggesting that other factors, such as monomer transport into the film, extent of radical formation and compatibility or miscibility of the graft component and the base polymer, exert a controlling influence in the grafting process.

5.2.3 Grafting rates and influence of solvents

It was reported that the radical decay rates in inert atmosphere are about an order of magnitude larger at +80 °C than at +60 °C and the grafting under inert atmosphere at +80 °C is significantly faster than under air [57,135]. Interestingly for the grafting reactions under Ar at +60 °C this order seems to be reversed. It is not clear why this is so, but we should keep in mind that the rate constants presented here reflect the rate at which styrene reaches the initial radicals at the backbone, rather than chain propagation.

The prevailing view is that for the grafting process to be efficient, it is necessary to use a solvent that swells polystyrene grafts and thereby facilitates its penetration by the monomer. Neither the diluents nor the styrene swell the ungrafted polymer films significantly (ETFE swells slightly in benzene and styrene, and FEP does not measurably swell in either one [84]).

The effect of the diluents (here benzene and ethanol) is seen from Table 6. For FEP irradiated under Ar the decay of the radical signal in styrene diluted with benzene is nearly four times faster (although the benzene concentration is a factor of four lower!) than with pure styrene. For samples irradiated under air, the rate is accelerated by as much as a factor of ten by the benzene diluent. ETFE showed the same trends, but with somewhat lower enhancement factors. This may be taken as evidence of successful swelling and seems in clear contrast with literature [84]. However, it has to be taken into account that benzene may also react with the radical centers on the backbone chain. For a concentration of 25% styrene in benzene such a radical transfer may reduce the above enhancement by as much as a factor of four. Dilution by ethanol did not increase the grafting rate.

Both the crystallinity and the reaction rate are important for the grafting process. It appears that acceleration through the addition of benzene works only for the amorphous phase, while the crystallites are not dissolved more rapidly. This is seen most clearly during grafting of FEP with 25% styrene in benzene, where we first have a period of very rapid radical decay, followed by an extended plateau (Fig. 40).

5.2.4 Grafting levels

ETFE is expected to form a greater number of radicals per unit irradiation dose, thus lowering the irradiation dose required to achieve a particular level of grafting. Indeed the grafting levels for FEP are between 30% and 80% lower than those for ETFE on weight basis (Table 7). The effect gets less pronounced if considered per grafted backbone $\text{CF}_2(\text{CH}_2)$ unit (compare Table 5).

The higher grafting levels of ETFE compared with FEP or PVDF are due to the better diffusion of the styrene monomer into the polymer structure. ETFE swells during the storage in toluene at +60 °C with two mass-percent, while FEP shows no tendency of swelling [87]. This means that the penetration of the styrene monomer to reach the radical centers is easier for ETFE than for FEP. It is only surprising that in some cases the grafting level for FEP is higher than for PVDF, especially when irradiated under air (Table 7). PVDF has a much lower glass transition temperature and lower molar mass, as mentioned earlier, so during the irradiation processing many of the generated radicals have sufficient time and mobility to combine and create cross-links [134]. Therefore, the crystallinity and molar mass have a pronounced effect for PVDF, whereby the monomer transport into the film and the extent of radical formation, as well as the compatibility with the graft component are the limiting

factors for FEP and ETFE. Further clarifications and further experiments are needed for the grafting reactions with PVDF in order the results to be comparable with those obtained for FEP and ETFE.

Table 7: Grafting levels (eqn. 3-30) for grafting at +60 °C and average number of monomer units per chain at 40 kGy radiation dose in dependence on solvent.

Polymer film	Solvent	Graft level (wt.%)	Number of styrene units per chain
FEP / peroxy	styrene	15	800
FEP / peroxy	25% styrene in benzene	10	330
FEP / peroxy	25% styrene in ethanol	3	160
FEP / alkyl	styrene	62	3100
FEP / alkyl	25% styrene in benzene	14	790
ETFE / peroxy	styrene	21	550
ETFE / peroxy	25% styrene in benzene	14	400
ETFE / peroxy	25% styrene in ethanol	20	490
ETFE / alkyl	styrene	164	4900
ETFE / alkyl	25% styrene in benzene	35	550
ETFE / alkyl	25% styrene in ethanol	83	3300
PVDF / peroxy	styrene	9	480
PVDF / peroxy	25% styrene in benzene	9	370
PVDF / peroxy	25% styrene in ethanol	5	200
PVDF / alkyl	styrene	41	1000
PVDF / alkyl	25% styrene in benzene	40	1100
PVDF / alkyl	25% styrene in ethanol	39	1200

The use of diluent reduces the grafting levels compared to pure styrene for both ETFE and FEP irradiated under Ar (Table 7). Benzene should be present along with styrene in the grafted zones of the film, thus reducing the monomer concentration. In styrene/ethanol

solutions, however, styrene would diffuse alone in the grafted zone, as if the film is immersed in a pure styrene solution. Similar observations were made by Walsby et al. who investigated electron-beam irradiated PVDF grafted with styrene in propanol or toluene as a solvent [78]. Propanol reduces the monomer concentration in the outside solution, but in the grafted portions of the film styrene diffuses alone, while toluene diffuses competitively with styrene through the grafted portions of the film. In the case of ETFE irradiated under air we have similar values for the grafting levels when the three solvents are used. For FEP irradiated under air the use of 25% styrene in ethanol leads to 3% grafting level, compared with 15% when pure styrene is used (Table 7). Probably ethanol reacts with the radical, and the radical center is transferred to the ethanol molecule. It is possible during the extraction with toluene that these chains are washed out, which will surely lead to lower grafting levels.

The grafting levels reported here were determined after the ESR detectable initial radical signal had disappeared, which was between one and four hours after initiation of grafting (see corresponding figures). Since chain propagation radicals are not observed it should be considered that grafting could have proceeded further if not interrupted. It has been reported that completion of the grafting process under similar conditions may take several days [71], reaching grafting levels which exceed the data in Table 7.

Based on the spin concentrations and the grafting levels we estimate the number of monomer units per chain (Table 7). The trend is PVDF < FEP < ETFE for both peroxy and alkyl radicals. Another interesting observation is that the number of monomer unit per chain is always higher for alkyl radicals compared to peroxy radicals for the three polymer films. Apparently the grafting reactions under Ar atmosphere at +60 °C lead to the formation of longer polymer chains and a lower number of cross-links, while the reactions under air result in a higher number of short polymer chains. Therefore, the irradiation atmosphere (air vs. inert atmosphere) plays an important role in determining the effects of radiation processing on the FEP, ETFE and PVDF polymer films.

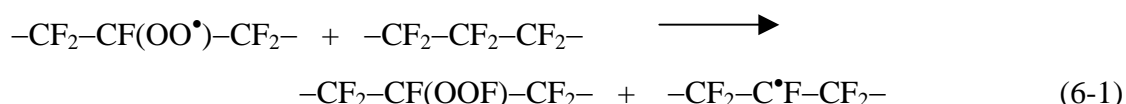
The correct choice of solvent is one of the essential elements towards the success of the radiation-induced grafting process. If the solvent has a high chain transfer constant, the growing chain will terminate quickly, leading to low graft levels [70]. This is confirmed by inspection of Table 7 which shows that in all cases except perhaps PVDF both, benzene and ethanol, decrease the grafting level considerably. It was reported as well that the solvent used in the grafting reactions with PVDF has a considerable impact on the surface aspect of the film [78]. Therefore, a compromise between many factors influencing the grafting process has to be found in order to achieve satisfactory degrees of grafting.

Chapter 6

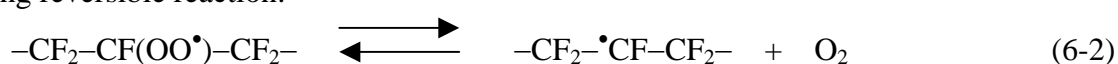
6 Comparative DFT study of non-fluorinated and perfluorinated alkyl and alkyl-peroxy radicals

6.1 Bond dissociation energies (BDEs) and reaction enthalpies

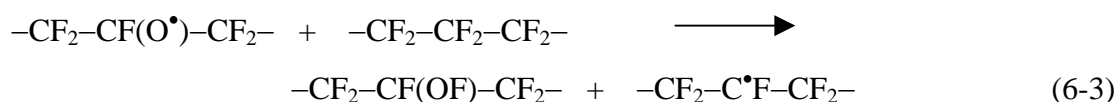
In ESR experiments with electron beam irradiated FEP under air it was observed that upon thermal annealing peroxy radicals are converted into alkyl radicals (see subchapter 5.1.2.1). A similar phenomenon was observed by Oshima et al. in their experiments with PTFE [153,154]. They suggested that peroxy radicals may abstract F-atoms from neighboring PTFE molecules, e.g.



It is well known that the C–F bond is very stable. From this view point it is not favorable for the peroxy radical to abstract an F-atom. Alternatively, the peroxy radical could detach molecular oxygen at higher temperature. Matsugashita and Shinohara [155] proposed in their experiments with non-cross-linked PTFE that the conversion mechanism is simply the following reversible reaction:



Aiming at an understanding of the relative importance of the above reactions (6-1) and (6-2) a comparative DFT study of non-fluorinated and perfluorinated alkyl and alkyl-peroxy radicals is conducted. Since alkoxy radicals may also occur in these systems, the radical transfer reaction is also contrasted with the analogous transfer reaction of the alkoxy radical:



Tables 8 and 9 summarize BDEs for primary, secondary and tertiary C–F and C–H bonds of the fluorinated (FC) and non-fluorinated (HC) alkyl model compounds. The experimental strengths for C–H bonds are $398 \pm 4 \text{ kJ mol}^{-1}$ and $385 \pm 4 \text{ kJ mol}^{-1}$ for *i*-C₃H₇–H and *t*-C₄H₉–H molecules, respectively [156]. The value for a secondary C–F bond is 443.9 kJ

mol^{-1} in *i*-C₃H₇-F [157]. Thus, where comparable experimental bond strengths are available they are close to the calculated ones in Table 8.

No experimental values are available for RO-O• peroxide bonds. The calculated BDEs are close to 70% of those of a C-H bond in HCs and near 50% of the ones for C-F in FCs. Again weaker is the C-OO• bond, in particular for the tertiary FC where it amounts to only 19.1 kJ mol⁻¹. The difference between the C-OO• bond strengths of the HC fragments is much smaller than that among the FCs, and substitution of H by F has a very pronounced effect.

Table 8: Bond dissociation energies for primary, secondary, and tertiary peroxy radicals (kJ mol⁻¹).

System	E _{C-OO•}	E _{O-O•}	E _{C-F} ^{a)}	E _{C-H} ^{a)}
CH ₃ CH ₂ CH ₂ (OO•)	123.2	244.9	-	412.0
CH ₃ CH ₂ CH(OO•)CH ₂ CH ₃	122.4	243.3	-	397.7
CH ₃ CH ₂ CCH ₃ (OO•)CH ₂ CH ₃	117.9	243.6	-	387.6
CF ₃ CF ₂ CF ₂ (OO•)	107.9	220.4	478.2	-
CF ₃ CF ₂ CF(OO•)CF ₂ CF ₃	59.0	182.3	433.3	-
CF ₃ CF ₂ CCF ₃ (OO•)CF ₂ CF ₃	19.1	194.6	386.0	-

a) BDE for F or H in place of (OO•)

Table 9: Bond dissociation energies for primary, secondary, and tertiary peroxide molecules (kJ mol⁻¹).

System	E _{OO-F}	E _{O-OF}	E _{OO-H}	E _{O-OH}
CH ₃ CH ₂ CH ₂ (OOH)	-	-	335.0	151.6
CH ₃ CH ₂ CH(OOH)CH ₂ CH ₃	-	-	331.5	146.5
CH ₃ CH ₂ CCH ₃ (OOH)CH ₂ CH ₃	-	-	323.1	138.4
CF ₃ CF ₂ CF ₂ (OOF)	110.7	120.8	-	-
CF ₃ CF ₂ CF(OOF)CF ₂ CF ₃	98.8	70.7	-	-
CF ₃ CF ₂ CCF ₃ (OOF)CF ₂ CF ₃	102.5	86.7	-	-

Comparison of the entries of Table 10 shows that all of the suggested reactions are endothermic, but there are large differences. The fluorine abstractions (reaction 6-1) are endothermic by more than 270 kJ mol⁻¹, those of H only between 50 and 90 kJ mol⁻¹. Cleaving off O₂ (reaction 6-2) costs between 19 kJ mol⁻¹ (tertiary FC) and 108 kJ mol⁻¹ (primary FC), and about 120 kJ mol⁻¹ for all HCs. However, one should keep in mind that this detachment reaction is entropically strongly favored relative to H or F abstraction. We suppose that nearly the complete translational and rotational entropy of O₂ (205 J mol⁻¹ K⁻¹ at 298 K) is gained on detachment. This would lead to an available entropic contribution $T\Delta S$ of about 60 kJ mol⁻¹ at standard temperature and pressure, as an upper limit, to offset the endothermicity. Detachment of O₂ should therefore be the most likely reaction, but abstraction of a secondary, or tertiary H but not of F should also be possible to some extent. The O–O bond should remain intact, although fluorine clearly destabilizes this bond.

Table 10: Reaction enthalpies $\Delta_R H$ of reactions (6-1) and (6-2) (kJ mol⁻¹).

Reacting radical	$\Delta_R H$ (6-1)			$\Delta_R H$ (6-2)
	primary ^{a)}	secondary ^{a)}	tertiary ^{a)}	
	H / F	H / F	H / F	
CH ₃ CH ₂ CH ₂ (OO•)	77 / -	63 / -	53 / -	123
CH ₃ CH ₂ CH(OO•)CH ₂ CH ₃	81 / -	66 / -	56 / -	122
CH ₃ CH ₂ CCH ₃ (OO•)CH ₂ CH ₃	89 / -	75 / -	65 / -	118
CF ₃ CF ₂ CF ₂ (OO•)	- / 368	- / 323	- / 275	108
CF ₃ CF ₂ CF(OO•)CF ₂ CF ₃	- / 379	- / 335	- / 287	59
CF ₃ CF ₂ CCF ₃ (OO•)CF ₂ CF ₃	- / 376	- / 331	- / 284	19

^{a)} abstracted atom

In some cases it may be possible that alkoxy radicals are formed, for example when peroxides are photolyzed, or when ether bonds are cleaved in polymers like Nafion[®]. The BDEs of these radicals with H and F atoms are given in Table 11 and the reaction enthalpies for the abstractions (reaction 6-3) in Table 12. It is seen that O–F bonds are quite weak, and abstractions of the strongly bound F from the carbon backbone is endothermic by 250-390 kJ mol⁻¹ and therefore not considered a serious reaction pathway. However, alcoholic O–H bonds are somewhat stronger than C–H bonds, so that H-abstraction by alkoxy radicals is slightly exothermic and therefore a suitable way for the conversion of alkoxy to alkyl radicals.

Table 11: Bond dissociation energies for primary, secondary, and tertiary alcohol OH and OF bonds (kJ mol^{-1}).

System	$E_{\text{CO-F}}$	$E_{\text{CO-H}}$
$\text{CH}_3\text{CH}_2\text{CH}_2\text{OH}$	-	418.3
$\text{CH}_3\text{CH}_2\text{CH}(\text{OH})\text{CH}_2\text{CH}_3$	-	416.4
$\text{CH}_3\text{CH}_2\text{CCH}_3(\text{OH})\text{CH}_2\text{CH}_3$	-	417.6
$\text{CF}_3\text{CF}_2\text{CF}_2\text{OF}$	132.1	-
$\text{CF}_3\text{CF}_2\text{CF}(\text{OF})\text{CF}_2\text{CF}_3$	92.5	-
$\text{CF}_3\text{CF}_2\text{CCF}_3(\text{OF})\text{CF}_2\text{CF}_3$	103.8	-

Table 12: Reaction enthalpies $\Delta_{\text{R}}H$ of reaction (6-3) (kJ mol^{-1}).

Reacting radical	$\Delta_{\text{R}}H$ (6-3)		
	primary ^{a)}	secondary ^{a)}	tertiary ^{a)}
	H / F	H / F	H / F
$\text{CH}_3\text{CH}_2\text{CH}_2\text{O}^\bullet$	-6 / -	-4 / -	-6 / -
$\text{CH}_3\text{CH}_2\text{CH}(\text{O}^\bullet)\text{CH}_2\text{CH}_3$	-21 / -	-19 / -	-20 / -
$\text{CH}_3\text{CH}_2\text{CCH}_3(\text{O}^\bullet)\text{CH}_2\text{CH}_3$	-31 / -	-29 / -	-30 / -
$\text{CF}_3\text{CF}_2\text{CF}_2\text{O}^\bullet$	- / 346	- / 386	- / 374
$\text{CF}_3\text{CF}_2\text{CF}(\text{O}^\bullet)\text{CF}_2\text{CF}_3$	- / 301	- / 341	- / 330
$\text{CF}_3\text{CF}_2\text{CCF}_3(\text{O}^\bullet)\text{CF}_2\text{CF}_3$	- / 254	- / 294	- / 282

^{a)} abstracted atom

An alternative reaction which is well known and therefore not in the focus here but reproduced well by the BDEs in Table 8 is radical transfer between hydrocarbon residues. In this exothermic reaction primary (secondary) radicals can be stabilized by abstraction of a secondary (tertiary) hydrogen or fluorine atom. Primary and secondary radicals are the most abundantly observed alkyl radicals in irradiated FEP and PTFE polymer films in the absence of oxygen [143,154]. It was concluded that chain motion plays a determining role on the extent of radical transfer and termination, and thus on the observed final distribution of radical species upon irradiation. The concentration of secondary alkyl radicals in FEP increases by radical transfer at cost of primary radicals, as the absorbed radiation dose

increases. Furthermore, the primary radicals are more mobile and undergo radical-radical termination reactions more readily as the overall radical concentration in FEP rises [143]. Surprisingly, the energetically more stable tertiary radicals decay much faster than the other radicals when thermally annealed since they are trapped in a region where the regular crystallization of the copolymer chains is perturbed by CF_3 groups [138]. The longevity of the radicals can lead to efficient post-irradiation chemistry, such as that required for surface grafting or surface oxidation.

6.2 Optimized geometries and charge distributions

We now turn to geometries and charge distributions. It is interesting that the C–C, C–F and C–H bonds neighboring the radical center are always longer for the peroxy radicals than for the alkyl radicals. The difference is very apparent for C–C bond length of the secondary and tertiary fluorinated fragments, where O_2 addition leads to an extension of ca. 0.07 Å (Figs. 42,43). This may formally be rationalized by a repulsive Coulomb interaction, since the total atomic charges are negative for both the *alpha* and the *beta* C atoms of these peroxy radicals. Also the C– CF_3 (C– CH_3) bonds are longer for the peroxy than for the alkyl radicals (Fig. 43). In general, substituting H-atoms by F leads to a slight extension of neighboring C–C bonds by approximately 0.05 Å for the peroxy radicals, and between 0.007 and 0.03 Å for the relevant alkyl radicals (Figs. 41-43). This can be understood by taking into account that the steric repulsion between the neighboring fluorine atoms is stronger than that between the hydrogen atoms, due to the larger radius of the F atom. For comparison, the calculated lengths using the Perdew-Zunger LDA were reported to be 1.54 Å for the C–C bond of PTFE and 1.51 Å for polydifluoroethylene [158], and the experimental bond lengths in crystalline polyethylene are 1.527 Å [159]. Thus, our calculated values agree with experiments as well as with previous theoretical studies [159,160].

Inspection of the bond lengths and the BDEs shows that the O–O bond is slightly longer for the fluorinated peroxy radicals compared with the non-fluorinated ones (Figs. 41-43). As expected, the shorter bond is the stronger one (Table 8). Surprisingly, the opposite behavior is found for the C– OO^\bullet bonds, where the stronger bonds (those of the HCs) are the longer ones. The C– OO^\bullet bond becomes significantly polarized in the fluorinated peroxy radical (by 0.26, 0.91 and 0.32 e for the primary, secondary and tertiary radicals, respectively, compare Figs. 41-43).

Introduction of F in place of H changes dramatically the electronic profile of a molecule. Fluorine is highly electronegative and withdraws electron density from C and also from O atoms. This is the reason for the less negative atomic charges of O in the fluorinated peroxy radicals. In the HC some electron density is transferred from hydrogen to the C backbone, while in the case of the FC we have the opposite behavior. Interestingly, the in-chain carbon atoms of the FCs remain negatively charged, but those of the CF₃ groups and the primary and secondary but not the tertiary radical center change sign, also the carbon next to the attached dioxygen of the peroxy compounds.

Geometry and charge distribution of the secondary and tertiary peroxy radicals are fully or nearly symmetric on reflection at the radical center. The C–C backbone of these structures represents to a good approximation an all-trans conformation. This holds also for the secondary HC alkyl radical, but the symmetry is slightly broken for the optimized structures of the secondary FC and the tertiary HC and FC alkyl radicals in which we find gauche elements. The energies of these broken symmetry structures are not much and perhaps not significantly lower than those of the corresponding all-trans secondary minima. More interesting is the slight C–C bond length inequivalence and in particular the charge polarization, amounting up to nearly 0.4 *e*, that results from the broken symmetry. It is known that C–F bonds are rather susceptible to stereoelectronic effects and orientate very specifically relative to C=O and C–N bonds [161], and for the present FC alkyl radicals it could mean that they possess quite a different chemical reactivity from the all-trans than from the gauche conformation.

In the case of the •CH₃ radical, current evidence suggests a planar or near-planar equilibrium geometry. In contrast, •CF₃ and •CCl₃ radicals, on the basis of EPR spectra, were judged pyramidal [162]. An interesting observation was the hyperfine coupling constant of ¹³C in the series •CH₃, •CH₂F, •CHF₂, •CF₃, with values of 38.3 G, 54.8 G, 148.8 G and 271.6 G, respectively [163]. The trend is explained by an increasing non-planarity with increasing fluorine substitution. The present calculations do not provide evidence for significant deviations from planarity, except for the primary FC alkyl radical for which the sum of the three bond angles at the radical center, 343°, demonstrates significant non-planarity due to double F substitution.

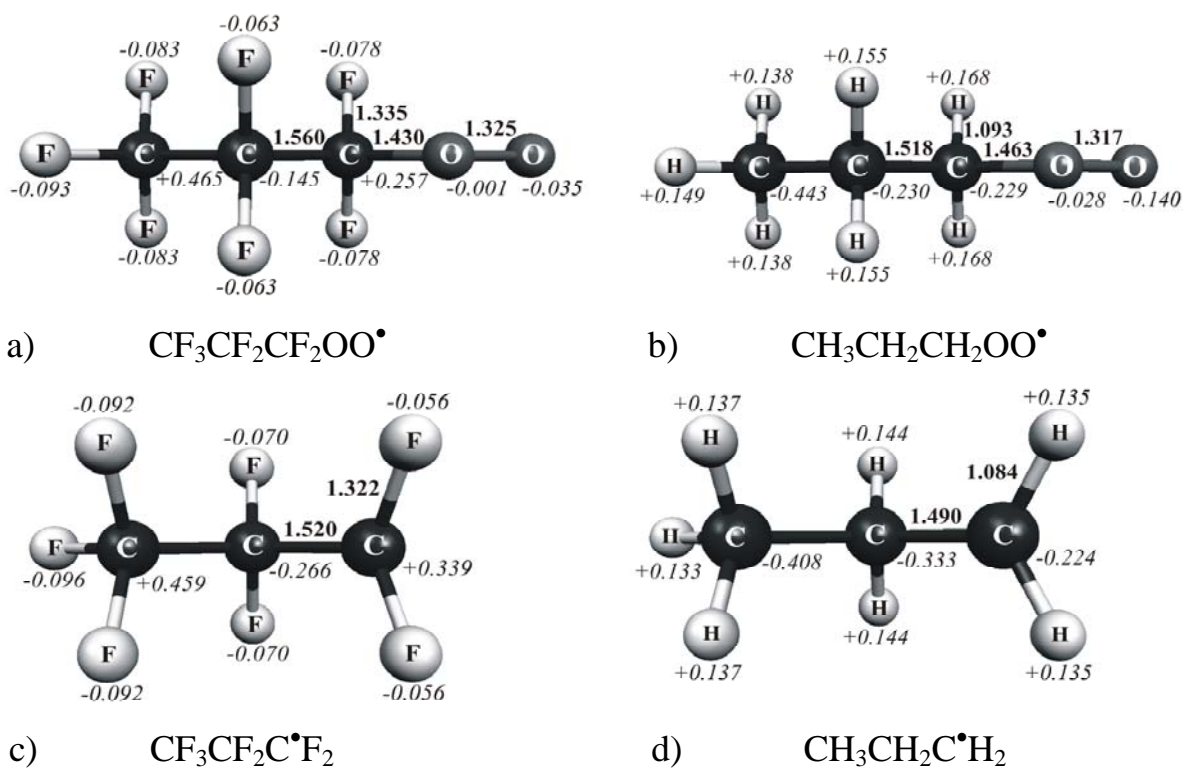


Fig. 41: Optimized geometries of non-fluorinated and perfluorinated primary alkyl and alkyl-peroxy radicals (selected bond lengths in Å (bold), total atomic charges in a.u. (italics)).

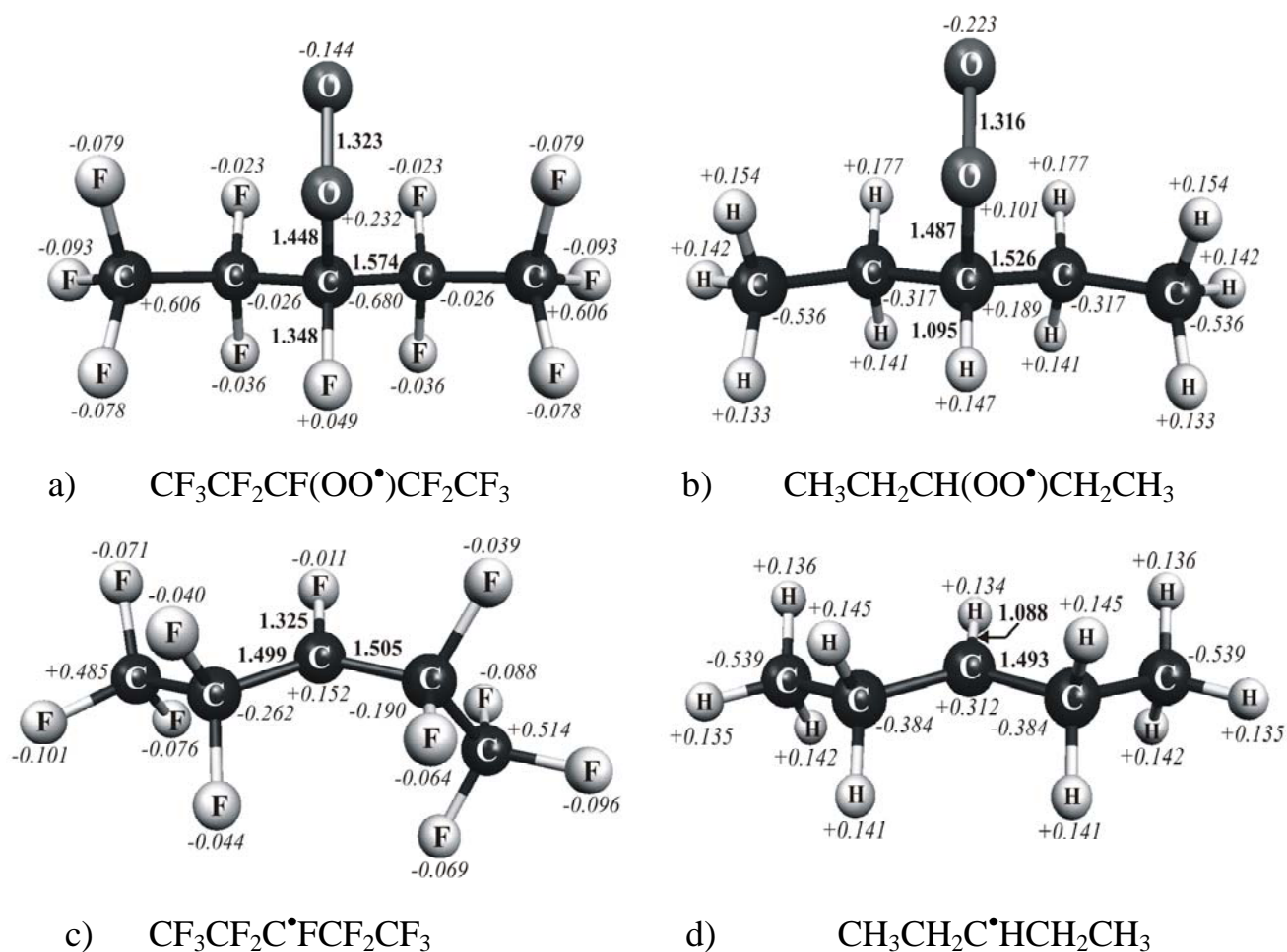


Fig. 42: Optimized geometries of non-fluorinated and perfluorinated secondary alkyl and alkyl-peroxy radicals (selected bond lengths in Å (bold), total atomic charges in a.u. (italics)).

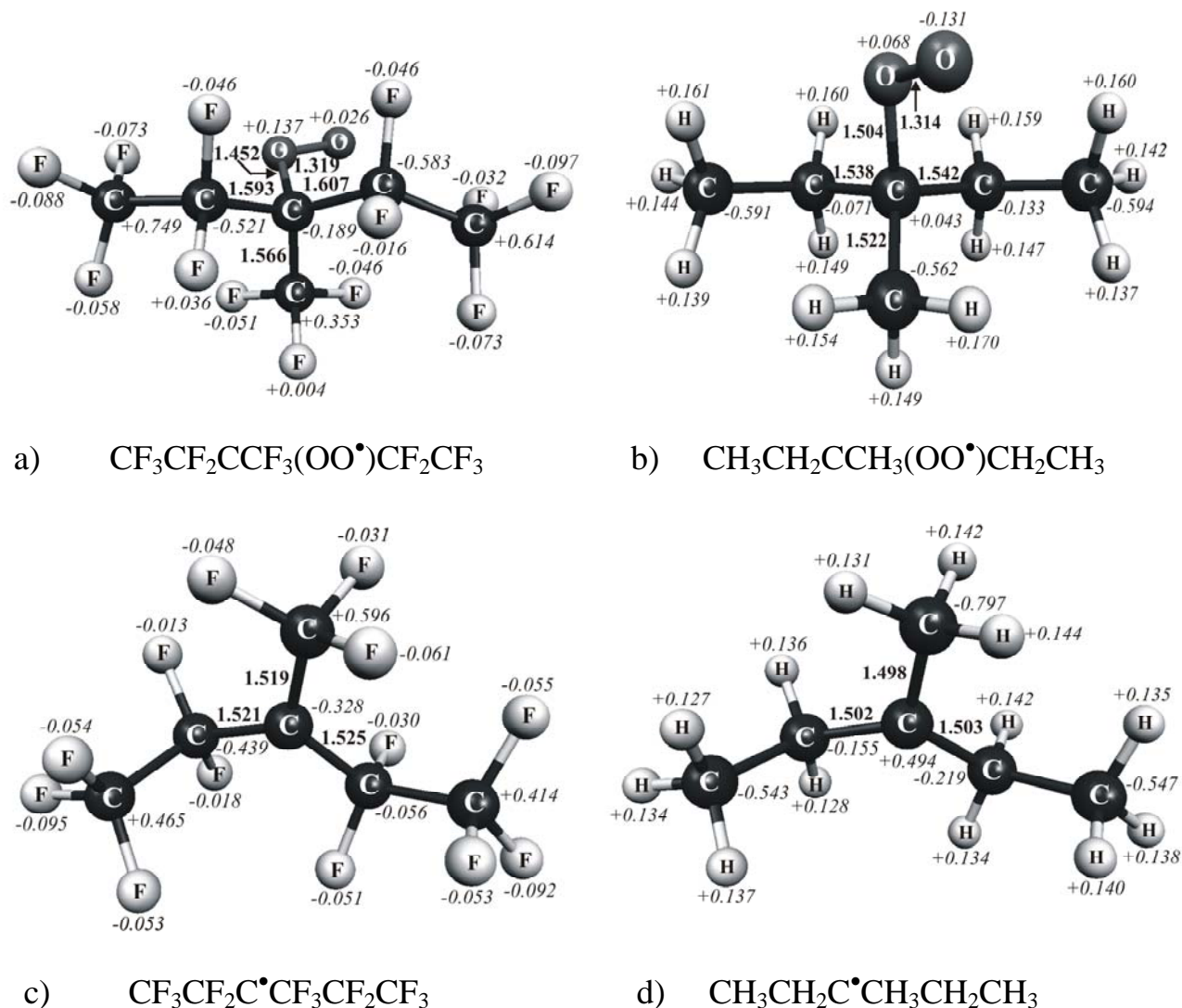


Fig. 43: Optimized geometries of non-fluorinated and perfluorinated tertiary alkyl and alkyl-peroxy radicals (selected bond lengths in Å (bold), total atomic charges in a.u. (italics)).

6.3 Energy barriers to internal rotation

Both the non-fluorinated and the forced planar fluorinated ethyl radicals exhibit a small six-fold potential on the order of 0.1-0.2 kJ mol⁻¹ for the internal rotation about the C^α-C^β bond. In both cases the energy minimum is calculated to be for $\theta = 0$, which points to a slight stabilizing hyperconjugative effect due to the overlap of the C-H (F) bond with the half-filled p_z orbital in the eclipsed conformation (Fig. 44). Admitting non-planarity for the radical centre of CF₃•CF₂ leads to a stabilization by 26 kJ mol⁻¹, but the threefold potential for internal rotation with all other parameters fully relaxed amounts to only 9.3 kJ mol⁻¹ (see Fig. 45). In the latter motion the radical centre does not invert. The energy minimum is now obtained for the conformation in which a C-F bond is anti-periplanar to the major lobe of the sp^3 like semi-occupied atomic orbital at the radical centre (Fig. 44).

Substitution of one of the β -H (F) atoms by a CH₃ (CF₃) group leads to a somewhat more complex potential which amounts, however, to only on the order of 1 kJ mol⁻¹ for the planar species, while it remains at 9-10 kJ mol⁻¹ for CF₃CF₂•CF₂.

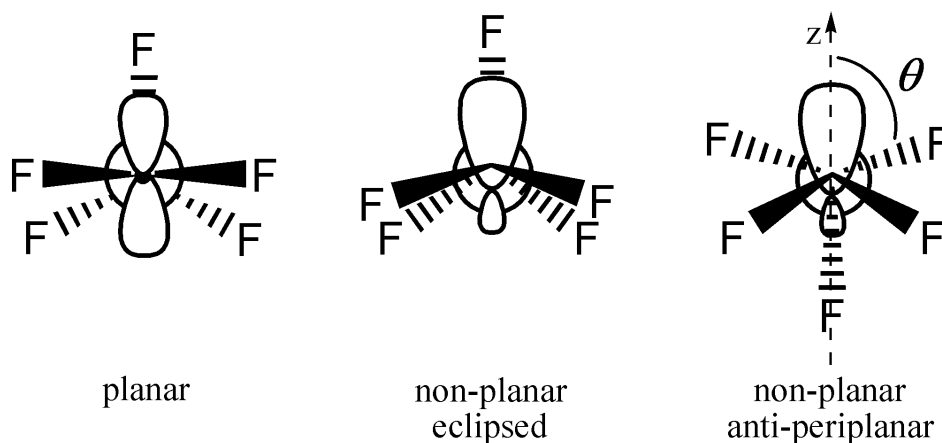


Fig. 44: Possible conformations of the fluorinated ethyl radical.

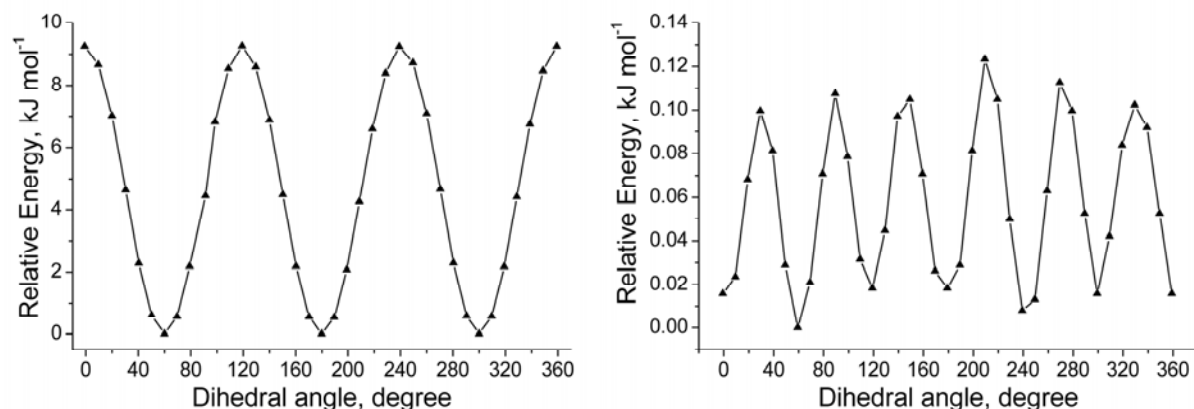


Fig. 45: Relative energies as a function of the dihedral angle θ for optimized (left) and forced planar (right) $\text{CF}_3\cdot\text{CF}_2$ structures.

6.4 g -Tensors

The g -tensor of $\text{CF}_3\cdot\text{CF}_2$ shows a nearly constant component (see Fig. 46) with a high value near 2.00525 in a direction roughly along the C–C bond and two out-of-phase oscillating components, one of which is near the free electron value ($g_e = 2.0023$). The resulting isotropic value is nearly independent of the rotation angle θ and adopts a value of 2.0040. The predicted anisotropy of 0.14% is sizable, nearly four times that of the non-fluorinated ethyl radical, and can lead to a line splitting of *ca.* 5 G in X-band ESR spectroscopy, which may be essential for the interpretation of solid state spectra. In many cases the σ character of the orbital containing the unpaired electron is expected to lead to $g < g_e$, which may be offset in the present case by a slight relativistic contribution of F that is a heavier atom than H.

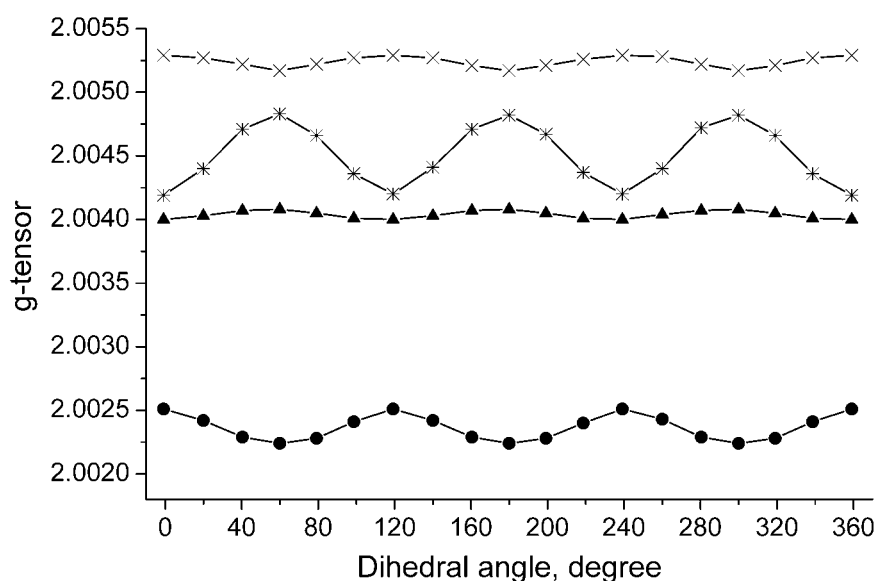


Fig. 46: g -Tensor components and isotropic g -value (▲) as a function of the dihedral angle θ for optimized $\text{CF}_3\cdot\text{CF}_2$.

6.5 Hyperfine couplings

The dependence of the isotropic hfc as a function of the dihedral angle θ is relatively small for the ^{13}C and the F^α and H^α nuclei. For the ethyl radicals it is represented well by an expression:

$$a^i = a_0^i + a_1^i \cos(3\theta + \theta_0) \quad (6-4)$$

These coefficients are given in Table 13 and Table 14. For the β -nuclei the dependence is much more pronounced. It is collated in the form of the coefficients of eqn. (3-31) in Table 15. The behavior of the anisotropic contribution is essential for the present work and is discussed for selected conformations.

^{13}C : The isotropic $^{13}\text{C}^\alpha$ hfc is a sensitive indicator of non-planarity at the radical center. For planar radicals with pure p_z character for the half-occupied orbital one finds values on the order of $\rho_\pi \times 40$ G which arise from spin polarization. Non-planarity contributes s character to this orbital, which enhances the spin density at the nucleus and therefore the coupling constant. This is well known since the work of Fessenden [164] and is verified in Table 13 where this hfc amounts to *ca.* 30 G for the non-fluorinated radicals and 34 G for the planar fluorinated radicals but close to 150 G when non-planarity is admitted so that the geometry is

closer to tetrahedral (the sum of the three bond angles at the radical center amounts to 341° as compared to 329° for a fully tetrahedral and 360° for a planar geometry). The dipolar contribution amounts to *ca.* $-25/-25/+50$ G for all conformations of the fully optimized structure and to *ca.* $-30/-30/+60$ G for forced planar geometries. As expected, the positive component of this axial tensor is directed along the direction of the p_z orbital of the unpaired electron.

The $^{13}\text{C}^\beta$ hfc arises from spin polarization and is therefore negative for the planar geometries (*ca.* -12 G for the nonfluorinated and -18 G for the fluorinated radicals), however, in the non-planar case it changes sign as a consequence of the changing hybridization at C^α and adopts values of *ca.* $+14$ G for the perfluorinated ethyl radical, while it becomes strongly θ dependent, with values between $+27$ G and -1 G, for the perfluoro-1-propyl radical. The dipolar contribution is small, with components ≤ 1 G, but in the non-planar case they increase to about $-2/-2/+4$ G, with the positive component along the C–C bond.

Table 13: Isotropic hfc of $^{13}\text{C}^\alpha$ and $^{13}\text{C}^\beta$ nuclei represented by the coefficients of eqn. (6-4) for the non-fluorinated and fluorinated ethyl radicals.

	a_0 / G		$a_1 / \text{G} (\theta_0 / \text{deg.})$	
	$^{13}\text{C}^\alpha$	$^{13}\text{C}^\beta$	$^{13}\text{C}^\alpha$	$^{13}\text{C}^\beta$
$\text{CH}_3\cdot\text{CH}_2$ (planar)	28.96	-11.85	0.00	0.00
$\text{CH}_3\cdot\text{CH}_2$ (optimized)	29.84^a	-11.74^a	$0.85^a (0)$	$0.11^a (0)$
$\text{CF}_3\cdot\text{CF}_2$ (planar)	34.30	-17.57^a	0.00	$0.05^a (0)$
$\text{CF}_3\cdot\text{CF}_2$ (optimized)	147.63	$+14.38$	$5.28 (-100)$	$1.81 (-130)$

$$^a) a^i = a_0^i + a_1^i \cos(6\theta + \theta_0)$$

F^α and H^α : The isotropic H^α hfc of the non-fluorinated radicals is -22 G. For F^α it becomes θ dependent and oscillates by $\pm 1-3$ G about a value of $+48.5$ G for the planar and $+77$ G for the non-planar structures (Fig. 47, Table 14). Thus, even though the hfc arises from spin polarization it is predicted to be positive for F, also in the planar case. For the non-planar case it was demonstrated long ago in the beautiful work by Fessenden [164] who suggested that even the H^α hfc of $\cdot\text{CHF}_2$ may be positive.

For the non-fluorinated radical the dipolar contribution to the H^α hfc tensor is of planar symmetry and amounts to *ca.* $-14/0/+14$ G with the positive component along the C–H bond. For the planar fluorinated radicals it rises to spectacular near axial $-85/-70/+155$ G, surprisingly with the positive component pointing parallel to the p_z orbital. There is a slight oscillation of the latter values by *ca.* ± 2 G for the different conformations. For the non-planar fluorinated radicals we calculate $-79/-71/+150$ G with very little variation for the different conformations or additional CF_3 substitution (Fig. 48). This means that the effective hfc (the sum of isotropic plus dipolar contributions) can vary in a rigid system, depending on orientation with respect to the applied magnetic field, between nearly zero and +227 G, which is not unexpected but can pose a challenge for the observation and assignment of experimental spectra.

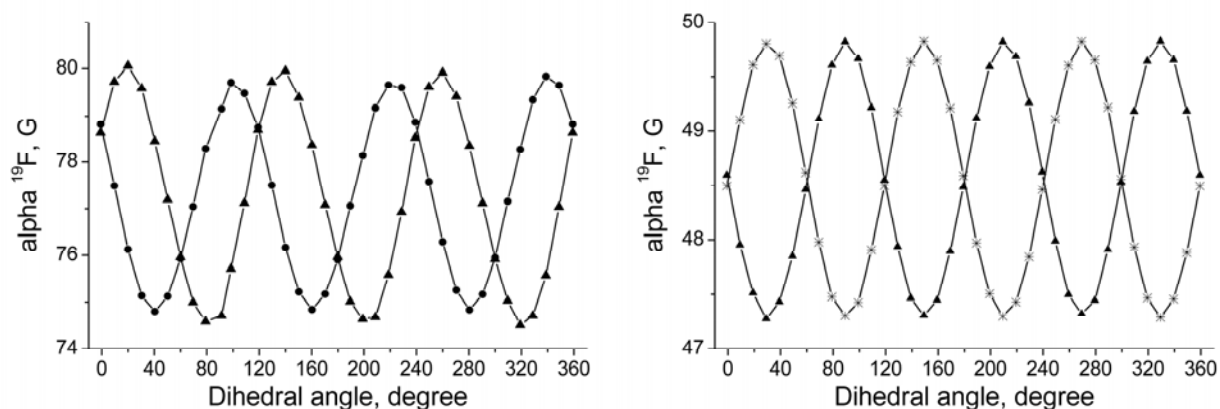


Fig. 47: F^α hfc as a function of the dihedral angle θ for optimized (left) and forced planar (right) $CF_3\bullet CF_2$ structures.

Table 14: Isotropic hfc of H^α and F^α nuclei represented by the coefficients of eqn. (6-4) for the non-fluorinated and fluorinated ethyl radicals.

	a_0 / G		$a_1 / G (\theta_0 / \text{deg.})$	
	$^1H^\alpha$	$^{19}F^\alpha$	$^1H^\alpha$	$^{19}F^\alpha$
$CH_3\bullet CH_2$ (planar)	-22.06	–	0.34 (–90)	–
$CH_3\bullet CH_2$ (optimized)	-21.82 ^a	–	0.37 ^a (–90)	–
$CF_3\bullet CF_2$ (planar)	–	+48.55	–	1.26 (–90)
$CF_3\bullet CF_2$ (optimized)	–	+77.23	–	2.73 (–60)

^a) $a^i = a_0^i + a_1^i \cos(3\theta + \theta_0) + a_2^i \cos(6\theta)$, $a_2 = 0.22$ G

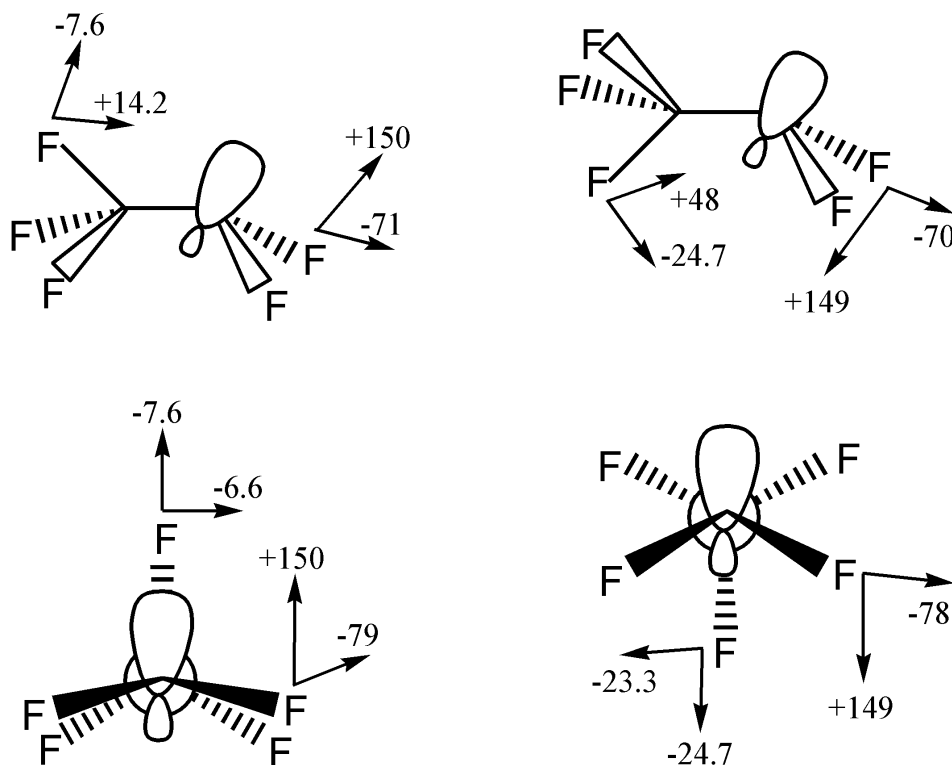


Fig. 48: Anisotropic spin-dipole couplings and directions of the dipolar contribution to the ^{19}F hyperfine tensor for optimized $\text{CF}_3\cdot\text{CF}_2$ structure in eclipsed (left) and anti-periplanar (right) conformations.

F^β and H^β : The isotropic hfc's of β -nuclei of $\text{CH}_3\cdot\text{CH}_2$ and planar $\text{CF}_3\cdot\text{CF}_2$ are both ideal representations of the McConnell relation. In the form of eqn. (3-31) a_0^β is close to and c^β equal to zero, while b^β amounts to 56 G for the nonfluorinated and 70 G for the fluorinated species (Fig. 49, Table 15). Surprisingly, b^β increases to 106 G for planar $\text{CF}_3\text{CF}_2\cdot\text{CF}_2$ while it remains essentially unchanged for the non-fluorinated analogue. Non-planarity at the radical center leads to an expected non-zero c^β , but the total variation of a^β reduces to 35 G for $\text{CF}_3\cdot\text{CF}_2$ and to 44 G for $\text{CF}_3\text{CF}_2\cdot\text{CF}_2$, with the largest value in the anti-periplanar conformation ($\theta = 180^\circ$). Thus, non-planarity leads to a net increase of the isotropic hfc at F^α , but a decrease at F^β .

Since the dipolar contribution scales with the inverse cube distance, $\langle r^{-3} \rangle$, of the nucleus from the unpaired electron it is expected to be much smaller for β - than for α -nuclei. In agreement with expectation we find near axial values with a dominant positive contribution of *ca.* 3.2 G for the non-fluorinated radicals. However, the situation becomes quite dramatic for the planar fluorinated species. The tensor is also axial, but the dominant positive contribution has increased to 56 G for F^β in the eclipsed or anti-periplanar conformation and still 22 G for

F at θ of 120° . In the fully optimized non-planar case the positive dipolar hfc component of F^β is still 48 G in the anti-periplanar position (5 G for the atoms at 120°), but this decreases to 14 G in the eclipsed position while it increases to 22 G at 120° . In the planar *n*-propyl radical the positive dipolar component of the eclipsed F^β increases even further to *ca.* 71 G . Since the nuclear moment of F is even slightly less than that of H and the distance of these β -nuclei cannot be greatly different, the spectacular increase by a factor of 20 and more cannot be explained by a purely dipolar interaction but must reflect large spin polarization which leads to a significant change in the spin distribution.

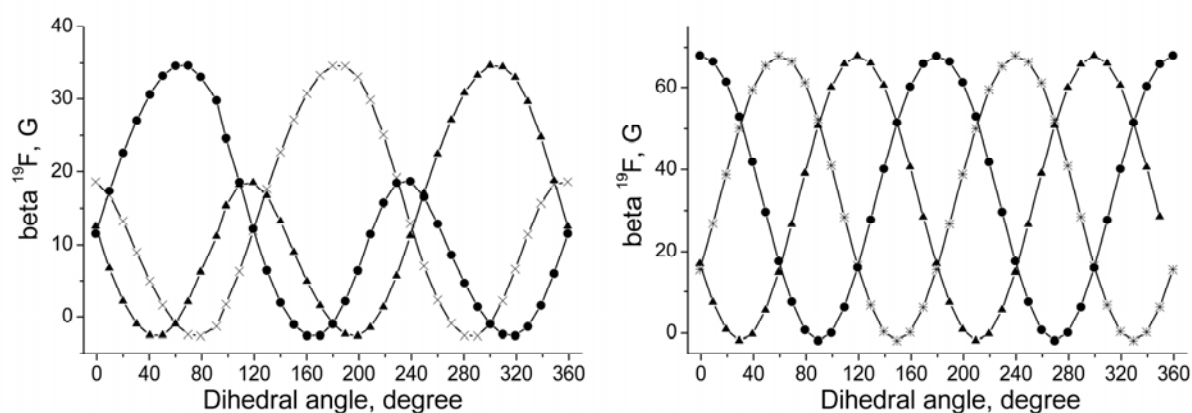


Fig. 49: F^β hfc as a function of the dihedral angle θ for optimized (left) and planar (right) $\text{CF}_3\cdot\text{CF}_2$ structures.

$^{13}\text{C}^\gamma$: This nucleus is located two bonds from the radical center and behaves therefore in an analogous way as F^β and H^β , with a strong dependence of the isotropic hfc on the dihedral angle θ . This is verified in Table 16 where it is seen that the *b* coefficients are a factor of 2 lower than those for H^β . Based on the $^1\text{H}/^{13}\text{C}$ relative magnetic moments one should have expected a factor of 4, so there is some spin polarization involved. The dipolar contributions amount to little more than 1 G at maximum.

Table 15: Isotropic hfc of H^β and F^β nuclei represented by the coefficients of eqn. (3-31) for the non-fluorinated and fluorinated ethyl and 1-propyl radicals (rotation is about the $C^\alpha-C^\beta$ bond).

	a_0 / G	$b / G (\theta_0 / \text{deg.})$	$c / G (\theta_0' / \text{deg.})$
$CH_3^\bullet CH_2$ (planar)	+0.16	55.79 (+60)	0.0
$CH_3^\bullet CH_2$ (optimized)	-0.30	56.59 (+60)	0.0
$CF_3^\bullet CF_2$ (planar)	-1.60	70.02 (+60)	0.0
$CF_3^\bullet CF_2$ (optimized)	-1.25	27.47 (+60)	8.21 (+60)
$CH_3CH_2^\bullet CH_2$ (optimized)	-0.28	53.07 (+60)	0.0
$CF_3CF_2^\bullet CF_2$ (planar)	-1.11	105.90 (+80)	0.0
$CF_3CF_2^\bullet CF_2$ (optimized)	-1.69	44.88 (+70)	1.39 (+80)

Table 16: Isotropic hfc of $^{13}C^\gamma$ nucleus represented by the coefficients of eqn. (3-31) for the non-fluorinated and fluorinated 1-propyl radicals (rotation is about the $C^\alpha-C^\beta$ bond).

	a_0 / G	$b / G (\theta_0 / \text{deg.})$	$c / G (\theta_0' / \text{deg.})$
$CH_3CH_2^\bullet CH_2$ (optimized)	-0.22	33.11 (-60)	0.0
$CF_3CF_2^\bullet CF_2$ (planar)	-1.37	20.41 (-60)	0.0
$CF_3CF_2^\bullet CF_2$ (optimized)	-0.48	9.86 (-60)	6.33 (-60)

H^γ and F^γ : These nuclei are at a distance three bonds away from the radical center. In a suitable conformation for the planar structures in which the $H^\gamma(F^\gamma)-C^\gamma-C^\beta-C^\alpha-p_z$ -orbital are arranged in a zig-zag (“W”) conformation (the dihedral $\angle H^\gamma(F^\gamma)-C^\gamma-C^\beta-C^\alpha = +180^\circ$ in our case) the isotropic hfcs nevertheless vary with the rotation angle about the $C^\alpha-C^\beta$ bond with an amplitude of 6.0 G for the non-fluorinated and 15.0 G for the planar perfluoro-1-propyl radicals (Table 17). Also the positive dipolar contributions can be *ca.* 2.3 G for the non-fluorinated and up to 7 G for the fluorinated species. It has been known for a long time that a

perfect “W”-plan arrangement of the bonds between the γ -proton and the reference p_z orbital for n -propyl radical is actually realized when the dihedral angle between the $\bullet\text{CC}^\alpha\text{C}^\beta$ and $\text{C}^\alpha\text{C}^\beta\text{C}^\gamma$ planes equals $\pm 180^\circ$ [165]. This situation is often supposed to be responsible for strong long-range interactions. In such a conformation, one gets an additive effect of delocalization and spin polarization, which is particularly large because these two contributions are maximum and positive at the same time. They result in a strong positive hyperfine splitting (+4.37 G) for H^γ in the “W” conformation [165]. Furthermore, the largest spin density is not found for the γ -position closest to the radical site [165].

Table 17: Isotropic hfc of F^γ (H^γ) nuclei represented by the coefficients of eqn. (3-31) for the non-fluorinated and fluorinated 1-propyl radicals ^{a)}.

	a_0 / G	$b / \text{G} (\theta_0 / \text{deg.})$	$c / \text{G} (\theta_0' / \text{deg.})$
$\text{CH}_3\text{CH}_2\bullet\text{CH}_2$ (optimized)	-0.85	6.42 (-60)	0.0
$\text{CF}_3\text{CF}_2\bullet\text{CF}_2$ (planar)	-0.84	14.97 (-60)	0.0
$\text{CF}_3\text{CF}_2\bullet\text{CF}_2$ (optimized)	+1.66	5.79 (-60)	7.55 (-60)

^{a)} eqn. (3-31) is valid for the γ -atom in the zig-zag (“W”) conformation.

6.6 Further discussions

Based on the BDEs for the primary, secondary, and tertiary peroxy radicals and peroxide molecules we can assume that a detachment of molecular oxygen, favored by the gain of entropy, is the most likely process of peroxy to alkyl radical conversion for both FEP and PE. The detachment of atomic oxygen is unlikely. Peroxy radicals are unlikely to abstract F from C–F bonds, but H abstraction may compete with oxygen detachment to some extent. For alkoxy radicals abstraction of H but not F atoms is thermodynamically favorable. In general, fluorine substitution leads to interesting charge polarization effects.

The hybridization about the radical center in the non-fluorinated ethyl radical is believed to be of sp^2 type, and, hence planar or nearly planar. Both experimental observations and ab initio calculations show that at very low temperatures the methyl group is distorted with non-equivalent β C–H bonds, and that the C–H bonds on the radical center are ethylene-type C–H

bonds [166]. Therefore non-planar radicals may be reasonable because this structure decreases the repulsions between C–H bonds located on the radical center and on the methyl group. The present DFT calculations do not provide clear evidence for deviations from planarity for the optimized non-fluorinated ethyl radical, for which the sum of the three bond angles at the radical center is 359.5° , although there are some slight deviations in the isotropic hfc's of the ^{13}C and ^1H nuclei between the optimized and the forced planar $\text{CH}_3\cdot\text{CH}_2$ structures. In contrast, the optimized fluorinated ethyl radical is non-planar, so that the geometry is closer to tetrahedral (the sum of the three bond angles at the radical center amounts to 341° as compared to 329° for a fully tetrahedral and 360° for a planar geometry). Both the optimized non-fluorinated and the forced planar fluorinated ethyl radicals exhibit a small six-fold potential on the order of $0.1\text{--}0.2\text{ kJ mol}^{-1}$ for the internal rotation about the $\text{C}^\alpha\text{--C}^\beta$ bond, while for the forced planar $\text{CH}_3\cdot\text{CH}_2$ radical the very small difference (0.03 kJ mol^{-1}) confirms the earlier conclusion that the two groups of C_{2v} and C_{3v} symmetries attached to the same single bond lead practically to a zero sixfold rotation barrier [165].

It has long been recognized that ^{13}C hyperfine splittings can yield important information concerning the electronic and geometrical structure of hydrocarbon radicals. The usefulness of the ^{13}C splitting is a result of the direct introduction, upon a departure from planarity, of s character into the orbital containing the unpaired electron, together with the large potential splitting by ^{13}C of the order of 300 G for an electron in an sp^3 hybrid orbital [167]. The splitting at the α -position in the non-fluorinated ethyl radical (39.07 G) is very similar to that in methyl, thus suggesting planar configuration, while the large (105.77 G) splitting, for instance in the vinyl radical reflects the hybrid nature of the electron containing orbital [164]. In interpreting ESR data, knowledge of the exact geometrical structure of the radical under consideration is very important, out-of-plane deviations at the radical site often being taken as responsible for the observed changes in the splittings. The direct contribution of conformational effects for the non-fluorinated ethyl radical is zero or near zero as a consequence of the local antisymmetry property of the half-occupied orbital at the planar radical site. Thus, the coupling arises from spin polarization essentially and the performed density functional calculations give a value of *ca.* 30 G , somehow smaller than the experimentally observed (39.07 G) [164]. The calculated $^{13}\text{C}^\beta$ hfc arises from spin polarization and is therefore negative for the planar geometries (*ca.* -12 G for the nonfluorinated and -18 G for the fluorinated radicals). It is again slightly smaller than the experimentally observed of 13.57 G for the $\text{CH}_3\cdot\text{CH}_2$ [164] radical, but in a good agreement

with the average coupling of 11.8 G (assuming free rotation about the $\bullet\text{C}-\text{C}^\alpha$ bond) given by Ellinger et al. [165]

On the contrary, both delocalization and spin polarization are very sensitive to deviations from planarity at the radical site. Thus the isotropic $^{13}\text{C}^\alpha$ coupling is close to 150 G for the optimized $\text{CF}_3\bullet\text{CF}_2$, which is non-planar as discussed above, while the $^{13}\text{C}^\beta$ hfc changes sign as a consequence of the changing hybridization at C^α and adopts values of *ca.* +14 G for the perfluorinated ethyl radical.

It should be noted that the basic features of the theory of the ^{13}C hyperfine splitting have been proven correct by the existence of radicals in which large ^{13}C splittings are observed owing to a large degree of bending and the consequent large *s* character to the orbital containing the unpaired electron. The clearest examples are $\bullet\text{CF}_3$ ($a_{\text{C}} = 271.6$ G), $\bullet\text{CHF}_2$ ($a_{\text{C}} = 148.8$ G), $\bullet\text{CH}_2\text{F}$ ($a_{\text{C}} = 54.8$ G). This trend can be explained by an increasing non-planarity with increasing fluorine substitution. For $\bullet\text{CF}_3$, at least, there can be little tendency for bent bonds because the value of a_{C} is close to the maximum possible for a tetrahedral radical. Furthermore, substitution of CF_3 for CH_3 might be expected to tip the energy balance enough to cause a relatively large change in conformation.

At room temperature the α -proton couplings in π electron radicals $-\text{CH}^\beta\bullet\text{CH}^\alpha$ tend to vary little from matrix to matrix and change little with temperature. The calculated isotropic H^α hfc of the non-fluorinated radicals is -22 G, in a good agreement with literature (-22.38 G for the ethyl and -22.11 G for the isopropyl radicals) [168]. For F^α it becomes θ dependent and oscillates by $\pm 1-3$ G about a value of $+48.5$ G for the planar and $+77$ G for the non-planar structures. Thus, even though the hfc arises from spin polarization it is predicted to be positive for F, also in the planar case. This in agreement with literature, as even for the $\bullet\text{CHF}_2$ radical mentioned above, the H^α hfc was determined to be positive ($+22.2$ G). Our density functional calculations give a H^α hfc of $+21.93$ G for the $\bullet\text{CHF}_2$ radical.

For the planar fluorinated radicals the calculated dipolar contribution to the F^α hfc tensor amounts to spectacular near axial $-85/-70/+155$ G, surprisingly with the positive component pointing parallel to the p_z orbital. This may mean that some of the unpaired electron delocalizes onto F^α . Comparing $\text{C}^\alpha-\text{F}^\alpha$ (*ca.* 1.314 Å) and $\text{C}^\beta-\text{F}^\beta$ (1.361 Å) bond lengths supports such a suggestion, as it shows that there is some spin distribution on the F^α nuclei. The spin density is localized mostly at the C^α atom (*ca.* 83%), but there is also *ca.* 6% spin density at each F^α atom (Fig. 50). Taking into account the extremely large isotropic hyperfine

constant for the ^{19}F -nuclide, such as 18865.3 G [100], such a variation for the effective hfc of the F-nuclei may be expected.

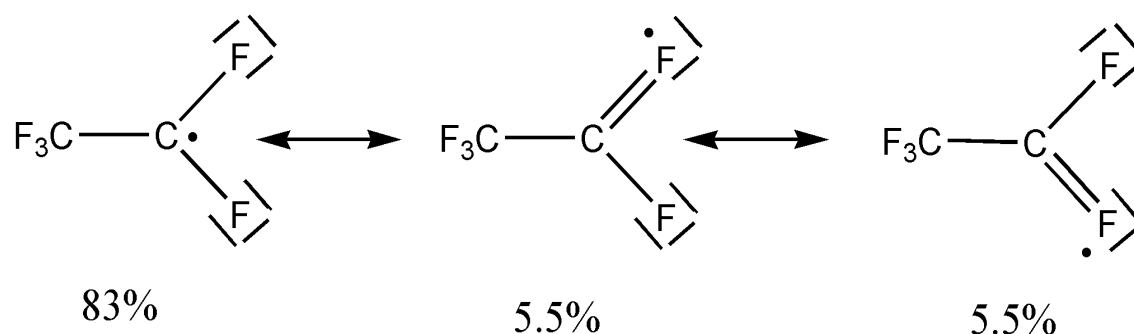


Fig. 50: Spin density distribution for the fluorinated ethyl radical.

The β -proton splittings are nearly isotropic but vary considerably from radical to radical and sometimes show a temperature dependence, the reason for this being the restricted motion about the $\text{C}^\alpha\text{-C}^\beta$ axis [169]. The isotropic hfc's of the β -nuclei of $\text{CH}_3\cdot\text{CH}_2$ and planar $\text{CF}_3\cdot\text{CF}_2$ radicals are both ideal representations of the McConnell relation. Assuming non-planarity at the radical center leads to a net increase of the calculated isotropic hfc at F^α , but a decrease at F^β . The β -coupling constants in cases where they have been rotationally averaged isotropically are found to decrease with increasing substitution of alkyl groups on the C^α atom [170]. For the non-fluorinated ethyl radical a value of 26.87 G for the freely rotating methyl group was obtained [170,171]. Our calculated values for a_0 and b^β terms in the McConnell relation for the $\text{CH}_3\cdot\text{CH}_2$ radical are in a good agreement with the quoted values of 1.5 G and 50 G, respectively [171].

Since the dipolar contribution scales with the inverse cube distance, $\langle r^{-3} \rangle$, of the nucleus from the unpaired electron it is expected to be much smaller for β - than for α -nuclei. The situation is quite dramatic for the planar fluorinated species suggesting large spin polarization which leads to a significant change in the spin distribution, as mentioned before. In general, the transfer of spin densities to the β -protons is a subject of much speculation, as it can be interpreted either by the delocalization of the unpaired electron or by a mechanism of spin polarization, depending whether we have planar or non-planar radicals.

In small fluorinated fragments typical values for $a_{\text{iso}}(\text{F})$ are large, in the range 60-150 G for α -fluorine and 20-70 G for β -fluorine [172]. The isotropic F^α hfc in the $\cdot\text{CF}_3$ radical has a value of 144.75 G, which is considerably larger than other known values for α -fluorine atoms,

for instance in $\bullet\text{CHF}_2$ (84.2 G) and $\bullet\text{CH}_2\text{F}$ (64.3 G) radicals [98]. However, the $\bullet\text{CF}_3$ radical comes close to maintaining tetrahedral geometry where the sp^3 hybridization would give 25% s character to the orbital [98]. Fluorine hyperfine splittings for the end-chain radical $-\text{CF}_2\bullet\text{CF}_2$ in γ -irradiated PTFE were quoted: 170 G for F^α and 16 G for F^β [173]. The primary perfluoroalkyl radical $\text{R}_f\text{CF}_2\bullet\text{CF}_2$ was also identified in the work of Faucitano et al. and the determined isotropic hfcs were 87.3 G ($2F^\alpha$) and 13.0 G ($2F^\beta$) [174]. The principal values of the g - and ^{19}F hyperfine tensors for the end-chain radical $\text{ROCF}_2\bullet\text{CF}_2$ (formed by UV irradiation of Nafion[®] and Dow[®] perfluorinated membranes) were determined, obtained by simulation of the ESR spectrum from the $\text{ROCF}_2\bullet\text{CF}_2$ radical and compared with the corresponding values for the propagating end-chain radical in PTFE or perfluorinated polyethers [175]. Thus the obtained anisotropic spin-dipole couplings for the F^α nuclei are (+136, -68 and -68 G), the isotropic splitting being 86 G [175]. The dipolar contributions for the F^β nuclei are (-5, +3 and +3 G), $a_{\text{iso}} = 35$ G [175]. For the $\bullet\text{CF}_2\text{CONH}_2$ radical in irradiated trifluoroacetamide the principal values of the anisotropic part of the hyperfine splitting tensor for the α -fluorines are (+107.5, -49.0 and -58.5 G) at 300 K, but they change to (+127, -57 and -69 G) at 77 K with an accompanying increase in the isotropic component from 72.5 to 75.3 G [176]. Furthermore the principal tensor components and direction cosines for α , β_1 and β_2 -fluorine interactions for the $\text{CO}_2^-\text{CF}_2\bullet\text{CFCO}_2^-$ radical at 77 K were determined, the isotropic F^α hyperfine interaction being *ca.* 75 G, while the isotropic hyperfine interactions as well the principal values were considerably different for the two F^β nuclei (+122, +41 and +41 G) for $F^{\beta 1}$, $a_{\text{iso}} = 68$ G and (+9, -3 and -2 G) for $F^{\beta 2}$, $a_{\text{iso}} = 1.4$ G [172]. Thus, where comparable experimental or theoretical literature data are available, the performed DFT calculations are in a relatively good agreement for the isotropic hfcs, while for the anisotropic spin-dipole couplings there are large variations depending strongly on the different systems being investigated, as well as on the different theoretical treatment of these systems.

In addition the equilibrium conformations in alkyl radicals are determined by a delicate balance between steric repulsions and the optimization of $\text{C}^\beta\text{-H}^\beta$ hyperconjugation effects. There is little evidence that C-C hyperconjugation plays a significant role in determining the geometry, in contrast to the conclusions reached for alkyl cations [171]. However, with alkyl radicals substituted in the β -position with heteroatoms such as S, Si, Ge, and ^{99}Sn the C-X hyperconjugation geometry with the heteroatom eclipsed by the p orbital on the radical center

generally prevails, indicating a measure of d orbital participation in the electronic structure of these radicals [171].

The coupling constants for protons lying more remote from the radical center, for instance γ -protons, have also received some attention. In alkyl radicals, where the spin density ρ_π on C^α is generally taken as unity, H^α and H^β protons exhibit large hyperfine splittings, whereas γ -protons are weakly coupled in most cases. However, there are exceptions to this rule, for example strong long-range interactions ascribed to a “W”-plan arrangement of the bonds between the γ -proton and the p orbital containing the unpaired electron [165] and this situation is also confirmed from the performed DFT calculations, as discussed before.

The calculated isotropic g -values of the $CH_3^\bullet CH_2$ and $CF_3^\bullet CF_2$ radicals, 2.0027 and 2.0040 respectively, are in a good agreement with the literature data for the non-fluorinated and fluorinated ethyl and propyl radicals [177].

Chapter 7

7 SUMMARY

The present work consists of three parts which deal with the optimization of the properties of polymers finding application as proton exchange membranes in PEMFCs. The focus is the oxidative and photochemical stability of non-fluorinated polymer membranes, as well as the radiation-induced grafting of commercially available fluoropolymer films. The use of the ESR technique is common for the first two parts of the dissertation. ESR spectroscopy is the major method of study, because of its sensitivity and specificity for the detection of radical intermediates. It is a suitable spectroscopic technique to identify the nature of radiation generated radicals in organic polymers, and to monitor their concentration *in-situ* during the grafting process. The third part comprises the results and discussions of DFT calculations for non-fluorinated and fluorinated fragments.

Oxidative degradation of polymers is usually a free radical process which involves attack of the hydroxyl and hydroperoxyl radicals, HO^\bullet and HOO^\bullet . Both radicals are intermediates of the oxygen reduction in a fuel cell process, and since hydrogen peroxide has been detected as a trace by-product of the fuel cell reaction it is plausibly assumed that attack of these two radicals is an important degradation pathway of the proton conducting polymer membrane. The focus of the first part of the present dissertation are the reaction mechanisms which are accessible *via* the structures of free radical intermediates, and the identification of fuel cell operating conditions which may lead to enhanced free radical production. Therefore the ESR approach is a natural choice for such studies. In order to predict hydroxyl radical initiated degradation of new proton conducting polymer membranes based on sulfonated polyetherketones and polysulfones, five non-fluorinated aromatics are chosen as model compounds for ESR experiments, aiming at the identification of products of HO^\bullet radical reactions with these monomers. Direct photolysis of aqueous solutions of H_2O_2 was chosen as the source of HO^\bullet radicals. In order to distinguish HO^\bullet radical attack from direct photolysis of the monomers, experiments were carried out in the presence and absence of H_2O_2 . A detailed investigation of the pH dependence was carried out for 4,4'-sulfonyldiphenol (SDP), bisphenol A (BPA) and 4,4'-diphenol (DP). 4,4'-dihydroxybenzophenone (HBP) and

sulfonated 4,4'-dichlorodiphenylsulfone were also investigated aiming at a comparison with the above monomeric building blocks.

It is remarkable that the maximum formation of phenoxyl radicals from BPA and SDP occurs in the pH range close to the pK_S of the HO^\bullet radicals (11.9) and of H_2O_2 (11.7). This has been shown to be due to the rates of formation of $\text{O}_2^{\bullet-}$ and of $^1\text{O}_2$ which are proportional to the products of the rate constants and the pH dependent concentrations of the reactants [47]. Moreover, $\text{O}^{\bullet-}$ and $\text{O}_2^{\bullet-}$ are radicals with nucleophilic nature that leads to H-abstraction from phenolic OH-substituents, thus producing the primary phenoxyl radicals. The $\text{O}_2^{\bullet-}$ radical, in contrast to its protonated form (HOO^\bullet , pK_S 4.8), can also attach directly to the aromatic ring and hence must be considered as an intermediate to phenoxyl radical formation. On this basis reaction mechanisms are suggested. Alternatively, radicals may be formed by reaction with oxygen, which is most probably of a singlet character since $^3\text{O}_2$ would lead to an extensive spin exchange and thus to the loss of hyperfine structure in the ESR spectra, in contrast to our observations. Thus, the addition of $^1\text{O}_2$ directly to the aromatic ring leads to the formation of the observed dioxysubstituted radicals at basic conditions. Since both H_2O_2 and HO^\bullet deprotonate near pH 11.7, the new reactive species is $\text{O}^{\bullet-}$ which can abstract H-atoms but shows little tendency for addition, but in particular, $\text{O}_2^{\bullet-}$ or $^1\text{O}_2$ are formed which are held mainly responsible for the formation of phenoxyl and semiquinone-type aromatic polyoxy radicals, observed at $\text{pH} \geq 11.7$ in the experimental ESR spectra. A large number of new radicals give evidence of multiple hydroxylation of the aromatic rings. For fuel cells with polymer-membrane electrolytes this means that high pH values, which may occur under conditions of fuel starvation and large inhomogeneities, are very damaging and lead to rapid degradation of the membrane.

Strongly deactivating substituents such as SO_3^- and SO_2 which exert a $-I/-M$ effect direct nucleophilic substitution to the *meta* position. An oxy substituent which is strongly activating, with a $+I/+M$ effect, favors further substitution at *ortho* and *para* positions. It is known that the sulfone group has a deactivating role. Thus, in comparison with the other monomeric building blocks, SDP has an advantage in terms of chemical stability towards HO^\bullet addition. Furthermore, blocking of the aromatic ring by suitable substitution, for example by fluorine, limits the HO^\bullet addition reactions. SO_3^- substituents are introduced to give rise to proton conductivity, but as an additional benefit they reduce the activity of the aromatic ring towards hydroxyl radical addition.

It is shown that also direct photolysis of the monomers leads to semiquinone type radicals. For SDP, BPA and HBP this involves cleavage of a C–C bond to give *p*-benzosemiquinone

radical anions, whereas DP does not cleave but photo-oxidizes to give the *p*-diphenobenzosemiquinone radical anion. At $\text{pH} < 10$, H_2O_2 is photolyzed to give HO^\bullet radicals which react more readily with the methanol solvent than with the substrate. The hydroxymethyl radical intermediate can, however, be trapped by spin-trap molecules (3,5-dibromo-4-nitrosobenzene-sulfonic acid in our case). Under acidic or neutral conditions no radicals are observed. It is expected that the dominating reaction is addition of HO^\bullet to the aromatic ring, preferentially in the *ortho* position to alkyl- and RO-substituents (since in sulfonated PEK the *para* position is substituted and thus blocked) [47]. The fact that no radicals are observed leads to the conclusion that the lifetime of these radicals (if formed) should be very short so that their concentration is too low, or the signals too broad or split into too many lines so that their signal is below the limit of ESR detection. The present study focuses on the case in which $\text{O}_2^{\bullet-}$ or $^1\text{O}_2$ are the damaging species above $\text{pH} 11.7$, and in which the dominating reaction is that with the aromatic ring.

In the second part of the present work three different electron beam irradiated fluoropolymers - poly(ethylene-alt-tetrafluoroethylene) (ETFE), poly(tetrafluoroethylene-co-hexafluoropropylene) (FEP) and poly(vinylidene fluoride) (PVDF), as well as their grafting reactions with styrene, 25% styrene in benzene and 25% styrene in ethanol are investigated by means of ESR. In spite of earlier investigations performed with fluoropolymers, many gaps still exist however in the current knowledge and data. For instance even the most basic information concerning molecular weight, crystallinity or orientation is not always known about the FEP, ETFE and PVDF materials that have been studied. A clear overall understanding is not possible because a variety of different irradiation sources and doses have been used. Therefore, the relative rates of radical decay are not known for the same polymer type but irradiated under air versus inert atmosphere, nor has the radiation grafting of different polymers irradiated in the same manner and with the same dose been compared. There is also no general agreement as to the radical species formed upon irradiation of FEP and PVDF, and comparatively little work has been published on the radicals generated in ETFE upon irradiation, especially under conditions similar to those used in the radiation grafting method for preparing membranes. Also no ESR investigations appear to have been carried out to-date on PVDF films irradiated with electron beam and using doses of relevance for the radiation grafting method (< 100 kGy).

The present research work addresses these various gaps in the literature. Firstly, it was possible to compare the radiation chemistry of the three fluoropolymers that have been irradiated using the same irradiation source, doses and atmospheres. Secondly, it was possible

to compare the decay of radicals in the different fluoropolymers by carrying out *in-situ* ESR measurements in a similar systematic manner during the radiation grafting process, aiming at an understanding of the influence of the irradiation atmosphere and of the diluent. In addition, this investigation focuses on studying the radiation chemistry of the fluoropolymer types most typically used in the radiation grafting method and the most industrially attractive irradiation method, namely the electron beam.

In the experimental ESR spectra obtained with ETFE electron irradiated under inert atmosphere and measured at +60 °C a secondary radical resulting from C–H bond scission is the majority species. In the ESR spectra obtained with FEP electron irradiated under Ar and measured at +60 °C primary, secondary and tertiary radicals (resulting from C–C and C–F bond scissions) are identified, the primary being the predominant ones. In the experimental ESR spectrum obtained with PVDF electron irradiated under Ar and measured at –120 °C we already have a fine structure and it is not better resolved by further heating to +60 °C, suggesting a high mobility of the polymer chains already at –120 °C. The spin concentration values for ETFE are always a factor of two higher than the corresponding values for FEP for both irradiation atmospheres. Under air the radical yield is reduced by a factor of two for both ETFE and PVDF polymer films, but not for FEP. This may be related to the high oxygen solubility in perfluorinated media. The higher spin concentration values for ETFE may be used for the production of membranes with higher grafting levels and thus resulting higher ion exchange capacities.

The grafting reactions with ETFE electron irradiated under air are expected to proceed over alkyl radicals, which have been previously formed by hydrogen abstraction by the peroxy groups in the swollen regions of the polymer. The resulting curves for radical decay of ETFE and FEP polymer films electron irradiated at 40 kGy fit to a mono exponential function (except when benzene is used as a diluent for the peroxy radicals). This gives rate constants which allow direct comparison of the grafting reactions under different experimental conditions. For FEP irradiated under Ar the decay of the radical signal in styrene diluted with benzene is nearly four times faster (although the benzene concentration is a factor of four lower) than with pure styrene. For samples irradiated under air, the rate is accelerated by as much as a factor of ten by the benzene diluent. ETFE showed the same trends, but with somewhat lower enhancement factors. Therefore this may be taken as an evidence of successful swelling. However, it has to be taken into account that benzene may also react with the radical centers on the backbone chain. For a concentration of 25% styrene in benzene such

a radical transfer may reduce the above enhancement by as much as a factor of four. Dilution by ethanol does not increase the grafting rate.

The grafting levels for FEP are between 30% and 80% lower than those for ETFE on weight basis. The effect gets less pronounced if considered per grafted backbone $\text{CF}_2(\text{CH}_2)$ unit. It is concluded that the crystallinity and molar mass have a pronounced effect for PVDF, whereby the monomer transport into the film and the extent of radical formation, as well as the compatibility with the graft component are the limiting factors for FEP and ETFE. The use of diluent reduces the grafting levels compared to pure styrene for both ETFE, FEP and PVDF irradiated under air or Ar. An interesting observation is that grafting reactions under inert atmosphere at +60 °C lead to the formation of longer polymer chains, while reactions under air at the same temperature result in short polymer chains.

For practical applications proton exchange membranes have to fulfill a variety of different and sometimes conflicting demands, like high mechanical stability at various relative humidity and temperature, high overall proton conductivity, wide range of operating temperatures from sub-zero up to +90 °C and above. By variation of the oxygen concentration during irradiation and the reaction temperature during grafting advantage can be taken to influence the grafting chain length and the degree of cross-linking and therefore the swelling behavior and the mobility of the functional groups in the membrane. This affects the sub-zero membrane conductivity and the water retention within the membrane. Radiation grafting seems to offer some flexibility to influence these specifications at a comparably early stage of membrane manufacturing. The results described above are of importance to optimize the various parameters influencing the radiation grafting process.

Furthermore, in the radiation grafting of polymer films with styrene for fuel cell applications it is important to control whether the polystyrene chain is grafted onto a peroxy or a carbon centered radical, because of the different bond strengths which prevent the grafted chain to cleave off. Thus thermodynamic properties of small alkyl and alkyl-peroxy radicals are studied to model primary, secondary and tertiary radicals in non-fluorinated and perfluorinated polymers and a comparative DFT study is conducted. A B3LYP hybrid functional and a 6-311+G** basic set were used as implemented in Gaussian 98. Based on the calculated bond dissociation energies a detachment of molecular oxygen, favored by the gain of entropy, is the most likely process of peroxy to alkyl radical conversion for both FEP and PE. The detachment of atomic oxygen is unlikely. Peroxy radicals are unlikely to abstract F from C–F bonds, but H abstraction may compete with oxygen detachment to some extent. For alkoxy radicals abstraction of H but not F atoms is thermodynamically favorable. In general,

the performed DFT calculations show that F can induce strong and sometimes counter-intuitive charge polarization in molecules.

Geometry and charge distribution of the secondary and tertiary peroxy radicals are fully or nearly symmetric on reflection at the radical center. The C–C backbone of these structures represents to a good approximation an all-trans conformation. This holds also for the secondary non-fluorinated alkyl radical, but the symmetry is slightly broken for the optimized structures of the secondary fluorinated and the tertiary non-fluorinated and fluorinated alkyl radicals in which we find gauche elements. More interesting is the slight C–C bond length inequivalence and in particular the charge polarization, amounting up to nearly $0.4 e$, that results from the broken symmetry. It is known that C–F bonds are rather susceptible to stereoelectronic effects and for the present fluorinated alkyl radicals it could mean that they possess quite a different chemical reactivity from the all-trans than from the gauche conformation.

Furthermore, it is shown based on DFT calculations that pronounced spin polarization effects lead to unexpected behavior of the hyperfine anisotropy. This is demonstrated by comparison of the parameters of $\text{CF}_3\cdot\text{CF}_2$, both in its fully optimized non-planar and in a forced planar conformation, with those of the analogous non-fluorinated and essentially planar $\text{CH}_3\cdot\text{CH}_2$ radical. The study is extended briefly to the fluorinated and the non-fluorinated 1-propyl radicals. A UB3LYP hybrid functional and EPR-II or 6-311+G** basis sets were used, and all calculations were performed with the Gaussian 03 package. For the planar fluorinated radicals the calculated dipolar contribution to the F^α hfc tensor has spectacular large near axial values, surprisingly with the positive component pointing parallel to the p_z orbital. This may mean that some of the unpaired electron delocalizes onto F^α and this is further supported by the shorter $\text{C}^\alpha\text{--}F^\alpha$ bonds compared to $\text{C}^\beta\text{--}F^\beta$ bonds. The spin density is localized mostly at the C^α atom (*ca.* 83%), but there is also *ca.* 6% spin density at each F^α atom. For the non-planar fluorinated radicals the calculated dipolar contribution to the F^α hfc tensor shows again large values and very little variation for the different conformations or additional CF_3 substitution. This means that the effective hfc (the sum of isotropic plus dipolar contributions) can vary in a rigid system, depending on orientation with respect to the applied magnetic field, between nearly zero and +227 G, which is not unexpected but can pose a challenge for the observation and assignment of experimental spectra.

The present DFT calculations do not provide clear evidence for deviations from planarity for the non-fluorinated ethyl radical, but in contrast the optimized fluorinated ethyl radical is essentially non-planar, so that the geometry is closer to tetrahedral (the sum of the three bond

angles at the radical center amounts to 341° as compared to 329° for a fully tetrahedral and 360° for a planar geometry). Interestingly non-planarity leads to a net increase of the isotropic hfc at F^α , but a decrease at F^β for the $CF_3\cdot CF_2$ and $CF_3CF_2\cdot CF_2$ radicals.

The dipolar contribution is expected to be much smaller for β - than for α -nuclei. The situation is quite dramatic for the planar fluorinated species where the calculated positive dipolar component of the eclipsed F^β amounts to *ca.* 71 G and this large value cannot be explained by a purely dipolar interaction but must reflect large spin polarization which leads to a significant change in the spin distribution. The predicted anisotropy of 0.14% for the *g*-tensor of $\cdot CF_3CF_2$ is sizable, nearly four times that of the non-fluorinated ethyl radical, and can lead to a line splitting of *ca.* 5 G in X-band ESR spectroscopy, which may be essential for the interpretation of solid state spectra.

The present study shows that DFT methods are capable of effectively describing fluorinated compounds and delivers valuable additional information about properties of radical intermediates formed during polymer aging processes.

ZUSAMMENFASSUNG

Die vorgestellte Arbeit setzt sich aus drei Teilen zusammen, die sich mit der Optimierung von Polymeren beschäftigen, die für den Einsatz als protonenleitende Membranen für PEM-Brennstoffzellen geeignet sind. Der Fokus ist die oxidative and photochemische Stabilität von nicht-fluorierten Polymermembranen, ebenso wie die strahleninduzierte Pfropfreaktionen von marktüblichen Fluorpolymeren. Gemeinsam ist den ersten zwei Teilen der Einsatz der Elektronen Spin Resonanz (ESR), einer geeigneten Methode, welche der Nachweis und die Analyse radikalischer Zwischenprodukte, sowie die Identifikation von strahleninduzierten Radikalen in organische Polymere gestattet. Der dritte Teil umfasst die DFT Rechnungen von nicht-fluorierten und fluorierten Fragmenten.

Der oxidative Abbau von Polymeren ist normalerweise ein oxidativer Radikalprozess, der den Angriff von HO^\bullet und HOO^\bullet Radikalen umfasst. Es ist bekannt, dass die Membrandegradation in einer laufenden Brennstoffzelle von HO^\bullet und HOO^\bullet Radikalen, die während der unvollständigen Sauerstoffreduktion gebildet werden, verursacht wird. Ein Hinweis auf die Entstehung dieser Radikale während dem Betrieb der Brennstoffzellen ergibt sich aus dem Nachweis geringer Mengen an Wasserstoffperoxid im Produktwasser. Diesen Radikalen schreibt man einen entscheidenden Anteil an den Zersetzungsreaktionen zu, die zu einer vorzeitigen Alterung insbesondere der neuentwickelten protonenleitenden Membranen auf der Basis sulfonierter aromatischer Kohlenwasserstoffe führen.

Um den Mechanismus dieser Zersetzungsreaktionen näher untersuchen zu können, wurden für diese Untersuchung fünf nicht-fluorierte aromatische Monomere als Modellverbindungen für protonenleitende Membranen ausgewählt und die entsprechenden Abbauprodukte in Abhängigkeit des pH-Werts über die ESR-Spektroskopie analysiert. Im Einzelnen handelte es sich dabei um 4,4'-Sulfonyldiphenol (SDP), Bisphenol A (BPA), 4,4'-Diphenol (DP), 4,4'-Dihydroxybenzophenon (HBP) und sulfoniertes 4,4'-Dichlordiphenylsulfon. Als Quelle für sauerstoffhaltige Radikale wurde die Photolyse von Wasserstoffperoxid eingesetzt. Auf diesem Weg werden hauptsächlich HO^\bullet -Radikale gebildet. Die Versuche wurden mit und ohne H_2O_2 durchgeführt, um den HO^\bullet -Radikalangriff von der direkten Photolyse zu unterscheiden. Eine detaillierte Untersuchung für die Abhängigkeit vom pH-Wert wurde für die SDP, BPA und DP Monomeren durchgeführt.

Auffällig ist, dass bei den pH-Wert-Experimenten gerade in der Nähe der pK_S -Wertes von HO^\bullet (11,9) und H_2O_2 (11,7) die maximale Bildung von Phenoxyradikalen von BPA und SDP auftrat. Außerdem sind $\text{O}^{\bullet-}$ und $\text{O}_2^{\bullet-}$ Radikale von nucleophilem Charakter. Damit haben sie eine hohe Tendenz zur Abstraktion eines H^\bullet -Atoms von dem OH-Substituenten am aromatischen Ring. Bei dieser Abstraktion werden primäre Phenoxyradikale gebildet. Die Abstraktion eines H^\bullet -Radikals durch aus dem Anion HO_2^- gebildeten HO^\bullet -Radikale ist um etwa 280 mal schneller als aus der protonierten H_2O_2 Ausgangsform [67]. Das bedeutet, dass in der Nähe des pK_S -Wertes von H_2O_2 die Bildung erheblicher Mengen des Superoxidradikalanions $\text{O}_2^{\bullet-}$ einsetzt, welches seinerseits direkt mit den Monomeren reagieren kann. Ersatzweise kann $\text{O}_2^{\bullet-}$ auch mit HO^\bullet oder $\text{O}^{\bullet-}$ unter der Bildung von Sauerstoff weiter reagieren [67]. Der bei dieser Reaktion gebildete Sauerstoff weist eher Singulett-Charakter auf. Es ist bekannt, dass $^3\text{O}_2$ zu einem ausgeprägten Spinaustausch und damit zu einem deutlichen Verlust an Hyperfeinstruktur in den ESR-Spektren führen sollte. Stattdessen wurden in dem alkalischen pH-Bereich ESR-Spektren mit gut aufgelöster Hyperfeinstruktur erhalten. Aufgrund dieser Erkenntnis kann vermutet werden, dass die Fähigkeit von $^1\text{O}_2$, sich direkt an aromatische Ringe zu addieren, zur Bildung der beobachteten dioxysubstituierten Radikale beiträgt. Aufgrund der Tendenz der Superoxidradikalanionen $\text{O}_2^{\bullet-}$, sich direkt an aromatische Ringe anzulagern, ist es sinnvoll, dass diese Radikale ebenfalls an der Bildung der dioxysubstituierten Verbindungen beteiligt sind. Reaktionsmechanismen wurden für die Bildung der Phenoxyradikale vorgeschlagen. Die große Zahl von neuen Radikalen beweist die mehrfache Hydroxylierung der aromatischen Ringe. Dies deutet darauf hin, dass für Brennstoffzellen die höheren pH-Werte sehr schädlich sind und zum schnellen Abbau der Membranen führen können. Das heisst, dass auch innerhalb der Brennstoffzelle lokal höhere pH-Werte vorherrschen, bei denen die beschriebenen Zersetzungsreaktionen ablaufen können. Die höheren pH-Werte können unter Bedingungen vom Brenngasmangel oder erheblichen örtlichen Unterschieden über die Membran auftreten.

Stark desaktivierende Substituenten wie SO_3^- und SO_2 , die einen $-I/-M$ Effekt ausüben, dirigieren nukleophile Substitution in die *meta* Position. Ein Oxysubstituent im System würde aufgrund seiner stark aktivierenden Wirkung ($+I/+M$ Effekt) eine weitere Substitution in *ortho* oder *para* Positionen begünstigen. Es ist bekannt daß die Sulfongruppe desaktivierend wirkt. Auf diese Weise zeigt das SDP Monomer Vorteile in Bezug auf chemische Stabilität gegen der HO^\bullet Addition. Weiterhin empfiehlt es sich, den aromatischen Ring durch geeignete Substituenten vor dem Angriff von HO^\bullet zu schützen. Ein SO_3^- -Substituent wirkt

desaktivierend und dient darüber hinaus der Erhöhung der Protonenleitfähigkeit. Die Blockierung eines aromatischen Ringes beispielweise mit Fluor limitiert die HO[•]-Additionreaktionen.

Es wurde auch gezeigt dass die direkte Photolyse der Monomeren zu Semichinonanonradikalen führt. Für SDP, BPA und HBP resultiert die Spaltung der C–C-Bindung im *p*-Benzosemichinonradikalanion, DP dagegen spaltet nicht sondern photooxidiert und führt zum *p*-Dipheno-Benzosemichinonradikalanion. Bei pH < 10 führt die Photolyse von H₂O₂ zu HO[•]-Radikalen. Letztere reagieren leichter mit dem Lösungsmittel Methanol als mit dem Substrat. Das Hydroxymethylradikal wurde als Zwischenprodukt doch abgefangen mit der Hilfe von Radikalfallenmolekülen (zum Beispiel 3,5-Dibrom-4-Nitrosobenzol-Sulfonsäure). Unter saueren oder neutralen Bedingungen wurden keine Radikale beobachtet. Es ist zu erwarten, dass bei pH unterhalb 11,7 vor allem die Addition der HO[•]-Radikale an die aromatischen Ringe abläuft. Diese tritt bevorzugt in *ortho*-Position zu den Alkyl- und RO-Substituenten auf (da bei den sulfonierten Formen von PSU und PEK die *para*-Position substituiert und damit gegenüber einem Angriff blockiert ist) [47]. Die Tatsache, dass keine Radikale beobachtet wurden, zeigt eventuell, dass die Lebensdauer dieser Radikale (falls gebildet) sehr kurz sein sollte. Da die Konzentration entweder zu gering ist oder die Signale in viele Linien aufspalten oder sehr breit sind, liegen diese Signale unterhalb der ESR-Nachweisgrenze. Im ersten Teil dieser Arbeit wurde demonstriert, dass O₂^{•-} und ¹O₂, die im alkalischen pH-Bereich auftreten, für die Bildung von Phenoxy- und Semichinonanonradikalen verantwortlich sind.

In Teil 2 der Arbeit wurden drei verschiedene elektronenbestrahlte Fluorpolymere - Poly(ethylen-alt-tetrafluorethylen) (ETFE), Poly(tetrafluorethylen-co-hexafluorpropylen) (FEP) und Poly(vinylidenfluorid) (PVDF), ebenso wie die Strahlungspfpfreaktionen von Styrol, 25% Styrol in Benzol und 25% Styrol in Ethanol auf die oben genannten Fluorpolymere über die ESR-Spektroskopie untersucht. Trotz früheren Untersuchungen mit Fluorpolymeren existierten zu Beginn der Arbeit noch Lücken in den Kenntnissen und Daten. Zum Beispiel waren Molekulargewicht, Kristallinität oder Orientierung der FEP-, ETFE- und PVDF-Materialen nicht immer bekannt. Ebenso waren in früheren Arbeiten verschiedene Strahlungsquellen und Dosen verwendet worden. Deshalb waren die relativen Geschwindigkeiten für den Radikalzerfall von unter Luft oder unter Schutzgas bestrahlten Fluorpolymeren nicht immer bekannt. Auch die Strahlungspfpfreaktionen verschiedener Polymere waren nicht bei vergleichbaren Reaktionsbedingungen durchgeführt worden. Es gab keine Einigkeit über die auf bestrahlten FEP- und PVDF-Polymeren gebildet Radikale, und

wenig war über die Radikale gebildet auf bestrahltem ETFE publiziert. Auch waren keine aktuellen ESR-Untersuchungen mit elektronenbestrahltem PVDF mit Dosen < 100 kGy bekannt.

Diese offenen Fragen wurden in dieser Arbeit diskutiert. Erstens war es möglich die Strahlenchemie der drei Fluorpolymere zu vergleichen. Die Strahlungsquellen, Dosen und Strahlungsatmosphären waren für alle drei Fluorpolymere gleich. Zweitens war es möglich, die Radikalzerfallsgeschwindigkeiten für die verschiedenen Fluorpolymere zu vergleichen und den Einfluss der Strahlungsatmosphäre und des Lösungsmittels zu verstehen.

Die experimentellen ESR-Spektren bei $+60$ °C von unter Schutzgas elektronenbestrahltem ETFE bestehen überwiegend aus dem bei der Abstaltung eines H-Atoms resultierenden sekundären Radikal. Die experimentellen ESR-Spektren von FEP bestehen bei $+60$ °C aus primären, sekundären und tertiären Radikalen. Das bei der C–C Bindungsspaltung resultierende primäre Radikal ist die Majoritätspezies. In den Spektren bei -120 °C des unter Schutzgas elektronenbestrahlten PVDF ist bereits eine Feinstruktur angedeutet, die sich bei weiterer Erwärmung bis auf $+60$ °C nicht mehr wesentlich ändert. Dies deutet auf eine höhere Beweglichkeit der Polymerketten schon bei -120 °C hin. Die Spinkonzentrationen sind bei ETFE nach der Bestrahlung unter Schutzgas oder Luft immer doppelt so hoch wie bei FEP. Erfolgt die Bestrahlung der Proben unter Luft, so werden bei ETFE und PVDF 50% weniger Radikale erzeugt als bei der Bestrahlung unter Schutzgas, aber dasselbe gilt nicht für FEP. Dies dürfte durch die höhere Sauerstoffsolubilität in perfluorierten Medien begründet sein. Die höheren Spinkonzentrationen in ETFE können für die Herstellung von Membranen mit deutlich höheren Pfropfgraden und damit möglichen höheren Ionenaustauschkapazitäten ausgenützt werden.

Bei der Bestrahlung von FEP und ETFE unter Luft werden ausschließlich Peroxyradikale erhalten. Die Pfropfreaktion auf Peroxyradikale an ETFE verläuft über Alkyldradikalzentren, die erst nach der Übertragung von H-Atomen auf die Peroxygruppen am Gerüstpolymer gebildet werden. Die resultierenden Radikalzerfallskurven in ETFE und FEP bestrahlt mit 40 kGy entsprechen einfachen Exponentialfunktionen (ausgenommen wenn Benzol als Lösungsmittel für die Peroxyradikale verwendet wird). Die Anpassung der Exponentialfunktion an die Messwerte liefert die Geschwindigkeitskonstanten, die einen direkten Vergleich der Pfropfreaktionen an den beiden Polymeren unter den jeweiligen Reaktionsbedingungen erlauben.

Die Abnahme der Signalintensitäten während der Pfropfreaktion von Styrol, verdünnt mit Benzol, auf Alkyldradikale an FEP ist fast viermal schneller (trotz viermal niedrigerer

Konzentration von Benzol) als wenn unvermisches Styrol verwendet wird. Bei Peroxyradikalen erhöht sich die Geschwindigkeit um einen Faktor 10, wenn Benzol als Verdünnungsmittel eingesetzt wird. Die Werte für ETFE zeigen eine ähnliche Tendenz, nur mit niedrigeren Erhöhungsfaktoren. Das könnte deshalb ein Nachweis für erfolgreiche Quellung sein. Allerdings könnte das Benzol auch mit den Radikalzentren an den Polymerketten reagieren. Für eine Konzentration von 25% Styrol in Benzol könnte eine solche Radikalübertragung diese Erhöhung um einen Faktor 4 verringern. Die Verdünnung mit Ethanol erhöht die Pflropfgeschwindigkeit nicht.

Aus der Massenzunahme während der Reaktion lässt sich der Pflropfgrad für die jeweilige Reaktion bestimmen. Die Pflropfgrade an FEP liegen bei sämtlichen Reaktionen etwa 30% bis 80% unterhalb derjenigen an ETFE. Der Effekt ist weniger ausgeprägt auf gepfropften Hauptketteneinheiten CF_2 (CH_2). Die Kristallinität und die Molekülmasse sind von großer Bedeutung für PVDF. Die Diffusion der Styrolmonomere in das Gerüstpolymer, die Radikalausbeute und die Kompatibilität mit der gepfropften Komponente sind die einschränkenden Faktoren für FEP und ETFE. Der Einsatz von Verdünnungsmitteln für alle drei Fluorpolymere verringert die Pflropfgrade, verglichen mit unverdünnten Styrol. Gemäß den aus der Massenzunahme der Filme nach der Pflropfreaktion und der anfänglichen Spinkonzentration gemachten Abschätzungen führt die Pflropfreaktion unter Schutzgas (bei $+60\text{ °C}$) zur Ausbildung längerer Polymerketten, während die Reaktion unter Luft bei der gleichen Temperatur zur Ausbildung kürzerer Ketten führt.

Für praktische Anwendungen müssen protonenleitende Membranen verschiedene Eigenschaften erfüllen, wie zum Beispiel mechanische Stabilität bei verschiedenen relativen Feuchten und Temperaturen, hohe Protonenleitfähigkeit und einen großen Bereich von Betriebstemperaturen von unter 0 bis zu $+90\text{ °C}$. Durch Variation der Sauerstoffkonzentration bei der Bestrahlung und der Reaktionstemperatur bei den Pflropfreaktionen können die Kettenlängen und der Vernetzungsgrad und dadurch das Quellverhalten und die Mobilität der Funktionsgruppen der Membran beeinflusst werden. Strahlungspflropfreaktionen können diese Spezifikationen in einem relativ frühen Stadium der Membranherstellung beeinflussen. Die oben beschriebenen Ergebnisse sind von Bedeutung bei der Optimierung der verschiedenen Parameter, welche die Strahlungspflropfreaktion beeinflussen.

Beim Strahlungspflropfen mit Styrol von Polymeren für Brennstoffzellenanwendungen ist es wichtig, zu kontrollieren, ob die Polystyrolkette auf ein Peroxyradikal oder ein kohlenstoffzentriertes Radikal gepfropft wird. Unterschiedliche Bindungsstärken verhindern, dass die gepfropfte Kette sich abspalte. Thermodynamische Eigenschaften kleiner Alkyl- und

Alkyl-Peroxyradikale wurden mittels DFT studiert, um primäre, sekundäre und tertiäre Radikale in nicht-fluorierten und perfluorierten Polymeren zu modellieren. Das B3LYP-Funktional und ein 6-311+G**-Basis-Satz wurden verwendet, und alle Rechnungen wurden im Rahmen des Gaussian 98 Programmes ausgeführt. Basierend auf den berechneten Bindungsdissoziationsenergien ist eine durch Entropieerhöhung begünstigte Abspaltung von molekularem Sauerstoff der wahrscheinlichste Prozess für die Umwandlung von Peroxy- zu Alkylradikalen für FEP und PE. Die Abspaltung von atomarem Sauerstoff ist unwahrscheinlich. Peroxyradikale sind nicht in der Lage, F von C–F Bindungen abzuspalten, aber H-Abstraktion könnte mit der Sauerstoffabspaltung konkurrieren. Für Alkoxyradikale ist thermodynamisch keine F-Abstraktion sondern eine H-Abstraktion begünstigt. Allgemein zeigen die DFT Rechnungen, dass F starke und manchmal nicht vermutete Ladungspolarisationen in Molekülen verursachen kann.

Geometrie und Ladungsverteilung des sekundären und tertiären Peroxyradikals sind völlig oder fast völlig symmetrisch bezüglich des Radikalzentrums. Das C–C-Rückgrat dieser Strukturen repräsentiert eine trans-Konformation. Dies ist auch für das sekundäre, nicht fluorierte Alkylradikal gültig, doch ist die Symmetrie leicht gebrochen für die optimierten Strukturen der sekundär fluorierten, tertiär nicht-fluorierten und fluorierten Alkylradikale, in denen wir gauche-Elemente finden. Interessanter ist der leichte C–C Bindungslängenunterschied und besonders die Ladungspolarisation von bis zu 0.4 e, die von der gebrochenen Symmetrie kommt. Es ist bekannt, dass C–F Bindungen sehr empfindlich auf stereoelektronische Effekte sind. Für die gegenwärtigen fluorierten Radikale könnte das bedeuten, dass sie eine ziemlich unterschiedliche chemische Reaktivität der trans-Konformation im Vergleich zur gauche-Konformation zeigen.

In DFT Rechnungen wurde gezeigt, dass ausgeprägte Spinpolarisationseffekte zum unerwarteten Verhalten der Hyperfeinanisotropie führen. Dies wurde bei dem Vergleich zwischen den Parametern von $\text{CF}_3\cdot\text{CF}_2$ sowohl voll optimiert als auch erzwungen planar mit den Parametern des hauptsächlich planaren $\text{CH}_3\cdot\text{CH}_2$ Radikal bewiesen. Die fluorierten und nicht-fluorierten 1-Propyl-Radikale wurden auch in Kürze diskutiert. Das UB3LYP-Funktional mit dem 6-311+G**- oder EPR-II-Basis-Satz wurden in diesem Fall verwendet, und alle Rechnungen wurden im Rahmen des Gaussian 03 Programmes ausgeführt. Die berechneten dipolaren Beiträge zum F^α hfc-Tensor für die planaren fluorierten Radikale zeigen spektakulär große, fast axiale Werte. Die positive Komponente ist erstaunlicherweise parallel zum p_z -Orbital ausgerichtet. Das kann bedeuten, dass ein Teil des ungepaarten Elektrons auf F^α delokalisiert. Kürzere $\text{C}^\alpha\text{--F}^\alpha$ Bindungen im Vergleich zu den $\text{C}^\beta\text{--F}^\beta$

Bindungen unterstützen diese Annahme. Die Spindichte ist größtenteils auf C^α (ca. 83%) lokalisiert, aber es gibt auch ca. 6% Spindichte auf jedem F^α -Atom. Die berechneten dipolaren Beiträge zum F^α hfc-Tensor für nicht-planare fluorierte Radikale zeigen ebenfalls große Werte. Für die verschiedenen Konformationen oder bei zusätzlicher CF_3 Substitution ist kaum eine Veränderung zu sehen. Das bedeutet, dass die effektive hfc (die Summe von isotropen plus dipolaren Beiträgen) in einem rigiden System variieren kann. Diese Variation zwischen ungefähr 0 und +227 G ist von der Orientierung in Bezug auf das angelegte Magnetfeld abhängig. Das kommt nicht unerwartet, könnte aber bei der Beobachtung und der Zuordnung von experimentellen Spektren Schwierigkeiten verursachen.

Unsere Rechnungen zeigen keine Abweichung von der planaren Struktur im Fall des nicht-fluorierten Ethylradikals. Im Gegensatz dazu ist das optimierte fluorierte Ethylradikal hauptsächlich nichtplanar. Die Geometrie ist nahezu tetraedrisch (die Summe der drei Bindungswinkel am Radikalzentrum beträgt 341° gegenüber 329° für völlig tetraedrische Geometrie, und gegenüber 360° für planare Geometrie). Interessanterweise führt Nichtplanarität für die $CF_3\cdot CF_2$ und $CF_3CF_2\cdot CF_2$ Radikale zu einem Nettoanstieg der isotropen hfc am F^α aber zu einer Verkleinerung am F^β .

Es wird erwartet, dass der dipolare Beitrag für β - kleiner als für α -Kerne ist. Die Situation ist drastisch für das planare fluorierte Radikal, bei dem der berechnete positive dipolare Beitrag zum ekliptischen F^β ca. 71 G beträgt. Das sollte eine große Spinpolarisation darstellen, welche zu wesentlichen Veränderungen in der Spinverteilung führt. Die erwartete Anisotropie von 0.14% für den g -Tensor von $CF_3\cdot CF_2$ ist erheblich, ungefähr viermal größer als die Anisotropie für $CH_3\cdot CH_2$, und dies könnte sehr wichtig für die Auswertung von Festkörperspektren sein.

Unsere Rechnungen demonstrieren, dass DFT-Methoden für die effektive Beschreibung von fluorierten Verbindungen brauchbar sind. Diese Arbeit bietet zusätzliche Erkenntnisse über Eigenschaften von radikalischen Zwischenprodukten, die während Polymeralterungsprozessen gebildet werden.

ACKNOWLEDGEMENT

First of all I would like to thank Prof. Dr. Emil Roduner for giving me the opportunity to become a member of his group and for the scientific supervision of my PhD work. I am very grateful for his permanent support, encouragement and invaluable discussions.

Taking the chair of the examination board by Prof. Dr. Friedhelm Zabel is kindly acknowledged. Writing the second advisory opinion by Prof. Dr. Andreas Friedrich is also kindly acknowledged.

I thank all my group colleagues for contributing to a pleasant working atmosphere. In particular, Dr. Herbert Dilger for his help with ESR and for the salvation of many technical problems. Dr. Igor Tkach for the valuable discussions on advanced ESR techniques and other spectroscopic methods.

My thank goes to Dr. Alexander Panchenko for introducing to me Gaussian 98 package as well as for his assistance with DFT calculations and for the valuable discussions on fuel cells.

I thank Dr. Jochen Kerres from Institute for Chemical Engineering, University of Stuttgart for providing me with different monomers and polymers used in low temperature fuel cells.

I thank Dr. Hans-Peter Brack and Dr. Günther Scherer from Electrochemistry Laboratory, Paul Scherrer Institut, Switzerland for the electron irradiation of the fluoropolymer films and for the useful discussions on radiation grafting methods.

I thank Dr. Stefan Jagiella for helpful discussions on DFT calculations. Dr. Roman Reviakin from Institute of Inorganic Chemistry, University of Würzburg is acknowledged for help with quantum chemical programs.

ACKNOWLEDGEMENT

The support by the mechanical, the electonical and the glassblower workshop is kindly acknowledged.

Many special thanks to my wife for her patience, tolerance and encouragement.

BIBLIOGRAPHY

- [1] G.A. Olah, A. Goeppert, G.K.S. Prakash, *Beyond Oil and Gas: the Methanol Economy*, Wiley-VCH Verlag GmbH & Co. (2006).
- [2] F. Barbir, *PEM Fuel Cells: Theory and Practice*, Elsevier Academic Press (2005).
- [3] K. Kordesch, G. Simander, *Fuel Cells and Their Applications*, VCH Publishers, New York (1996).
- [4] L. Gubler, S.A. Gürsel, G.G. Scherer, *Fuel Cells*, **5**, 317 (2005).
- [5] Q. Li, R. He, J.O. Jensen, N.J. Bjerrum, *Chem. Mater.*, **15**, 4896 (2003).
- [6] C.A. Sperati, *Fluorocarbon Polymers*, in *Handbook of Plastic Materials and Technology*, 93 (1990).
- [7] S. Gottesfeld, T.A. Zawodzinski, in *Advances in Electrochemical Science and Engineering*; R.C. Alkire, H. Gerischer, D.M. Kolb, C.W. Tobias, eds., p. 195, Wiley-VCH, Weinheim, Germany (1997).
- [8] P. Costamagna, S. Srinivasan, *J. Power Sources*, **102**, 242 (2001).
- [9] W.G. Grot, *Macromol. Symposia*, **82**, 161 (1994).
- [10] G. Alberti, M. Casciola, *Solid State Ionics*, **145**, 3 (2001)
- [11] F. Babir, T. Gomez, *Int. J. Hydr. Energy*, **21**, 891 (1996).
- [12] P. Zegers, *J. Power Sources*, **154**, 497 (2004).
- [13] K.T. Adjemian, S. Srinivasan, J. Benziger, A.B. Bocarsly, *J. Power Sources*, **109**, 356 (2002).
- [14] X. Ren, T.E. Springer, S. Gottesfeld, *J. Electrochem. Soc.*, **147**, 92 (2000).
- [15] V.M. Barragan, C. Ruiz-Bauza, J.P.G. Villaluenga, B. Seoane, *J. Power Sources*, **130**, 22 (2004).
- [16] A. Bosnjakovic, S. Schlick, *J. Phys. Chem. B*, **108**, 4332 (2004).
- [17] C. Huang, K.S. Tan, J. Lin, K.L. Tan, *Chem. Phys. Lett.*, **371**, 80 (2003).
- [18] A.B. LaConti, M. Hamdan, R.C. McDonald, *Mechanisms of Membrane Degradation for PEMFCs*, in *Handbook of Fuel Cells - Fundamentals, Technology and Applications*, vol. 3, John Wiley & Sons, Ltd (2003).
- [19] R. Baldwin, M. Pham, A. Leonida, J. McElroy, T. Nalette, *J. Power Sources*, **29**, 399 (1990).
- [20] W. Liu, K. Ruth, G. Rusch, *J. New Mater. Electrochem. Syst.*, **4**, 227 (2001).

- [21] E. Roduner and S. Schlick, *ESR Methods for Assessing the Stability of Polymer Membranes Used in Fuel Cells*, in: S. Schlick, editor, *Advanced ESR Methods in Polymer Research*, John Wiley & Sons, New York (2006).
- [22] G.G. Scherer, *Ber. Bunsenges. Phys. Chem.*, **94**, 1008 (1990).
- [23] B. Gupta, F.N. Buechi, G.G. Scherer, *Solid State Ionics*, **61**, 213 (1993).
- [24] A.E. Steck, C. Stone, *US Patent* 5834523 (1998).
- [25] C. Stone, A.E. Steck, *U.S. Patent* 6359019 (2002).
- [26] C. Stone, A.E. Steck, B. Choudhury, *U.S. Patent* 6723758 (2004).
- [27] A.B. LaConti, *Workshop on Perfluorinated Ionomer Membranes*, Lake Buena Vista, FL, Amer. Chem. Society, Washington, DC (1982).
- [28] J. Wei, C. Stone, A.E. Steck, WO 95/08581, Ballard Power Systems, Int. Publ. (1995).
- [29] J. Roziere, D. Jones, *Annu. Rev. Mater. Res.*, **33**, 503 (2003).
- [30] B. Yang and A. Manthiram, *Electrochem. Sol. State Lett.*, **6**, A229 (2003).
- [31] S. Vetter, B. Ruffmann, I. Buder, S.P. Nunes, *J. Membr. Sci.*, **260**, 181 (2005).
- [32] F. Wang, M. Hickner, Y.S. Kim, T.A. Zawodzinski, J.E. McGrath, *J. Membr. Sci.*, **197**, 231 (2002).
- [33] M. Rikukawa, K. Sanui, *Prog. Polym. Sci.*, **25**, 1463 (2000).
- [34] B. Bonnet, D. Jones, J. Roziere, L. Tchicaya, G. Alberti, M. Casciola, L. Massinelli, B. Baner, A. Peraio, E. Ramunni, *J. New Mater. Electrochem. Syst.*, **2**, 87 (2000).
- [35] S. Mitov, B. Vogel, E. Roduner, J. Kerres, M. Hein, D. Xing, F. Schönberger, H. Zhang, X. Zhu, V. Gogel, L. Jörissen, *Fuel Cells*, **6**, 413 (2006).
- [36] W.L. Harrison, M.A. Hickner, Y.S. Kim, J.E. McGrath, *Fuel Cells*, **5**, 201 (2005).
- [37] O. Savadogo, B. Xing, *J. New Mat. Electrochem. Systems*, **3**, 345 (2000).
- [38] J. Kerres, *J. Membr. Sci.*, **185**, 3 (2001).
- [39] J. Kerres, A. Ulrich, M. Hein, *J. Polym. Sci. Part A: Polym. Chem.*, **39**, 2874 (2001).
- [40] A. Noshay, L.M. Robeson, *J. Appl. Polym. Sci.*, **20**, 1885 (1976).
- [41] J. Kerres, W. Zhang, L. Jörissen, V. Gogel, *J. New Mater. Electrochem. Syst.*, **5**, 97 (2002).
- [42] J.G. Calvert, J.N. Pitts, *Photochemistry*, John Wiley & Sons, Inc. New York (1966).
- [43] E.J. Anderton, H.T. J. Chilton, G. Porter, *Proc. Chem. Soc. (London)*, 352 (1960).
- [44] H. Wang, G.A. Capuano, *J. Electrochem. Soc.*, **145**, 780 (1998).
- [45] F.N. Büchi, B. Gupta, O. Haas, G.G. Scherer, *Electrochim. Acta*, **40**, 345 (1995).
- [46] W. Liu, D. Zuckerbrod, *J. Electrochem. Soc.*, **152**, A1165 (2005).
- [47] G. Hübner, E. Roduner, *J. Mater. Chem.*, **9**, 409 (1999).

- [48] Q. Guo, P.N. Pintauro, H. Tang, S. O' Connor, *J. Membr. Sci.*, **154**, 175 (1999).
- [49] J. Yu, D. Xing, F. Liu, Z. Shao, Y. Fu, H. Zhang, *Phys. Chem. Chem. Phys.*, **5**, 611 (2003).
- [50] H. Ericson, T. Kallio, T. Lehtinen, B. Mattsson, G. Sundholm, F. Sundholm, P. Jacobsson, *J. Electrochem. Soc.*, **149**, A206 (2002).
- [51] M. Watanabe, U. Hiroyuki, E. Masomi, *J. Electrochem. Soc.*, **145**, 1137 (1998).
- [52] A. Pozio, R.F. Silva, M. De Francesco, L. Giorgi, *Electrochim. Acta*, **48**, 1543 (2003).
- [53] L. Zhang, S. Mukerjee, *J. Electrochem. Soc.*, **153**, A1062 (2006).
- [54] E. Yeager, *Electrochim. Acta*, **29**, 1527 (1984).
- [55] T.J. Schmidt, U.A. Paulus, H.A. Gasteiger, R.J. Behm, *J. Electroanal. Chem.*, **508**, 41 (2001).
- [56] E. Endoh, S. Trezono, H. Widjaja, Y. Takimoto, *Electrochem. Solid State Lett.*, **7**, A209 (2004).
- [57] G. Hübner, *Dissertation*, Universität Stuttgart (1999).
- [58] D. Behar, J. Rabani, *J. Phys. Chem.*, **92**, 5288 (1988).
- [59] A. Panchenko, *J. Membr. Sci.*, **278**, 269 (2006).
- [60] S. Lunak, P. Sedlak, *J. Photochem. Photobiol. A: Chem.*, **68**, 1 (1992).
- [61] N. Jacob, I. Balakrishnan, M.P. Reddy, *J. Phys. Chem.*, **81**, 17 (1977).
- [62] E.J. Wolfrum, D.F. Ollis, *Aqu. Surf. Photochem.*, **2**, 451 (1994).
- [63] P. Neta, M.Z. Hoffmann, M. Simic, *J. Phys. Chem.*, **76**, 847 (1972).
- [64] K. Eiben, R.W. Fessenden, *J. Phys. Chem.*, **75**, 1186 (1971).
- [65] K. Makino, M.M. Mossoba, P. Riesz, *J. Phys. Chem.*, **87**, 1369 (1983).
- [66] H. Kaczmarek, L.A. Linden, J.F. Rabek, *Polym. Degrad. Stab.*, **47**, 175 (1995).
- [67] G.V. Buxton, C.L. Greenstock, W.P. Helman, A.B. Ross, *J. Phys. Chem. Ref. Data*, **17**, 513 (1988).
- [68] Landolt-Börnstein, *New Ser. II*: **17c**, 92 (1987); **17c**, 171 (1987); **17e**, 36 (1988); **17g**, 78 (1989).
- [69] S. Mitov, O. Delmer, J. Kerres, E. Roduner, *Helv. Chim. Acta*, **89**, 2354 (2006).
- [70] A. Chapiro, *Radiation Chemistry of Polymeric Systems*, Wiley: New York (1962).
- [71] B. Gupta, G.G. Scherer, *Chimia*, **48**, 127 (1994).
- [72] R.L. Clough, *Nucl. Instrum. Methods Phys. Res. B*, **185**, 8 (2001).
- [73] H.P. Brack, G.G. Scherer, *Macromol Symp.*, **126**, 25 (1997).
- [74] B. Gupta, F.N. Buechi, G.G. Scherer, *J Polym. Sci. Part A: Polym. Chem.*, **32**, 1931 (1994).

- [75] B. Gupta, G.G. Scherer, *Angew. Makromol. Chemie*, **210**, 151 (1993).
- [76] I. Guilmeau, S. Esnouf, N. Betz, A. Le Moel, *Nucl. Instr. and Methods in Phys. Research B*, **131**, 270 (1997).
- [77] C. Aymes-Chodur, S. Esnouf, A. Le Moel, *J. Polym. Sci. Part B: Polym. Phys.*, **39**, 1437 (2001).
- [78] N. Walsby, M. Paronen, J. Juhanaja, F. Sundholm, *J. Polym. Sci. Part A: Polym. Chem.*, **38**, 1512 (2000).
- [79] E.S.A. Hegazy, I. Ishigaki, J. Okamoto, *J. Appl. Polym. Sci.*, **26**, 3117 (1981).
- [80] M.M. Nasef, H. Saidi, M.A. Yarmo, *J. Appl. Polym. Sci.*, **77**, 2455 (2000).
- [81] L. Gubler, H. Kuhn, T.J. Schmidt, G.G. Scherer, H.P. Brack, F. Simbeck, *Fuel Cells*, **4**, 196 (2004).
- [82] A.B. Geiger, T. Rager, L. Matejcek, G.G. Scherer, A. Wokaun, in *Proceedings of the First European PEFC Forum*, F.N. Büchi, G.G. Scherer and A. Wokaun, Editors, p. 124 (2001).
- [83] F.N. Büchi, B. Gupta, O. Haas, G.G. Scherer, *J. Electrochem. Soc.*, **142**, 3044 (1995).
- [84] H.P. Brack, F.N. Büchi, J. Huslage, M. Rota, G.G. Scherer, in *Membrane Formation and Modification*, I. Pinnau, B.D. Freeman, Ed.; ACS Symposium Series 744, p.174, Amer. Chem. Society: Washington D.C (1999).
- [85] J.A. Horsfall, K.V. Lovell, *Fuel Cells*, **1**, 186 (2001).
- [86] J.A. Horsfall, K.V. Lovell, *Polym. Adv. Technol.*, **13**, 381 (2002).
- [87] H.P. Brack, H.N. Bühner, L. Bonorand, G.G. Scherer, *J. Mater. Chem.*, **10**, 1795 (2000).
- [88] J. Dobo, F. Hedvig, *J. Polym. Sci. Part C: Polym. Symp.*, **44**, 2577 (1967).
- [89] H. Sakurai, M. Shiotani, H. Yahiro, *Rad. Phys. Chem.*, **56**, 309 (1999).
- [90] M.P. Tonge, A. Kajiwara, M. Kamachi, R.G. Gilbert, *Polymer*, **39**, 2305 (1998).
- [91] N.E. Skeins, *Radiat. Phys. Chem.*, **15**, 47 (1980).
- [92] M.S. Jahan, K.S. McKinny, *Nucl. Instr. and Meth. in Phys. Res. B*, **151**, 207 (1999).
- [93] P.W. Teare, *Acta Cryst.*, **12**, 294 (1959).
- [94] S. Kavesh, J.M. Schultz, *Polym. Sci. Part A-2*, **8**, 243 (1970).
- [95] G. Avitabile, R. Napolitano, B. Prozzi, K.D. Rouse, M.W. Thomas, B.T.M. Willis, *J. Polym. Sci. Polym. Lett. Ed.*, **13**, 351 (1975).
- [96] A. Panchenko, H. Dilger, J. Kerres, M. Hein, A. Ullrich, T. Kaz, E. Roduner, *Phys. Chem. Chem. Phys.*, **6**, 2891 (2004).
- [97] H.M. McConnell, *J. Chem. Phys.*, **24**, 764 (1956).
- [98] R.W. Fessenden, R.H. Schuler, *J. Chem. Phys.*, **43**, 2704 (1965).

- [99] S. Mitov, A. Panchenko, E. Roduner, *Chem. Phys. Lett.*, **402**, 485 (2005).
- [100] J.A. Weil, J.R. Bolton, J.E. Wertz, *Electron Paramagnetic Resonance: Elementary Theory and Practical Applications*, John Wiley & Sons, Inc., New York (1994).
- [101] P. W. Atkins, *Physical Chemistry 6th edition*, Oxford University Press (1998).
- [102] H. Fischer, in *Free Radicals*, editor J. K. Kochi, Wiley, New York, p. 442-454 (1973).
- [103] E.G. Janzen, *Acc. Chem. Res.*, **4**, 31 (1971).
- [104] A.E. Dikalova, M.B. Kadiiska, R.P. Mason, *PNAS*, **98**, 13549 (2001).
- [105] H.H. Perkampus, *UV-VIS Spectroscopy and its Applications*, Springer-Verlag Berlin, Heidelberg (1992).
- [106] H.H. Perkampus, *Analytiker-Taschenbuch*, Bd 3. Springer Berlin Heidelberg New York, S 279-316 (1983).
- [107] P. Atkins and J. De Paula, *Atkin's Physical Chemistry 8th edition*, Oxford University Press (2006).
- [108] G. Kortüm, *Kolorimetrie, Photometrie und Spektrometrie*, Kap. 1.5, 4. Aufl. Springer Berlin Göttingen Heidelberg, S 21 ff (1962).
- [109] P. Hohenberg, W. Kohn, *Phys. Rev.*, **136**, B864 (1964).
- [110] W. Koch, M.C. Holthausen, *A Chemist's Guide to Density Functional Theory*, Wiley-VCH, Weinheim, New York, Chichester, Brisbane, Singapore, Toronto (1999).
- [111] W. Kohn, L.J. Sham, *Phys. Rev.*, **140**, A1133 (1965).
- [112] J.B. Foresman, E. Frisch, *Exploring Chemistry with Electronic Structure Methods 2nd edition*, Gaussian, Inc. Pittsburgh, PA (1993).
- [113] A.D. Becke, *Phys. Rev. A*, **38**, 3098 (1988).
- [114] A.D. Becke, *J. Chem. Phys.*, **98**, 1372 (1993).
- [115] C. Lee, W. Yang, R.G. Parr, *Phys. Rev. B*, **37**, 785 (1988).
- [116] S.H. Vosko, L. Wilk, M. Nusair, *Can. J. Phys.*, **58**, 1200 (1980).
- [117] J.P. Perdew, Y. Wang, *Phys. Rev. B*, **45**, 13244 (1992).
- [118] L.A. Curtiss, K. Raghavachari, G.W. Trucks, J.A. Pople, *J. Chem. Phys.*, **94**, 7221 (1991).
- [119] E. Frisch, M.J. Frisch, *Gaussian 98 User's Reference*, Gaussian, Inc. Pittsburgh (1998).
- [120] E. Frisch, M.J. Frisch, G.W. Trucks, *Gaussian 03 User's Reference*, Gaussian, Inc. Carnegie (2003).
- [121] Landolt-Boernstein, *New Ser. II* (1977).
- [122] Y. Tabata, J. Fujikawa, *J. Macromol. Sci. A5: Chem.*, **5**, 821 (1971).

- [123] V. Barone, *Recent Advances in Density Functional Methods*, Part I, Ed. D. P. Chong, World Scientific Publ.Co., Singapore (1996).
- [124] M. Kaupp, M. Bühl, V.G. Malkin, *Calculation of NMR and EPR Parameters: Theory and Applications*, Wiley-VCH Verlag GmbH & Co. KGaA, Weinheim (2004).
- [125] M. Ye, H. Schuler, *J. Phys. Chem.*, **93**, 1898 (1989).
- [126] H.I. Joschek, S.I. Miller, *J. Am. Chem. Soc.*, **88**, 3273 (1973).
- [127] F.R. Hewgill, M.C. Pass, *Aust. J. Chem.*, **38**, 537 (1985).
- [128] C.M.R. Clancy, M.D.E. Forbes, *J. Phys. Chem. A*, **105**, 9869 (2001).
- [129] R. Ruggiero, A.E.H. Machado, A. Castellan, S. Grelier, *J. Photochem. Photobiol. A: Chem.*, **110**, 91 (1997).
- [130] C. Went, *Ionic Organic Mechanisms*, in *Dimensions of Science*, J.J. Thompson, editor, Macmillan Education Ltd, London (1986).
- [131] I. Saito, S. Kato, T. Matsuura, *Tetrahedron Lett.*, **11**, 239 (1970).
- [132] D.R. Kearns, *Chem. Rev.*, **71**, 395 (1971).
- [133] D.W. Clegg, A.A. Collyer, Eds., *Irradiation Effects on Polymers*, Elsevier: Essex (1991).
- [134] H.P. Brack, D. Ruegg, H. Buehrer, M. Slaski, S. Alkan, G.G. Scherer, *J. Polym. Sci.: Part B: Polym. Phys.*, **42**, 2612 (2004).
- [135] S. Mitov, G. Hübner, H.P. Brack, G.G. Scherer, E. Roduner, *J. Polym. Sci. Part B: Polym. Phys.*, **44**, 3323 (2006).
- [136] A.J. Swallow, *Polymers in: Radiation Chemistry of Organic Compounds*, Pergamon Press, Oxford (1960).
- [137] J.H. O'Donnell, *Chemistry of the Radiation Degradation of Polymers*, R.L. Clough, S. Shalaby, in *Radiation Effects on Polymers*, Amer. Chem. Soc., Washington, D.C., ACS Symp. Ser. No. 475, 402 (1991).
- [138] M. Iwasaki, K. Toriyama, T. Sawaki, M. Inoue, *J. Chem. Phys.*, **47**, 554 (1967).
- [139] M. Iwasaki, K. Toriyama, *J. Chem. Phys.*, **47**, 559 (1967).
- [140] S. Schlick, W. Chamulitrat, L. Kevan, *J. Phys. Chem.*, **89**, 4278 (1985).
- [141] S.S. Kim, R.H. Liang, "Effects of Ultraviolet and Vacuum Ultraviolet Irradiation on Fluorinated Ethylene-propylene Copolymers", in *Radiation Effects on Polymers*, ACS Symposium Series Vol. 475, R.L. Clough and S.W. Shalaby, Eds, ACS, Washington DC, Chap. 9 (1991).
- [142] F.A. Rasoul, D.J.T. Hill, G.A. George, J.H. O'Donnell, *Polymers Adv. Tech.*, **9**, 24 (1998).

- [143] D.J.T. Hill, S. Mohajerani, P.J. Pomeroy, A.K. Whittaker, *Rad. Phys. Chem.*, **59**, 295 (2000).
- [144] P. Hedvig, *J. Polym. Sci. A*, **7**, 1145 (1969).
- [145] M. Iwasaki, Y. Sakai, *J. Polym. Sci.: Polym. Phys. Ed.*, **6**, 265 (1968).
- [146] D. Olivier, C. Marachi, M. Che, *J. Chem. Phys.*, **71**, 4688 (1979).
- [147] M. Kuzuya, J. Niwa, T. Noguchi, *Polym. J.*, **27**, 251 (1995).
- [148] J.N. Helbert, B.E. Wagner, E.H. Poindexter, L. Kevan, *J. Polym. Sci.: Polym. Phys. Ed.*, **13**, 825 (1975).
- [149] Z.F. Illicheva, N.A. Slovokhotova, I.G. Akhvlediani, *Vysokomol. Soyed.*, **A18**, 209 (1976).
- [150] H. Suryanarayana, L. Kevan, *J. Amer. Chem. Soc.*, **104**, 6251 (1982).
- [151] A. Furuhashi, H. Mukozaka, H. Matsuo, *J. Appl. Polym. Sci.*, **12**, 2201 (1968).
- [152] Y. Haruvy, L.A. Rajbenbach, J. Jagur-Grodzinski, *J. Appl. Polym. Sci.*, **27**, 2711 (1982).
- [153] A. Oshima, T. Seguchi, Y. Tabata, *Polymer International*, **48**, 996 (1999).
- [154] A. Oshima, T. Seguchi, Y. Tabata, *J. Radiat. Phys. Chem.*, **55**, 61 (1999).
- [155] T. Matsugashita, K. Shinohara, *J. Chem. Phys.*, **35**, 1652 (1961).
- [156] *CRC Handbook of Chemistry and Physics*, 64th edition (1983-1984).
- [157] K.W. Egger, A.T. Cocks, *Helv. Chim. Acta*, **56**, 1516 (1973).
- [158] M.S. Miao, M.I. Zhang, V.E. Van Doren, *J. Phys. Chem.*, **A 104**, 6809 (2000).
- [159] S. Kavesh, J.M. Schultz, *Polym. Sci. Part A-2*, **8**, 243 (1970).
- [160] M.S. Miao, M.L. Zhang, V.A. Van Doren, *J. Chem. Phys.*, **115**, 11317 (2001).
- [161] T. Solomun, A. Schimanski, H. Sturm, E. Illenberger, *Chem. Phys. Lett.*, **387**, 312 (2004).
- [162] S.W. Benson, *Thermochemical Kinetics*, 2nd edition, p.74 (1976).
- [163] Landolt-Boernstein, *New Ser. II: 9a* 41, 46 (1977); **9b** 7, 56 (1977).
- [164] R.W. Fessenden, *J. Phys. Chem.*, **71**, 74 (1967).
- [165] Y. Ellinger, R. Subra, B. Levy, P. Milli, G. Berthier, *J. Chem. Phys.*, **62**, 10 (1975) and references therein.
- [166] J. Pacansky, M. Dupuis, *J. Chem. Phys.*, **68**, 4276 (1978).
- [167] T. Cole, H.O. Pitchard, N.R. Davidson, H.M. McConnell, *Mol. Phys.*, **1**, 406 (1958).
- [168] R.W. Fessenden, *J. Mag. Res.*, **1**, 277 (1969).
- [169] O.H. Griffith, *J. Chem. Phys.*, **41**, 1093 (1964).
- [170] R.W. Fessenden, R.H. Schuler, *J. Chem. Phys.*, **39**, 2147 (1963).

- [171] P.J. Krusic, P. Meakin, J.P. Jesson, *J. Phys. Chem.*, **75**, 3438 (1971).
- [172] L.D. Kispert, M.T. Rogers, *J. Chem. Phys.*, **54**, 3326 (1971).
- [173] S. Hara, K. Yamamoto, S. Shimada, H. Nishi, *Macromolecules*, **36**, 5661 (2003).
- [174] A. Faucitano, A. Buttafava, F. Martinotti, *Tetrahedron Letters*, **31**, 7055 (1990).
- [175] M. Kadirov, A. Bosnjakovic, S. Schlick, *J. Phys. Chem. B*, **109**, 7664 (2005).
- [176] M.T. Rogers, L.D. Kispert, *J. Chem. Phys.*, **46**, 3193 (1967).
- [177] Landolt-Boernstein, *New Ser. II*: **9b** 10, 12, 244, 245 (1977).